Object Localization in Fluids based on a Bioinspired Electroreceptor System

DISSERTATION

submitted in partial fulfillment
of the requirements for the degree of
Doctor rerum naturalium
(Dr. rer. nat.)

Sabine Wolf-Homeyer

Faculty of Technology
Bielefeld University
Germany

June 2019

Object Localization in Fluids based on a Bioinspired Electroreceptor System

DISSERTATION

submitted in partial fulfillment
of the requirements for the degree of
Doctor rerum naturalium
(Dr. rer. nat.)

Sabine Wolf-Homeyer

Faculty of Technology
Bielefeld University
Universitätsstr. 25
33615 Bielefeld
Germany

June 2019

Reviewers:

Prof. Dr. Elisabetta Chicca
Prof. Dr. Jacob Engelmann
Prof. Dr. Axel Schneider (supervisor)

Acknowledgments

"The test of all happiness is gratitude"
Gilbert Keith Chesterton (1874-1936)

This thesis would not have been possible without the support of several people and institutions. I would like to take this opportunity to express my sincere thanks for the help received in so many ways:

My first words of gratitude go to my supervisor Prof. Dr. Axel Schneider, who gave me the opportunity to deal with this interesting and interdisciplinary subject including electromagnetism, simulations, mathematics and biology. Our continuous meetings and constructive discussions have enabled me to gain many skills and experiences that will carry me forward in my future life.

Prof. Dr. Jacob Engelmann supported me significantly with inspirations on the biological aspects of this work. In addition to his expertise in finding answers to biological questions, I want to thank him for his continuous encouragement during the dissertation process.

Special thanks also go to Prof. Dr. Elisabetta Chicca, who has accepted to review this thesis from the perspective of an independent external expert.

In recent years, several students and employees have made a major contribution to the development of a measurement system, used to validate the introduced strategies. In particular, I would like to mention Fabian Eickmann and Jens Böckmann to thank them for their commitment and support.

My special gratitude also goes to Prof. Dr. Jutta Kunz-Drolshagen, who helped me a lot with her expertise in theoretical physics during the final examination of my work.

Also, I thank Dr. Irén Juhasz Junger and Dr. Thomas Maier for the intensive professional exchange concerning the theoretical aspects of this work.

My thanks also extend to the employees on floor A5 at Bielefeld University of Applied Sciences, in particular Kerstin Kuper, Diana Schneider, Constanze Schwan, Simon Bekemeier and the members of the HEA^{2}R-team for the friendly and supportive atmosphere.

In addition, I would like to thank Prof. Dr. Michaela Hoke and Prof. Dr. Christian Schröder for the follow-up financing of this work and Christine Scheele for her administrative support. Many thanks also to Maren Köster for the friendly meetings in which honest and constructive discussions could took place.

Moreover, I would like to express sincere thanks to my peer group consisting of Dr. Nina Brassler, Dr. Julia Hinz, Dagmar Jantos, Sabine Kraus and Marieke Pahlke. Your impulses, suggestions and encouraging words have been my motivation to continue this work even in times of crisis. Furthermore, my mentor, Dr. Dr. Andrea Ehrmann, has supported me in decision-making processes with a lot of tailwind for which I thank her deeply.

My sincere thanks also go to Dr. Lisa Teich for her comprehensive and always fast support and the pleasant positive words. Our exchange of information and experience was very precious to me and I thank her very much for her time.

I thank Gottfried Meier, for repeatedly redirected my focus and confidence back to trusting in my core beliefs. It helped me power through the difficult times.

My deepest thanks goes to my family and friends for their understanding, their extensive support and their love. Specifically, I would like to thank my daughter Lucy who is stuffed with a lot of happiness. She made me realize that you can use glitter whenever life seems difficult. My son Felix, equipped with a excellent sense of humor, has often shown me that many things are easier to handle with irony and music. Special thanks go to my safe haven, reliable companion, best friend and beloved husband Peter. His focus on actions and not on words always provided me with stability. This work would never have been possible without him. I am deeply grateful that you three exist.

"Beryllus lapis est lucidus, albus et transparens. Cui datur forma concava pariter et convexa, et per ipsum videns attingit prius invisibile. Intellectualibus oculis si intellectualis beryllus, qui formam habeat maximam pariter et minimam, adaptatur, per eius medium attingitur indivisibile omnium principium."

Nicolaus Cusanus (1401-1464), "De Beryllo" (Capitulum II)

Object Localization in Fluids based on a Bioinspired Electroreceptor System

by

Sabine Wolf-Homeyer

Faculty of Technology
Bielefeld University
Germany

Abstract

Weakly electric fish use self-generated electric fields for communication, active electrolocation and navigation. Additionally to visual sense, this ability enables them to detect objects and food even in dark or turbid waters. Specialized muscle cells in the tail region actively generate an electric field in the surrounding fluid, shaped like a dipole between tail and head. This dipole field may be distorted depending on environmental parameters such as the presence of objects of different geometry or material properties in the animal's vicinity. Electroreceptors, distributed all over the fish' skin allow to perceive distortions of the field, caused by objects. Furthermore, fish execute stereotyped scanning behaviors to obtain additional sensory information of detected objects.

The development of innovative sensor systems for short-range exploration in fluids is still in its infancy. Also, the use of electric fields in bio-inspired technologies is still at an early stage. Based on the biological model of weakly electric fish, the question has already been examined if an array of electrodes can be used for a contactless object detection and localization and finally for navigation in fluids (Solberg et al. 2008). This examination is performed by analyses of electric field modulations, based on so-called EEVs. An EEV (Ensemble of Electrosensory Viewpoints) is a scalar field representation of the influence of an object on the electric field in the form of potential differences measured between two electrodes for every possible object location.

The first part of this thesis explores the characteristics of the electric dipole field and the resulting EEV by means of numerical simulations to determine the influence of an object placed in the emitted field. It will also be investigated how many receptors are required and which arrangement is to be preferred to uniquely identify the positions of spherical objects in the vicinity of the sensor system. For this, a receptor system composed of a simple biomimetic abstraction of an emitter dipole and an orthogonally arranged pair of sensor electrodes is used. Inspired by the scanning movements of the fish, a fixed, minimal scanning strategy, composed of active receptor system movements is developed. The active electrolocation strategy introduced here is based on the superposition of

extracted EEV contour-rings in order to find intersections of these contours.

The second part of this work focuses on the development of an *application* for active electrolocation which is based on a minimal set of scanning movements as a precursor for the partitioning of the later search area in which sensor-emitter movements take place. In this application, EEVs are also used as major components of two localization algorithms. In order to find points within the search space which are part of several contour-rings, intersection points have to found. Due to numerical inaccuracies intersection points may degrade to contour-segments which lie very close to each other but do not touch. For this case, a nearness metric is used to identify such points. However, in this part of the work the EEVs are based on a simplified analytical representation, which renders the corresponding algorithms suitable for embedded computer systems.

In the third part of this thesis, a fitted histogram representation of EEVs is used to compare a large number of different movement sequences to select the optimal composition from this variety. For this, the general shape of an EEV has to be considered, which plays a major role in estimating the best sequence.

Contents

List of Figures

List of Tables

Publications

- S. Wolf-Homeyer, J. Engelmann, A. Schneider: Application of reduced sensor movement sequences as a precursor for search area partitioning and a selection of discrete EEV contour-ring fragments for active electrolocation, *Bioinspiration & Biomimetics*, 13(6): 066008, **2018**

- S. Wolf-Homeyer, J. Engelmann, A. Schneider: Electrolocation of objects in fluids by means of active sensor movements based on discrete EEVs, *Bioinspiration & Biomimetics*, 11(5): 055002, **2016**

- S. Wolf-Homeyer, J. Engelmann, A. Schneider: Reduced sensor movement sequences for a partitioning of search area and a selection of discrete EEV contour-ring fragments in active electrolocation, *110th Annual Meeting of the German Zoological Society (DZG)*, **September 12-15, 2017**, poster presentation, Bielefeld, Germany

- S. Wolf-Homeyer, J. Engelmann, A. Schneider: Bionic Electrolocation Strategy of Objects in Fluids based on Superposition of Numerically Extracted and Shifted EEVs, *DPG Conference*, **March 19-24, 2017**, poster presentation, Dresden, Germany

- A. Schneider, S. Wolf-Homeyer: Objektlokalisation in Fluiden auf Basis eines bioinspirierten Elektrorezeptorsystems, *8. Bremer Bionik-Kongress*, **October 21-22, 2016**, invited talk, Hochschule Bremen, Germany

- S. Wolf-Homeyer, J. Engelmann, A. Schneider: Bio-inspired method for electrolocation of objects in fluids based on active sensor movements, *DPG-German Conference of Women in Physics 2016*, **November 3-6, 2016**, poster presentation, Hamburg, Germany

1

Introduction to biological and bioinspired electrolocation

Abstract

This chapter provides a short introduction, first to the biological and then to the bioinspired electroreceptor system to be developed. At the beginning, various sensory modalities of biological beings are presented. Subsequently, the ability of weakly electric fish to perform active electrolocation will be described. This is followed by the concept of electric images which enables the fish to perceive objects and their parameters. After that, the scanning behavior of the weakly electric fish while approaching and identifying objects is presented. Inspired by the biological model, an abstraction of the electrosensory system of the fish for the development of a technical receptor system will be introduced. To investigate different strategies for active electrolocation, the concept of EEVs will be revised and modified. Closing the chapter, the main research objectives of the thesis are defined and the content of the main chapters is outlined.

1.1 Sensory modalities and electrosensory system of the weakly electric fish

Evolution has led to various sensory modalities of biological beings adapting them to different habitats to be able to perceive relevant information from their environment. Depending on the life-style and the physical propagation properties of the specific medium that sensory systems are tuned to the modalities can be classified as far, intermediate, near and contact senses. Examples for far range sensing are the visual sense or the echolocation system of bats and toothed whales (Jones 2005). An example for near range sensing are the specialized hair cells of insects (Zill et al. 2014) or the mechanical

appendages for tactile exploration like antennae (Staudacher et al. 2005). Fish have evolved various intermediate range sensory systems. A typical mechanosensory example is the lateral line system that is tuned to low frequency vibrations and preassure differences caused by water movements (Mogdans and Bleckmann 2012). Another example, often found in aquatic vertebrates, is the ability to perceive low frequency electric fields. This so-called passive electroreception is frequently found in fishes and has evolved independently several times.

Contrary to the passive sense, only a few lineages of fish have evolved the ability to actively generate weakly electric fields and use these self-generated fields to explore their environment. This so-called active electric sense has been discovered in the 1950s when Lissmann demonstrated that some fish can use these fields to identify objects in their nearby environment (Lissmann 1958; Lissmann and Machin 1958).

Afterwards it has been determined that these fish also use electric fields to communicate (Moller 1970; Hopkins 1999). The ability to sense and detect objects within a short range of approximately twice the body length of the animal (Sichert et al. 2009) is called active electrolocation (von der Emde 1999). A prominent and well studied example of a weakly electric fish is Peters' elephant-nose fish (*Gnathonemus petersii*) as shown in figure 1.1. These nocturnal fish, native to the rivers of West and Central Africa, use active electrolocation to orient in darkness or turbid waters. They are also able to identify the size, shape, material properties and relative position of unknown objects (von der Emde and Fetz 2007).

FIGURE 1.1: Picture of a weakly electric fish, in this case, Peters' elephant-nose fish (*Gnathonemus petersii*). Its characteristic *Schnauzenorgan*, which is a flexible extension of its chin, explains the origin of this species name. The fish have the special ability to actively generate electric fields and perceive them on their skin to detect and analyze objects in their environment. The photograph was generously provided by Jacob Engelmann.

The electric organ of the fish represents the emitter part of the biological electrosensory system. It consists of specialized muscle cells located in the tail region of the fish, which are responsible for the field generation (Lissmann 1951; M. V. L. Bennett 1971). By

discharging the electric organ, a bipolar weak electric field is build up which surrounds their body. Figure 1.2(a) shows a 2D-illustration of the isopotential lines which indicates the emitted field. In this example, the field is distorted by the presence of objects consisting of different materials. The distortion depends on the relation of the material parameters (i.e. conductivity and permittivity) of the respective object to the fluid. The analytical calculation of the field distortion plays an important role in this work, therefore it will be described in more detail in chapter 2. An effect that sets the dipole field of the animal apart from a simple dipole field is the fact that the animals body and the anatomy of the electric organ as well as its innervation shape the geometry of the dipole-like field, resulting in asymmetric properties (Machin and Lissmann 1960; Bell et al. 1976). While this is of biological as well as technical importance, the field-shaping effects of the body are not covered in this thesis to be able to focus on very basic abstractions of biological principles first.

In general, two main orders of weakly electric fish which differ in characteristics of form and continuity of their electric organ discharge (EOD) signal, have evolved in parallel (Bullock and Heiligenberg 1986). Most of the *Gymnotiformes*, native to South America, emit a nearly sinusoidal waveform of the EOD signal. In contrast, most of the *Mormyriformes* like *Gnathonemus petersii*, exhibit short and pulsed EOD signals. A typical biphasic pulse-type EOD waveform of *Gnathonemus petersii*, is exemplarily shown in figure 1.2(b). Environmental modulations of the EOD amplitude, frequency and/or phase allows the fish to perform active electrolocation but also to differentiate between individuals (Crawford 1992; Mc Gregor and Westby 1992), species (Hopkins and Bass 1981), genders (Bass and Hopkins 1983) and dominance (Carlson et al. 2000).

The sensor part of the biological electrosensory system is constituted by electroreceptors which are distributed across the fish's skin (Szabo 1965; Caputi and Budelli 2006). Two types of receptive organs are identified: Ampullary electroreceptors, sensitive to low-frequency electric fields, are used for passive electrolocation (Bullock and Heiligenberg 1986), whereas tuberous electroreceptors, which are only present in fish that perform active electrolocation, are able to perceive higher frequencies (von der Emde and Bleckmann 1997). Tuberous organs are subdivided again into so-called *Knollenorgan* receptor organs, which perceives EODs of other fishes during electrocommunication (Hopkins 1983; Zakon 1987; Kramer 1990) and into *Mormyromast* electroreceptors which are used for sensing the self-emitted EOD pulses (Bell 1990; von der Emde 1999). The biological measurement system is mainly composed of more than 2000 Mormyromasts distributed over the surface of the skin, but the density distribution of the receptor organs is not uniform (Hollmann et al. 2008). Most electroreceptors can be found in the head region and in particular on the extended chin, the so-called *Schnauzenorgan*. It indicates regions with high receptor densities within the electrosensory surface (*functional foveae*) (Caputi et al.

(a)   (b)
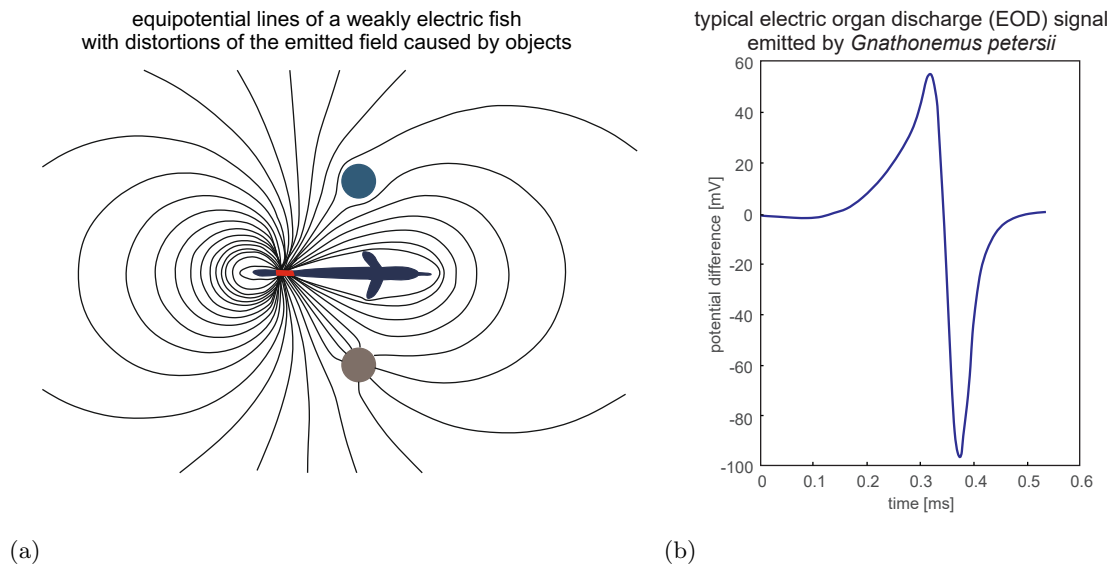
FIGURE 1.2: Equipotential lines surrounding the body of the weakly electric fish and a typical EOD signal. (a) Top view of equipotential lines which surround the weakly electric fish. The emitted field is distorted by objects of different materials. The emitter (electric organ), which is located in the tail region of the fish, is marked in red. The object shown above is more conductive (e.g. metal) and the object illustrated below is less conductive than the fluid surrounding the fish. (b) Typical electric organ discharge (EOD) signal, here emitted by *Gnathonemus petersii*, does not vary appreciably but minor modifications of EOD amplitude and duration are used by fish for communication and orientation. This depends, for example, on the sex and hormonal state of the fish (Bass and Hopkins 1985). The EOD is measured by using two electrodes in the water, which are positioned in front of and behind the fish.

2002; Bacelo et al. 2008). The biological electrosensory system allows perceiving field distortions caused by objects by detecting potential changes in the range of 0,1 % of the basal field amplitude on the surface of the fish's skin (Nelson and MacIver 1999). For an estimated skin potential of about 1 mV, the perception limit is in the µV-range. This extreme sensitivity underlines the attractiveness of this sensory modality for technical abstractions, although reaching the same sensitivity will be challenging, understanding how animals deal with measurement noise will certainly be informative for technical abstractions of this ability.

The presence of an object in the environment of the fish results in a 2D-modulation of the self-generated electric field at the electroreceptive skin of the animal, which has been termed as the *electric image* (Budelli and Caputi 2000; Budelli et al. 2002; Engelmann and von der Emde 2011). Based on the concept of electric images, a correlation of object parameters and signal parameters exists (figure 1.3). This enables the fish to perceive objects and their properties like position, distance, size, shape and material parameters in a complex 3D-scene (Toerring and Moller 1984; Engelmann et al. 2008; Engelmann and von der Emde 2011).
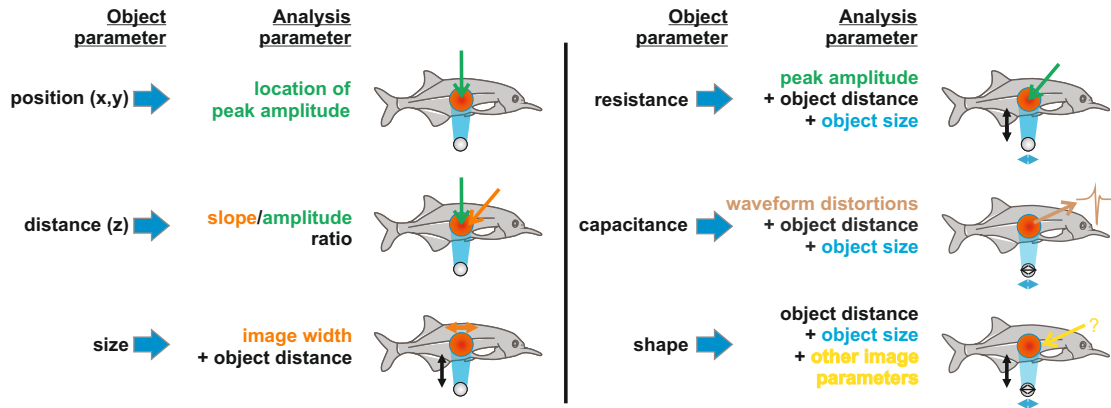
FIGURE 1.3: Detection of different object parameters based on combinations of image/analysis parameters. Based on the concept of electric images, weakly electric fish are able to detect objects and to analyze their properties in a complex 3D-scene. This includes the position of the object along the fish body, the distance of the object to the fish, the size, material parameters of the object and the shape. The fish can identify these object parameters by combining different parameters such as the location of the amplitude, the slope, the width and size of the image, the distance to the object, the waveform distortions and more. The figure is adapted from (Engelmann and von der Emde 2011).

However, it has to be noted that there is no one-to-one relationship between the spatial properties of the object and the shape of the electrical image when projecting 3D-objects onto the 2D-sensory surface, since electrical images are usually blurred (Engelmann and von der Emde 2011). But different combinations of analysis parameters enable the fish to identify the individual object parameters. Even if fish, based on the concept of electrical images, are able to detect several object parameters according to a combination of analysis parameters, only the aspect of object localization is initially considered in this work. The reason for this is to take a step backwards in order to extract as much information as possible from the basic data and a few parameters by using basic procedures.

The information and data processing of the biological electrosensory system is performed by the central nervous system of the fish. Mormyromast electroreceptors transduce the electrosensory signals necessary for active electrolocation. A Mormyromast contains two different types of electroreceptor cells: The A-cells encode only the amplitude of the signal, while the B-cells are sensitive to both the amplitude and the waveform (phase shifts) (Bell et al. 1989). The sensory input of both types of receptor cells is transmitted to two zones of the electrosensory lateral line lobe (ELL) of the brain (Bacelo et al. 2008). Within a layer of granule cells, the temporal code of the signal is transformed into a rate code. A second input, an electric organ corollary discharge (EOCD), is also processed in the granule cells in order to predict and eliminate responses to self-generated stimuli (M. V. L. Bennett and Steinbach 1969). The EOCD is a copy of centrally generated motor command signals which is sent from motor areas responsible for EOD generation

to sensory systems involved in the processing and analysis of electrosensory data (Bell 1982; Bell et al. 1992; Bell and Grant 1992; Sawtell 2010).

1.2   Scanning behavior of weakly electric fish

Weakly electric fish use a sophisticated repertoire of movement behaviors while approaching objects (Toerring and Belbenoit 1979). This exploratory behavior has been characterized in five different probing motor acts (PMAs) as illustrated in figure 1.4. The fish changes their position and body geometry to obtain additional sensory parameters like the size, shape, and material properties of the detected objects (von der Emde and Fetz 2007; Engelmann and von der Emde 2011; Stamper et al. 2012; Pedraja et al. 2018). This scanning behavior is based on whole body movements (Engelmann et al. 2009) and on motor prototypes with rotational and translational character arranged sequentially in time (Toerring and Moller 1984; Hofmann et al. 2014; Lebastard et al. 2016).
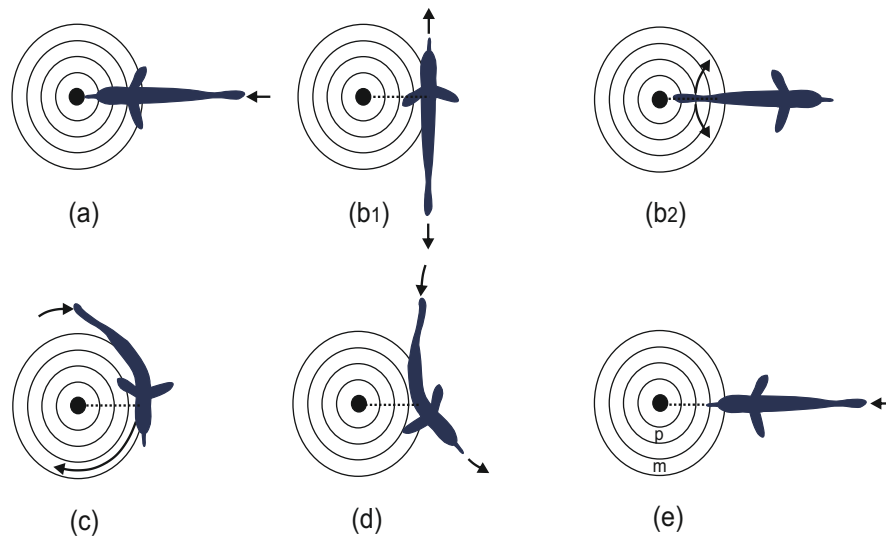
FIGURE 1.4: Exploratory behavior of weakly electric fish. The fish uses five different probing motor acts (PMAs) while investigating objects of interest. The circular object is surrounded by concentric circles which enable the comparison of probing distances for example when using different materials of the object (metal rod (m), porcelain tube (p)). The dashed lines indicate the corresponding probing distance. The arrows are pointing in direction of the fish's movements. The PMAs have been termed differently: (a) chin probing, (b$_1$) lateral va-et-vient, (b$_2$) radial va-et-vient, (c) lateral probing, (d) tangential probing, (e) stationary probing. The figure is redrawn according to (Toerring and Belbenoit 1979; Toerring and Moller 1984)

Inspired by the biological model, the question arises whether the exploratory behavior of fish, based on their different movement actions, can be used to develop a minimal and fixed scanning strategy that allows a unique localization of objects. In order to analyze and compare different movement sequences, in this work the options for moving

the sensor-emitter array are reduced to the two fundamental modalities of rotation and linear shift.

1.3 Abstraction of the biological electrosensory system for the development of a technical electroreceptor system

As explained in chapter 1.1, the electrosensory system of weakly electric fish, used for active electrolocalization, is basically composed of the electric organ, the electroreceptors and the central nervous system as illustrated in figure 1.5(a). In order to transfer the localization capabilities of the fish to the technological domain, an abstraction inspired by the biological system is carried out. Figure 1.5(b) shows the electrosensory system of a hardware setup used to develop and perform active electrolocation strategies. Similar to weakly electric fish, the technical system is also composed of three main components: The emitter system is required to generate an electric field, the sensor system is responsible for receiving the signal and a system for acquiring and processing the data has to be implemented.

The aspect that the weakly electric fish forms an electric dipole-like field around its body will be considered during designing a sensor system for active electrolocation. Based on the biological model, the emitter system here comprises two emitter electrodes connected to a function generator to create an electric dipole field. The pulse waveform of the fish's EOD signal is simplified by a continuous sinusoidal signal which is emitted by the function generator. On the one hand a sinusoidal signal is used to avoid electrolytic effects (Eickmann 2014), on the other hand the use of any other periodic but non-sinusoidal waveform would show disadvantages. A square wave signal for example is approximated by an additive synthesis of a large number of sine waves. However, a variety of signal processing techniques include the *Fourier analysis*, in which a function of the real signal over time is transformed into a function of frequency. Concerning the square wave signal, it leads to a large frequency spectrum, whereas the sinusoidal signal only consists of the fundamental frequency, a fact that simplifies the signal analysis.

In the following analyses, simulations and calculations, a static 2D-dipole field, generated at the emitter electrodes, is assumed. A further simplification with respect to the biological example concerns the analysis of the data, where here only the effective signal amplitude (RMS value) is considered. Thus, in contrast to the fish, the phase distortions of the emitted signal is not analyzed . As shown by Meyer (1982) and von der Emde (1999), Mormyrid fish can indeed use this information to determine capacitive properties of objects.

electrosensory system of weakly electric fish

electrosensory system of hardware setup

central nervous system
electroreceptors
electric organ

data processing PC
data acquisition ADC
amplifiers

data acquisition and processing system
sensor system
emitter system

function generator

(a)

(b)
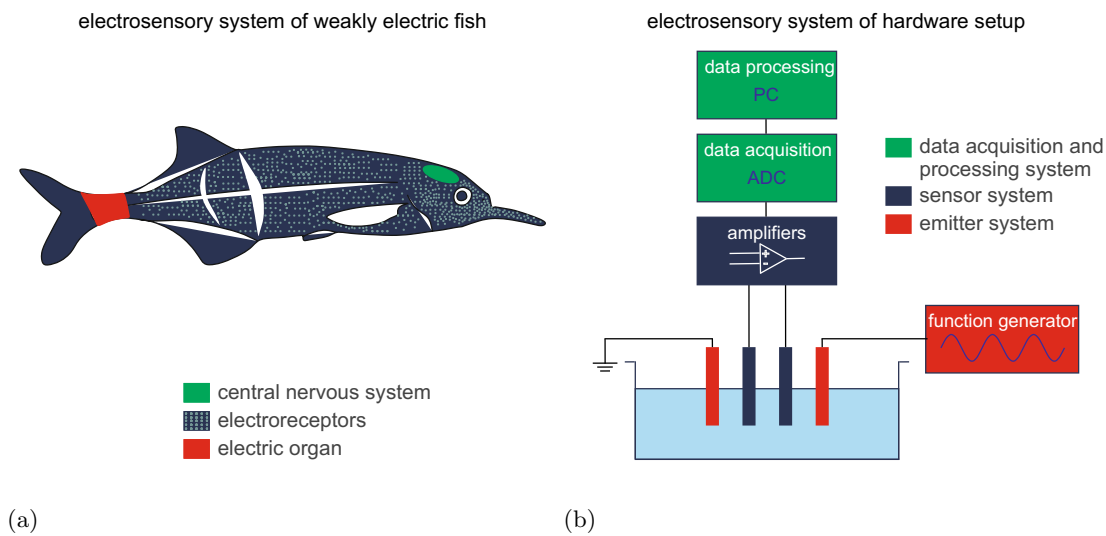
FIGURE 1.5: Comparison of the biological and technical electrosensory system used for active electrolocation. (a) Electrosensory system of a weakly electric fish. In principle, the biological system is composed of the electric organ, the electroreceptors and the central nervous system. The electric organ is responsible for generating a weak electric field surrounding the fish body. A large number of electroreceptors is distributed on the fish's skin to sense distortions of the field when objects are present. The acquisition and processing of the sensory data is performed by the central nervous system of the fish. (b) Electrosensory system as a hardware setup. Inspired by the biological model, the basic components of the hardware system exhibit similar functionality for active electrolocation. Two emitter electrodes and a function generator are used to realize an emitter system. The simplified sensor system consists of a sensor pair and corresponding signal amplifiers. The data acquisition is carried out by an analog-to-digital converter (ADC) and the processing of data is performed by a measurement computer. The emitter and sensor electrodes are located in a fluid-filled basin.

Furthermore, the electroreceptors in the electrosensory system of the fish, consisting of a large number of Mormyromasts, is abstracted to a minimum number of sensors for the design and development of the hardware system. This minimum condition requires at least two sensors to allow for differential signal acquisition (as opposed to a single-ended configuration) and to allow for a large amplification. Differential measurement of voltages compared to single-ended measurement provides the advantage that noise signals which act simultaneously on both sensors will not be considered during measurements. Thus a large amplification at both sensors is achievable even with noisy signals, since the noise is then almost eliminated.

In a first step, the emitter and sensor electrodes are arranged orthogonally to each other as in Solberg et al. (2008) and are placed in a fluid-filled basin. This minimal abstraction is to be characterized by how much information can be obtained using this basic sensor-emitter ensemble. In addition, further questions regarding the number and arrangement of sensors and emitters have to be answered. How much more information can be obtained if multiple sensor pairs are used for electrolocation, just as the fish is

equipped with many sensors on its skin? With respect to the fovea of fish, it can also be investigated whether a high sensor density at particular locations can be useful to acquire more information and to achieve a unique localization of objects.

The third main component of the hardware-setup is the data acquisition and information processing stage. In accordance to the data processing system of the biological model, in which the input signal obtained by the electroreceptors is sampled, encoded, and further processed by peripheral and central neurons specialized for time coding (Kawasaki 2009), the technical system requires an analog-to-digital converter (ADC) to transform the amplified analog measurement signal into a digital signal. In the first step, the data processing is carried out by a PC. Once suitable localization strategies have been developed and successfully validated, the implementation on an embedded hardware system for the analysis and digital processing of measured signals is intended.

Weakly electric fish are considered to be capable of forming a cognitive map and exhibit a memory of the position of landmarks for a successful navigation (A. T. D. Bennett 1996; Braithwaite 1998; Cain and Malwal 2002). In accordance to this ability, in this work the concept of EEVs introduced in Solberg et al. (2008), will be revised, which comprises the location of objects at different positions relative to the sensor array. In principle, also here a map, the so-called EEV matrix, is used for object localization. The matrix can be constructed by systematically placing an object at each discrete position on a grid. It contains the observed potential difference measured at the sensors for each coordinate of the object. A previously generated EEV can be used as a look-up table which is only dependent on direct sensor readings in order to carry out and investigate different active electrolocation strategies for a unique identification of objects.

Previous work already examined various approaches and methods for identifying objects in active electrolocation systems, bioinspired by weakly electric fish. As mentioned before, these fish are able to perceive perturbations of the self-generated electric field by means of electroreceptors on their skin. In a similar fashion, sensors integrated in a hardware setup can be used to detect distortions of a self-generated electric dipole field. A close inspection of the distortions provides further data including information on size, shape and material properties of detected objects. Electrosensory information can be obtained both from the amplitude or/and the phase shifts of the measured perturbation signal. For example, in Ammari et al. (2014) the frequency dependency is used for shape classification and recognition of objects with large permittivity, whereas Solberg et al. (2008) have focused on extracting information from the amplitude of the perturbations. Likewise Gottwald et al. (2017) used amplitude and waveform measurements to investigate strategies comparable of those used by the animals, to determine the distance and the impedance of capacitive objects.

In general, two different experimental setups have been used to develop methods for localizing and identifying objects and their properties based on electrosensory information. Boyer's group has specialized on a configuration with multiple current sensors (Boyer et al. 2012; Boyer et al. 2013; Lebastard et al. 2013; Boyer et al. 2015; Bazeille et al. 2018). The general principle is based on emitting a voltage and sensing the currents in a multiple-electrode electrosensory platform (Servagent et al. 2013). In contrast, the principle used in the list of references Solberg et al. (2008); Y. Silverman et al. (2012); Snyder et al. (2012); Neveln et al. (2013); Dimble et al. (2014); Bai et al. (2015) and Bai et al. (2016) is based on the combination of two emitter electrodes for generating an electric dipole field and a varying number of pairs of differential electrodes for sensing the potential differences. Based on their differing sensing modes, these two options are also referred to as *U-I* or *U-U* sensors.

These approaches have resulted in the introduction of probabilistic based procedures for navigation based on electric information as well as the localization of objects. In Lebastard et al. (2013), an environment reconstruction based on a Kalman filter is introduced, whereas Solberg et al. (2008) and Stachniss and Burgard (2014) use a particle filter approach, which is a type of Bayes filter. In a further example shown in Y. Silverman et al. (2012), a combination of a particle filter and an extended Kalman filter approach has been introduced to estimate the location and orientation of a robot system with respect to the object. Thus, this robot system is able to localize and orient itself. The common feature of all probabilistic sensor models is that the measured values are considered as probability distributions. Depending on a diversity of usage, a suitable choice based on these different statistical algorithms has to be defined.

The strategies developed in this thesis are all based on voltage measurements, are initially examined independently of the more complex and higher-level procedures like probabilistic approaches (e.g. particle filter algorithm, Kalman filter, Bayes filter). They are focused on the extraction of existing information from unprocessed data. However, in the future they may act as a pre-processing step for higher-level algorithms. The principal mathematical means to analytically describe the perturbation of an electric field caused by an object used in this thesis draw on earlier works (Lissmann and Machin 1958; Bacher 1983; Rasnow 1996; Ammari et al. 2013). These approximations will be used in chapters 4 and 5 to analytically describe an EEV and thus the influence of a spherical object on the electric field. Based on this mathematical framework, it is intended to develop methods that can be implemented in an embedded software system.

1.4 Outline of the thesis

The present work is structured into a theoretical description of the fundamentals and in three main research objectives:

Chapter 2 introduces the fundamentals of the theoretical description of an electric field and its distortion by objects. In particular, the properties of the field at interfaces between different materials will be investigated more closely. In this context, the interface between object and fluid represents an important focus which provides the basis for an analytical field description which plays a central role later in this work. This so-called *simplified analytical formulation* requires only a lower computational power compared to simulations when performing active electrolocation. In the second part of this chapter a numerical FEM-simulation of the distorted electric field is presented. At the end of the chapter the concept of electrical viewpoints is introduced which provides the foundation on which all subsequent chapters are based.

In chapter 3 the first main research objective is presented in which an optimal concatenation of active receptor system movements is to be examined. Inspired by the electrosensory system and the scanning behavior of weakly electric fish, an optimal scanning strategy composed of reduced sensor movements based on numerically extracted EEVs is to be developed. The aim is a unique localization of a spherical object.

The second main research objective, introduced in chapter 4, is concerned with the development of an application for active electrolocation. This is based on the reduced sensor movements explored in chapter 3 which will be used in a preliminary step for a search area partitioning and a fragmentation of extracted EEV contour-rings. In this chapter, the EEVs will be generated by means of a simplified analytical formulation. Based on a nearness metric, a strategy for active electrolocation is to be developed, which can be implemented on an application-oriented embedded hardware system. Furthermore, this strategy will be used to empirically determine an optimal composition of movements of the sensor-emitter ensemble.

The third main research objective presented in chapter 5 is based on the optimal composition of movements whose result was determined before in chapter 4. For the symmetrical sensor-emitter arrangement, a method is developed that can be used to compare a large number of different movement sequences to analytically determine the optimal composition of movements. For this purpose, a fitted histogram representation of analytically calculated EEVs is used to estimate the best sequence by means of the resulting fit curve.

The last chapter 6 contains a conclusion of the results and the final discussion of the achievements of this thesis. An outlook on further possible methods and applications completes this work. In this context, a particular focus is directed to the investigation of unsymmetrical sensor arrangements for possible improvements of the already introduced strategies.

2

The electric field and its perturbation by spherical objects

Abstract

This chapter gives a summary of the basic equations, which are required to describe the characteristics of electromagnetic fields and their perturbation by spherical objects. Both an analytical and a numerical solution for the description of the distortion will be presented. The explanations are based on the following literature, which is specialised in electrodynamics of media and of analytical and numerical solutions of electric and magnetic fields (Landau et al. 1984; Jackson 1999; Griffith 1999; Binns et al. 1993) Based on this theoretical background, the perturbation of the field and its representation with electrical viewpoints will be presented.

2.1 Analytical description of the perturbed electric field

For simple geometric objects like spheres or cylinders within an electric field, an analytical description for the field and the change of its shape can be found. The analytical description presented in this section is based on Maxwell's equations and the resulting interface-conditions at a surface between different media. In order to find a solution, suitable boundary conditions and simplifications have to be defined. First, the simple case is assumed where a spherical object is located in a uniform electric field. In the further procedure the field is extended to a dipole field. To find a mathematical description, especially for the perturbation by the spherical object, a solution for the Poisson's or Laplace's equation has to be derived. These equations, which will be explained in more detail below, represent suitable descriptions of many natural scientific problems.

2.1.1 Macroscopic Maxwell's equations

At the interface between two media with different electrical properties, the characteristics of the fields can be described by the macroscopic Maxwell's equations (Maxwell 1865; Maxwell 1873), here shown in differential form. In contrast to the integral representation, the differential form treats location-dependent quantities and the central values are the electromagnetic fields themselves.

$$\vec{\nabla} \cdot \vec{D} = \rho_q \qquad \text{(Gauss's law)} \tag{2.1}$$

$$\vec{\nabla} \cdot \vec{B} = 0 \qquad \text{(Gauss's law for magnetism)} \tag{2.2}$$

$$\vec{\nabla} \times \vec{E} + \frac{\partial \vec{B}}{\partial t} = 0 \qquad \text{(Faraday's law)} \tag{2.3}$$

$$\vec{\nabla} \times \vec{H} - \frac{\partial \vec{D}}{\partial t} = \vec{J} \qquad \text{(Ampère's law)} \tag{2.4}$$

$\vec{E}$ denotes the electric field, ρ_q the total charge density, $\vec{B}$ the magnetic flux density, $\vec{H}$ the magnetic field, $\vec{D}$ the electric displacement field (electric flux density) and $\vec{J}$ the current density. All field quantities locally depend on space $\vec{x}$ and time t. Gauss's law shown in equation (2.1) indicates that electrical charges are the sources of the electric displacement field. Equation (2.2) shows the Gauss's law for magnetism. It means that the magnetic field is source-free because there are no free magnetic charges or magnetic monopoles. Faraday's law (equation (2.3)) states that a time-varying magnetic flux density induces a local curl of the electric field. The last of the Maxwell's equations as shown in equation (2.4) is called Ampère's law. The equation expresses that a time-varying electrical flux density and a current density cause a local curl of the magnetic field.

In addition, also the influence of material properties must be taken into account by supplementary equations. These linear approximations are valid in homogeneous, linear and isotropic media:

$$\vec{D} = \epsilon \vec{E} \tag{2.5}$$

$$\vec{B} = \mu \vec{H} \tag{2.6}$$

$$\vec{J} = \sigma \vec{E} \qquad \text{(Ohm's law)} \tag{2.7}$$

In these equations, μ stands for the permeability of the material and σ for the conductivity of the conductive medium. The permittivity ϵ is the product of the vacuum permittivity ϵ_0 and the relative permittivity ϵ_r:

$$\epsilon = \epsilon_0 \cdot \epsilon_r \tag{2.8}$$

The four Maxwell's equations and three material equations described above combined with the equation of continuity of charge are sufficient to describe the relationships of electric and magnetic fields and currents (with defined boundary conditions) in materials.

$$\frac{\partial \rho}{\partial t} + \vec{\nabla}\vec{J} = 0 \qquad \text{(Continuity equation)} \tag{2.9}$$

The continuity equation represents the relationship between the charge and the electric current within a medium. In closed systems, the sum of charges always remains constant.

2.1.2 Interface conditions at a surface of different media

The transition from one material to a different one leads to a discontinuity. At the interface of two materials, as illustrated in figure 2.1, the behaviour of electromagnetic fields are described by general interface conditions (here in scalar form), which are derived from Maxwell equations:

$$E_{t2} - E_{t1} = 0 \tag{2.10}$$

$$H_{t2} - H_{t1} = J_s \tag{2.11}$$

$$D_{n2} - D_{n1} = \sigma_q \tag{2.12}$$

$$B_{n2} - B_{n1} = 0 \tag{2.13}$$

$$J_{n2} - J_{n1} = -\frac{\partial \sigma_q}{\partial t} \tag{2.14}$$

σ_q is the surface charge density at the boundary surface and J_s the surface current density which indicates the current per unit surface at the interface. The indices n and t refer to the normal and tangential components of the fields. Perfect conductors are related to a surface current density and perfect insulators to a surface charge density at the interface.
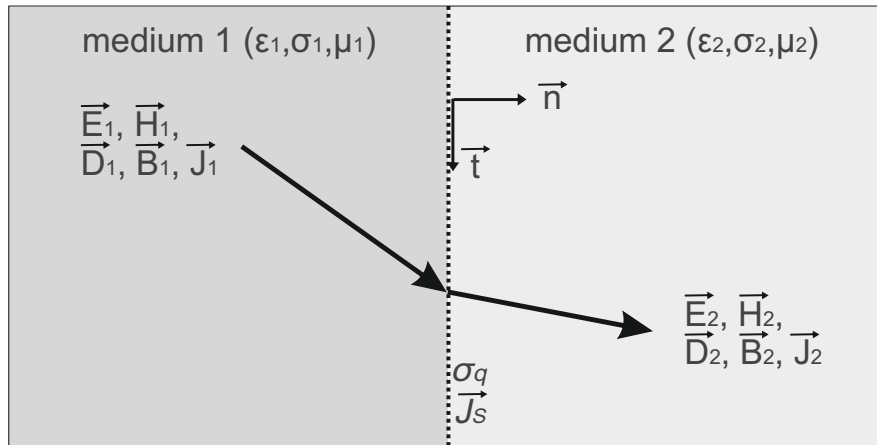
FIGURE 2.1: Behaviour of electromagnetic fields and fluxes at the interface of two media. The interface is located between two different regions, each with its own material parameters ϵ, σ and μ. General conditions as shown in equations (2.10)-(2.14) characterise the behaviour of the fields $\vec{E}$ and $\vec{H}$ and their corresponding fluxes $\vec{D}$, $\vec{B}$ and current $\vec{J}$ at the interface of the two media. A surface charge density σ_q and a surface current density $\vec{J_s}$ are assumed at the surface of the boundary. Furthermore a tangential $\vec{t}$ and normal vector $\vec{n}$ to the surface is illustrated.

2.1.3 Perturbation due to a spherical object in a uniform electric field

When an object is placed within a uniform electric field, the shape of the initial field is perturbed. This is caused by charge distributions on the object surface and within the object. They constitute an additional electric field which overlays the original field. The following section addresses the mathematical description of the influence of a spherical object on an electric field.

As illustrated in figure 2.2, a sphere with radius a is placed in an initially uniform electric field $\vec{E_0}$, which is oriented along the z-direction. A general solution to describe the perturbation $\delta\varphi(\vec{r})$ due to the sphere at a point $\vec{r}$ outside the sphere has to be found. The solution also depends on material properties such as the permittivity ϵ_2 and conductivity σ_2 of the sphere and the permittivity ϵ_1 and conductivity σ_1 of the surrounding medium.

For the boundary value problem to be solved it has to be assumed that there are no free charges in the vicinity of the sphere. Thus, the following boundary conditions can be assumed by the general interface conditions as already introduced in equations (2.10)-(2.14). Equation (2.10) shows that the tangential component of $\vec{E}$ is continuous:

$$E_{t1} = E_{t2} \tag{2.15}$$

A partial derivative of equation (2.12) with respect to the time t and substituted in equation (2.14) results in:
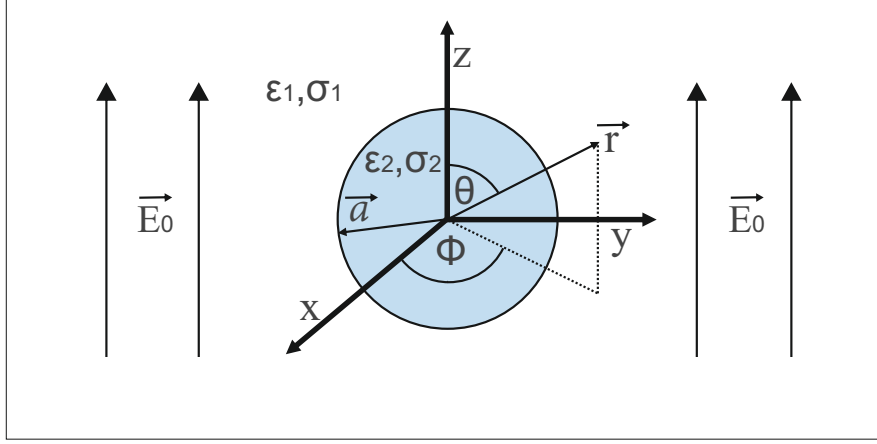
FIGURE 2.2: Spherical object in a uniform electric field. At the origin, a sphere with radius a, the permittivity ϵ_2 and conductivity σ_2 is placed in a medium with permittivity ϵ_1 and conductivity σ_1. The initially uniform electric field $\vec{E_0}$ shows in direction of the z-axis. θ represents the zenith angle and ϕ the azimuth angle.

$$J_{n2} - J_{n1} = \frac{\partial D_{n1}}{\partial t} - \frac{\partial D_{n2}}{\partial t} \tag{2.16}$$

Taking equations (2.5) and (2.7) into account, this results in the second boundary condition

$$\sigma_1 E_{n1} + \epsilon_1 \frac{\partial E_{n1}}{\partial t} = \sigma_2 E_{n2} + \epsilon_2 \frac{\partial E_{n2}}{\partial t} \tag{2.17}$$

It should be noted that the electrical resistivity ρ is defined as the inverse of the electrical conductivity σ:

$$\rho = \frac{1}{\sigma} \tag{2.18}$$

2.1.4 Solution of boundary-value problem by solving Laplace's equation

An additional field quantity of Maxwell's equations is the electrostatic potential φ. Under static conditions, the electric field $\vec{E}$ is equal to the negative gradient of the potential φ:

$$\vec{E} = -\vec{\nabla}\varphi \tag{2.19}$$

Application of the divergence to equation (2.19) and substitution of equations (2.1) and (2.5) results in Poisson's equation:

17

$$\Delta\varphi = -\frac{\rho_q}{\epsilon} \tag{2.20}$$

Many electrodynamic questions can be solved by means of Poisson's equation. A solution for this equation can be found by calculating the electrical potential φ for a given charge density distribution. If the charge density is zero (space of no free charge), the following Laplace's equation is obtained:

$$\Delta\varphi = 0 \tag{2.21}$$

The problem to be solved here satisfies the Laplace's equation in spherical coordinates. In spherical coordinates (r,θ,ϕ) the Laplace equation $\Delta\varphi(\vec{r})$ in three dimensions is given by:

$$\Delta\varphi(\vec{r}) = \frac{1}{r^2}\frac{\partial}{\partial r}\left(r^2\frac{\partial\varphi}{\partial r}\right) + \frac{1}{r^2 sin\theta}\frac{\partial}{\partial\theta}\left(sin\theta\frac{\partial\varphi}{\partial\theta}\right) + \frac{1}{r^2 sin^2\theta}\frac{\partial^2\varphi}{\partial\phi^2} \tag{2.22}$$

In order to solve the elliptic Partial Differential Equation (PDE) of this Laplace's equation, boundary conditions are required. An approach to obtain a solution by separation of variables is chosen. It is assumed that

$$\varphi(r,\theta,\phi) = F(r,\theta)\,\Phi(\phi) \tag{2.23}$$

The boundary-value problem as depicted in figure 2.2 exhibits a rotational symmetry about the z-axis (azimuthal symmetry). Consequently, the general solution for this problem is independent of ϕ. The advantage of this is that only two ordinary differential equations have to be considered and solved separately. Finally, the coefficients have to be determined by taking the boundary conditions into account because the PDEs are always defined on a region. A solution for this scenario is defined as follows:

$$\varphi(r,\theta) = \sum_{l=0}^{\infty}\left[A_l r^l + B_l r^{-(l+1)}\right]P_l(cos\theta) \tag{2.24}$$

A detailed derivation for this solution presented in equation (2.24) can be found in Jackson (1999, Chapter 3: Boundary-value Problems in Electrostatics II).

$P_l(cos\theta)$ are Legendre polynomials. The coefficients A_l and B_l have to be determined for $(r = a)$ in consideration of the boundary conditions as defined by equations (2.15) and (2.17). In addition, the boundary condition in which r goes towards infinity $(r \to \infty)$ is

observed. The applied external and constant electric field is $\vec{E}_0 = (0, 0, \vec{E}_0) = E_0 \vec{e}_z$. The first case to be investigated is the limes $r \rightarrow \infty$. Taking equation (2.19) into account, the electrical potential difference φ between the two points A and B can be written as:

$$\varphi = \varphi_B - \varphi_A = -\int_A^B \vec{E}_0 \ d\vec{s} = -\frac{W}{q_0} \tag{2.25}$$

The electrical potential is equivalent to the amount of work W required in bringing a positive test charge q_0 from a reference point to an arbitrary point within the electric field. Here, A is chosen as the reference point, assumed to be in infinity ($A = \infty$) and $B = r$.

$$\varphi_r - \varphi_\infty = -\int_\infty^r \vec{E}_0 \ d\vec{s} = -E_0 \int_\infty^r \ ds \tag{2.26}$$

At infinity the potential is referenced to zero and the applied uniform electric field is assumed in z-direction. Integrating the above equation (2.26) according a simple path s (for example a straight line) from infinity to r gives the potential associated with the constant and unperturbed field:

$$\varphi_{r \rightarrow \infty}(r, \theta) = -E_0 z = -E_0 r \ cos\theta \tag{2.27}$$

Inside the sphere ($r < a$) the interior potential φ_2 is

$$\varphi_2(r, \theta) = \sum_{l=0}^{\infty} A_l r^l P_l(cos\theta) \tag{2.28}$$

Compared to the general solution described in equation (2.24), there are no terms with B_l because the origin ($r = 0$) lies within the volume to be considered. In that case, all B_l have to be set to zero, otherwise the potential would diverge at the origin and that would not correspond to the physical model.

Outside the sphere ($r > a$) the exterior potential φ_1 is

$$\varphi_1(r, \theta) = \sum_{l=0}^{\infty} \left[C_l r^l + D_l r^{-(l+1)} \right] P_l(cos\theta) \tag{2.29}$$

Thus, the potentials inside and outside are expanded in spherical harmonics, which represent homogeneous polynomial solutions of the Laplace's equation shown in equation (2.21).

The potential described in equation (2.28) is a Legendre polynomial of order 1, hence further considerations need to be performed only to this order. Consequently, the potential inside the sphere is given by

$$\varphi_2(r,\theta) = Ar\,cos\theta \tag{2.30}$$

and the potential outside can be calculated as

$$\varphi_1(r,\theta) = Cr\,cos\theta + \frac{D}{r^2}cos\theta \tag{2.31}$$

At infinity, the distortion of the field caused by the sphere tends to zero, therefore according to equation (2.27) the result for the coefficient C is

$$C = -E_0 \tag{2.32}$$

The two remaining coefficients A and D have to be determined under consideration of the interface conditions at $(r = a)$. The tangential component of the electric field $\vec{E}$ is continuous as shown in equation (2.15). From this, it follows that the potential at this interface is continuous. Therefore, equation (2.30) and (2.31) can be equated and C can be substituted according to equation (2.32). This results in:

$$A = \frac{D}{a^3} - E_0 \tag{2.33}$$

Also the normal component of the the electric displacement field $\vec{D}$ is continuous across the surface. In addition it is assumed that the potential and thus the electric field have sinusoidal time dependence. This approach is chosen to allow the use of a sinusoidal source to generate the electric field that avoids electrolytic effects.

$$\varphi(\vec{r},t) = \varphi(\vec{r})e^{i\omega t} \quad \text{and} \quad \vec{E}(\vec{r},t) = \vec{E}(\vec{r})e^{i\omega t} \tag{2.34}$$

where ω is the angular frequency. Thus, the problem is quasi-static for which the time dependency of the current density can be neglected (Jackson 1999). The advantage

of using the description in equation (2.34) can be found in the calculation of the time derivative of the complex function:

$$\frac{\partial}{\partial t} e^{i\omega t} = i\omega\, e^{i\omega t} \tag{2.35}$$

It simplifies the partial derivation over time, because the result is a factor.

The boundary condition depicted in equation (2.17) combined with equation (2.34) and (2.35) imply the following condition at $(r = a)$:

$$(\sigma_1 + i\omega\epsilon_1)\frac{\partial\varphi_1}{\partial r}\bigg|_{r=a} = (\sigma_2 + i\omega\epsilon_2)\frac{\partial\varphi_2}{\partial r}\bigg|_{r=a} \tag{2.36}$$

The calculation can be simplified by using the following substitutions

$$\psi_1 = (\sigma_1 + i\omega\epsilon_1) \tag{2.37}$$

$$= \frac{\xi_1}{\rho_1} \qquad \text{with} \qquad \xi_1 = 1 + i\omega\epsilon_1\rho_1 \tag{2.38}$$

$$\psi_2 = (\sigma_2 + i\omega\epsilon_2) \tag{2.39}$$

$$= \frac{\xi_2}{\rho_2} \qquad \text{with} \qquad \xi_2 = 1 + i\omega\epsilon_2\rho_2 \tag{2.40}$$

After inserting equation (2.32) in equation (2.31), this result and equation (2.30) can be used to calculate the outcome of equation (2.36) as follows:

$$\psi_1\left(-E_0 - \frac{2D}{a^3}\right) = \psi_2 A \tag{2.41}$$

Reorganization of the solution results in the following expression for A:

$$A = \frac{\psi_1}{\psi_2}\left(-E_0 - \frac{2D}{a^3}\right) \tag{2.42}$$

Equating equations (2.42) and (2.33) leads to

$$\frac{D}{a^3} - E_0 = \frac{\psi_1}{\psi_2}\left(-E_0 - \frac{2D}{a^3}\right) \tag{2.43}$$

Rearranging for the coefficient D results in

$$D = E_0 a^3 \left(\frac{\psi_2 - \psi_1}{\psi_2 + 2\psi_1} \right) \tag{2.44}$$

Substituting back according to equations (2.37) and (2.39) results in

$$D = E_0 a^3 \left(\frac{(\sigma_2 + i\omega\epsilon_2) - (\sigma_1 + i\omega\epsilon_1)}{(\sigma_2 + i\omega\epsilon_2) + 2(\sigma_1 + i\omega\epsilon_1)} \right) \tag{2.45}$$

$$= E_0 a^3 \left(\frac{\sigma_2 - \sigma_1 + i\omega(\epsilon_2 - \epsilon_1)}{\sigma_2 + 2\sigma_1 + i\omega(\epsilon_2 + 2\epsilon_1)} \right) \tag{2.46}$$

This solution of D is based on the conductivity σ and the permittivity ϵ of the medium and object as dependend material parameters.

However, if equations (2.38) and (2.40) are used for back substitution as in Rasnow (1996), this leads to a result of D depending on resistivity ρ and permittivity ϵ of the medium and object.

$$D = E_0 a^3 \left(\frac{\frac{\xi_2}{\rho_2} - \frac{\xi_1}{\rho_1}}{\frac{\xi_2}{\rho_2} + 2\frac{\xi_1}{\rho_1}} \right) \tag{2.47}$$

$$= E_0 a^3 \left(\frac{\xi_2\rho_1 - \xi_1\rho_2}{\xi_2\rho_1 + 2\xi_1\rho_2} \right) \tag{2.48}$$

$$= E_0 a^3 \left(\frac{\rho_1 - \rho_2 + i\omega\rho_1\rho_2(\epsilon_2 - \epsilon_1)}{\rho_1 + 2\rho_2 + i\omega\rho_1\rho_2(\epsilon_2 + 2\epsilon_1)} \right) \tag{2.49}$$

This result can also be obtained by using equation (2.18) to replace the conductivities in equation (2.46) by resistivities.

Consequently, a new term – the contrast factor χ – can be defined for the fractions in equations (2.46) and (2.49):

$$\chi = \frac{\sigma_2 - \sigma_1 + i\omega(\epsilon_2 - \epsilon_1)}{\sigma_2 + 2\sigma_1 + i\omega(\epsilon_2 + 2\epsilon_1)} = \frac{\rho_1 - \rho_2 + i\omega\rho_1\rho_2(\epsilon_2 - \epsilon_1)}{\rho_1 + 2\rho_2 + i\omega\rho_1\rho_2(\epsilon_2 + 2\epsilon_1)} \tag{2.50}$$

Now also the coefficient A can be determined to characterize the behavior inside the sphere. Therefore, the previously determined result of D has to be inserted in equation (2.42).

$$A = -\left(\frac{3}{2 + \frac{\psi_2}{\psi_1}} \right) E_0 \tag{2.51}$$

Substitution back according to equations (2.37)-(2.40) leads to

$$A = -\left(\frac{3}{2 + \frac{(\sigma_2 + i\omega\epsilon_2)}{(\sigma_1 + i\omega\epsilon_1)}}\right) E_0 = -\left(\frac{3}{2 + \frac{(1 + i\omega\epsilon_2\rho_2)\rho_1}{(1 + i\omega\epsilon_1\rho_1)\rho_2}}\right) E_0 \qquad (2.52)$$

The second contrast factor Γ to characterize the behavior inside the sphere is defined as follows:

$$\Gamma = \frac{(\sigma_2 + i\omega\epsilon_2)}{(\sigma_1 + i\omega\epsilon_1)} = \frac{(1 + i\omega\epsilon_2\rho_2)\rho_1}{(1 + i\omega\epsilon_1\rho_1)\rho_2} \qquad (2.53)$$

Consequently, the potential inside the sphere according to equation (2.30), (2.52) and (2.53) is

$$\varphi_2(r, \theta) = -\left(\frac{3}{2 + \Gamma}\right) E_0 r \, cos\theta \qquad (2.54)$$

$$= -\left(\frac{3}{2 + \Gamma}\right) \vec{E}_0 \cdot \vec{r} \qquad (2.55)$$

$$= \left(\frac{3}{2 + \Gamma}\right) \varphi_{r\to\infty} \qquad (2.56)$$

This equation shows, that only the second contrast factor Γ, which defines the relationship between the material parameters, characterises the potential inside the spherical object. In perfect conductors, as illustrated in figure 2.3(a), the electrical induction causes that the electric field inside the object is zero and the potential at the boundary is constant. The physical reason for this is that free charges on the conductive object are redistributed by the electrical induction of the charges of the applied field. Charges on the surface of the conductor are induced such that the field within the object is canceled. In perfect dielectrics as depicted in figure 2.3(b), an electric field can be found on the surface and inside the object due to the polarization charge, which is opposed to the applied field. Even though there are only few free charges available in dielectric objects, a transfer of charges can also accur over short distances caused by the presence of the applied electric field.

According to equation (2.31) and (2.32), the potential outside the sphere can be described as:

$$\varphi_1(r,\theta) = -E_0 r\, cos\theta + E_0 \frac{a^3}{r^2}\, cos\theta\, \chi \tag{2.57}$$

$$= -\vec{E}_0 \cdot \vec{r} \quad + \vec{E}_0 \cdot \vec{r} \left(\frac{a}{r}\right)^3 \chi \tag{2.58}$$

$$= \quad \varphi_{r\to\infty} \quad + \quad \delta\varphi(\vec{r}) \tag{2.59}$$

Equation (2.59) shows that the initialized potential φ_∞ is superposed by a dipole potential $\delta\varphi(\vec{r})$ specified as

$$\delta\varphi(\vec{r}) = \vec{E}_0 \cdot \vec{r} \left(\frac{a}{r}\right)^3 \chi \tag{2.60}$$

This is the desired analytical description of the perturbation due to the spherical object in a uniform electric field. It shows that the separation of charge is always responsible for an influenced object, which becomes an electrical dipole. In consequence of the sinusoidal time dependence of the potential, a complex-valued character of the amplitude or phase shift is to be taken into account.

2.2 Numerical description of the perturbed electric field by means of FEM

As shown in the previous section 2.1, the direct analytical solution of the Laplace's or Poisson's equation solely depends on the chosen boundary conditions and optimal geometrical requirements, such as spherical symmetry of the object set into the field. However, if these specifications cannot be maintained, it is possible that only a numerical solution can be considered instead of an analytical one.

Numerical simulation is used as an important tool in this work. First 2D-numerical computer simulations of active electrolocation have been implemented by Heiligenberg (1975) to calculate the electric field of the fish and distortions caused by objects. Subsequent studies (Hoshimiya et al. 1980; Rasnow et al. 1989) and (Babineau et al. 2006) made use of the finite element method (FEM) in which the electric field of the fish was treated as an electrostatic boundary-value problem to be modelled and solved. The study here will use FEM with high precision to design the sensor-emitter ensemble by simulating the electrical dipole field and its distortion by objects. In addition to real physical measurements, the results of simulation will be used in the development of
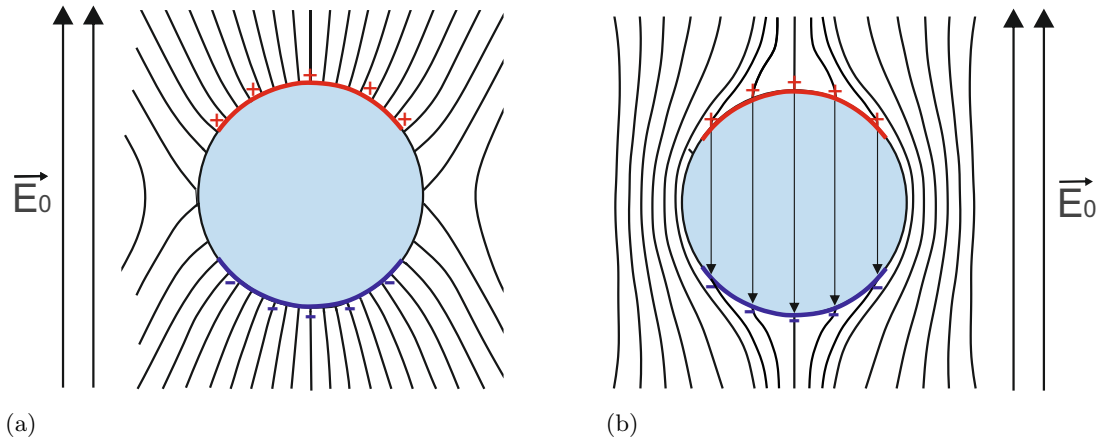
FIGURE 2.3: Example of a conductive and dielectric spherical object in uniform electric field. (a) A perfect conductor is placed in a uniform electric field. Due to induction, the influence of the applied uniform electric field effects the redistribution of the electrical charge within the object. At the surface of the conductor, the potential is constant at any point. Outside the sphere, this surface charge generates a dipole field. In addition, the potential of the surface charge compensates the applied field so that the field inside the object is zero. (b) A perfect dielectric sphere in a uniform electric field. The polarisation charge at the surface is responsible for an opposed electric field inside the object. The shapes of the fields themselves are only determined by the relationships of the material parameters, as described by the contrast factors Γ and χ for the potential inside and outside the sphere. For example an object of infinite permittivity is mathematically identical to a perfect conductive object.

suitable electrolocation strategies as ground truth to evaluate the simplified analytical solution. The numerical approach used here is the finite element method (FEM) (Clough 1960) in its implementation in the software framework COMSOL Multiphysics® v. 5.2 (Comsol Multiphysics GmbH, Göttingen, Germany).

2.2.1   Physical background for using COMSOL's AC/DC module

The FEM-based electric field problem considered here requires modeling and simulation based on the AC/DC module (COMSOL 2015) that also provides the electrostatics interface and the electric currents interface. Both interfaces solve equation (2.19) for the scalar electric potential φ as the dependent variable. Depending on material properties of the object and the medium, either the problem can be solved by the electrostatics interface, in which the permittivities appear in the calculation or by the electric currents interface, in which the conductivities are the significant material properties. COMSOL's electrostatic interface numerically solves the Poisson's equation as shown in equation (2.20) in which the electric potential φ is the dependent variable in consideration of defined boundary conditions and initial values.

To compute the electric field distribution and stationary electric currents in conductive media, the electric current interface has to be used. Here it is assumed that there are no temporal charges but a flow of electric currents. The fundamental equation for this is Ohm's law, which was previously introduced in equation (2.7). It describes the linear relation between the current density $\vec{J}$, the product of the electric field $\vec{E}$ and the conductivity σ. The current source Q can be defined by the static form of the equation of continuity as shown in equation (2.9)

$$Q = \vec{\nabla} \cdot \vec{J} \tag{2.61}$$

From this the following Poisson's source equation can be calculated by inserting equation (2.19) in equation (2.7) followed by a substitution in equation(2.61).

$$\Delta\varphi = -\frac{Q}{\sigma} \tag{2.62}$$

This equation is numerically solved by COMSOL's electric current interface and again, the electric potential is used as the dependent variable. Based on equations (2.20) and (2.62) it is possible to numerically calculate the electric field.

2.2.2 Modeling process by using COMSOL

In general, the AC/DC module is used to solve the previously described partial differential equations in consideration of initial and boundary conditions. The modeling process by using COMSOL (COMSOL 2016) is shown in figure 2.4 by means of a flow chart. Basically, the interface is composed of the preprocessing, the processing and the postprocessing step. The preprocessing step contains the global definition, the abstraction in which the model has to be specified and the modeling step to generate the geometry, define the materials, the physics model including the boundary conditions and the meshing. In the processing step the solver and its modifiable options for calculation (study steps) has to be configured to solve the model. Finally the postprocessing step is used to analyze and to interpret the results. The FEM-results can also be visualized by COMSOL. For example, contour and isosurface plots can be generated in a 2D-domain.

2.2.3 Solution of the Poisson's/Laplace's equation in 2D based on FEM

The concept of numerical methods is not to get an exact solution of the problem but partial solutions as discrete components, which have to be combined to achieve an approximation
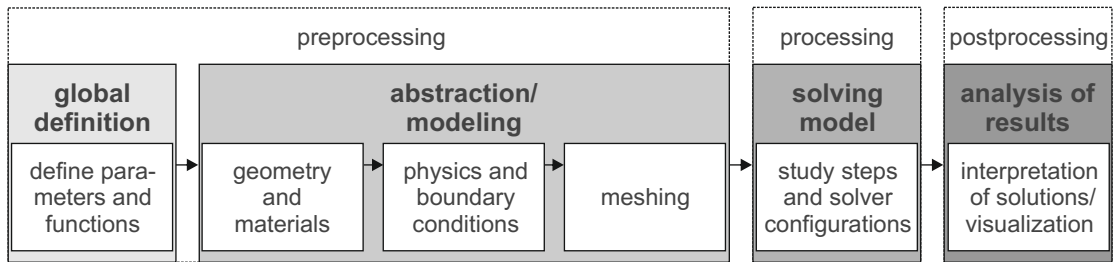
FIGURE 2.4: Flow chart of main steps of the modeling process in COMSOL. The process can be devided into three general steps from left to right. The preprocessing step is intended to define the global definitions including the parameters and functions and to perform the abstraction and modeling of the problem to be solved by FEM. For this, the dimension, the geometry and the material properties are defined. Subsequently, the physics and boundary conditions are specified. The meshing completes the modelling process. This is followed by the second step, in which the model is to be solved. This processing step includes the solver configurations and the study steps which have to be defined. Finally, the postprocessing step is used to analyze and interpret the results, which also can be visualized.

of the total solution. Explanations and calculations of the numerical approach shown in this subsection are based on the following literature: (Silvester and Ferrari 1996; Schwab 2013). The general procedure of solving the electromagnetic problem, which has to be considered here, is based on the method of Rayleigh-Ritz (Rayleigh 1877; Ritz 1908) and Galerkin's method of mean weighted residuals (Fairweather 1978). In general, these methods are used to construct a discretized form (weak form) of a simple 2D limit boundary-value problem based on its strong formulation. In order to obtain a numerical solution of the electric field and its perturbation by an object, the method of finite elements can be divided into three principal steps:

- Modeling and discretization of the 2D-domain

- Determination of the local element equations based on interpolation by using shape functions for minimizing the potential energy

- Assembling the global system equations to solve the linear system under consideration of the boundary conditions

Modeling and discretization of the 2D-domain

At first, the entire 2D-domain used for FEM-calculations, has to be modelled. The problem which has to be examined is the distortion of the electric field by a spherical object. The domain is discretized into a number of finite elements and nodes as depicted in figure 2.5(a). The process is also known as meshing. When discretizing, it is important to consider that neither overlaps nor holes are created within any region. In addition,

the elements shouldn't have too acute angles (H. R. Schwarz 1991). The domain to be observed here includes material interfaces, thus the mesh has to be adapted to this boundaries. Here, the 2D-grid is composed of different element types of triangles as depicted in figure 2.5(b).

(a)   (b)
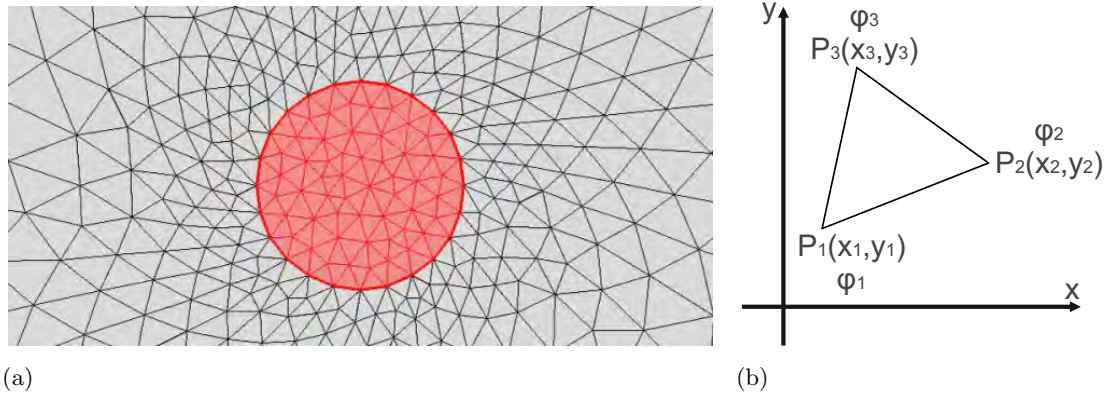
FIGURE 2.5: Discretized 2D-domain for calculation by FEM. (a) The region considered here contains a spherical object, which is colored in red. It is devided into a finite number ob subregions (finite elements). (b) Triangular FEM-element. Each finite element is having the basic form of a triangle which is set up from three points P_1 - P_3 with corresponding coordinates $(x_1, y_1) - (x_3, y_3)$ and potential φ_1 - φ_3. The physical characteristics of each finite element can be obtained through their simple geometry and well known basic functions. The solution of Poisson's/Laplace's equation for each finite element can be approximated by a polynomial function.

This geometric structure is useful to determine the physical characteristics of each element in a simple way in order to divide a difficult field problem into many small simple field problems.

Determination of the local element equations based on interpolation by using shape functions for minimizing the potential energy

In consideration of the initial and boundary conditions of the model, a numerical solution of the Laplace's/Poisson's equation can be obtained. It represents an approximation of the direct solution to the PDE which has to be computed for each finite element.

The basic idea of the FEM is to approximate the exact function $\varphi(\vec{x})$ with $\varphi^N(\vec{x})$. This is a linear combination of linear trial functions $P_e(\vec{x})$ which are piecewise continuously differentiable and their initially unknown coefficients φ_e.

$$\varphi(\vec{x}) \approx \varphi^N(\vec{x}) \equiv \sum_{e=1}^{N} P_e(\vec{x})\, \varphi_e \tag{2.63}$$

These trial functions are used to create an N-dimensional space comprising the approximate solution. In a subsequent step, the error (also called residual) between the exact and approximated solution has to be minimized. The residual quantifies the error of approximation at any point of the domain. The unknown coefficients φ_e have to be determined, so that the residual on the domain will be minimized. The coefficients φ_e contain the physical characteristics.

Equations (2.20) and (2.62) show the strong form of the governing Poisson's/Laplace's equation, which represent partial differential equations (PDEs). A PDE can only have a unique solution by using boundary conditions. Here, a Dirichlet boundary condition is assumed along the boundary of the domain, in which for example the potential φ is fixed similar to a voltage source.

For each finite element, an approach is applied for the energy it contains. This energy includes the wanted parameter, here the potential. The energy of the complete solution area has to be minimized. This leads to a linear system of equations for the unknown parameters.

In a first step, a potential distribution function has to be set up for each single finite element e. Based on interpolation, the potential in one 2D-element is approximated by a linear polynomial function as shown in equation (2.64).

$$\varphi_i^{(e)}(x,y) = a_i^{(e)} + b_i^{(e)} x + c_i^{(e)} y \tag{2.64}$$

Thus, the solution is assumed to be a function of the spatial coordinates where the coefficients $a^{(e)}$, $b^{(e)}$ and $c^{(e)}$ have to be determined. By using the triangular FEM-mesh for the 2D-problem shown in figure 2.5, i runs from 1 to 3, thus representing the nodes of the triangle.

Correspondingly, the potentials at the three nodes can be described as

$$\underbrace{\begin{bmatrix} \varphi_1^{(e)} \\ \varphi_2^{(e)} \\ \varphi_3^{(e)} \end{bmatrix}}_{\varphi_i^{(e)}} = \underbrace{\begin{bmatrix} 1 & x_1 & y_1 \\ 1 & x_2 & y_2 \\ 1 & x_3 & y_3 \end{bmatrix}}_{B} \begin{bmatrix} a^{(e)} \\ b^{(e)} \\ c^{(e)} \end{bmatrix} \tag{2.65}$$

This linear equations contain the three unknown coefficients $a^{(e)}$ - $c^{(e)}$. They can be uniquely determined by resorting to Cramer's rule which expresses the solution in terms of determinants of the matrix B.

$$a^{(e)} = \frac{det\, B_{a^{(e)}}}{det\, B}, \quad b^{(e)} = \frac{det\, B_{b^{(e)}}}{det\, B}, \quad c^{(e)} = \frac{det\, B_{c^{(e)}}}{det\, B} \tag{2.66}$$

with

$$det\, B = [(x_2 - x_1)(y_3 - y_1) - (x_3 - x_1)(y_2 - y_1)] \tag{2.67}$$

The determinants in the numerators of equations (2.66) are formed by replacing the first column of B with vector $\varphi_i^{(e)}$ for $det\, B_{a^{(e)}}$, the second column of B with vector $\varphi_i^{(e)}$ for $det\, B_{b^{(e)}}$ and the third column of B with vector $\varphi_i^{(e)}$ for $det\, B_{c^{(e)}}$.

The area of the triangular element is denoted by $A^{(e)}$ and, according to analytical geometry, can be calculated based on the determinant as

$$A^{(e)} = \frac{1}{2} \left| det \begin{bmatrix} 1 & x_1 & y_1 \\ 1 & x_2 & y_2 \\ 1 & x_3 & y_3 \end{bmatrix} \right| = \frac{1}{2}[(x_2 - x_1)(y_3 - y_1) - (x_3 - x_1)(y_2 - y_1)] \tag{2.68}$$

where the numbering of the nodes is anticlockwise.

For the unknown coefficients the area of the triangle can be used to simplify the expressions when equation (2.66) is calculated. The result is:

$$a^{(e)} = \frac{1}{2A^{(e)}} \left[(x_2 y_3 - x_3 y_2)\varphi_1^{(e)} + (x_3 y_1 - x_1 y_3)\varphi_2^{(e)} + (x_1 y_2 - x_2 y_1)\varphi_3^{(e)} \right] \tag{2.69}$$

$$b^{(e)} = \frac{1}{2A^{(e)}} \left[(y_2 - y_3)\varphi_1^{(e)} + (y_3 - y_1)\varphi_2^{(e)} + (y_1 - y_2)\varphi_3^{(e)} \right] \tag{2.70}$$

$$c^{(e)} = \frac{1}{2A^{(e)}} \left[(x_3 - x_2)\varphi_1^{(e)} + (x_1 - x_3)\varphi_2^{(e)} + (x_2 - x_1)\varphi_3^{(e)} \right] \tag{2.71}$$

Here it is shown that the denominator of all obtained coefficients is always equal to twice the area of the triangle. Thus, for each individual element it can be extracted as constant in following calculations. The remaining part of the result indicates that the coefficients are described by the potentials and coordinates of the corresponding nodes. This allows to define a function of spatial coordinates according to equation (2.64).

For this, the results of equations (2.69)-(2.71) can now be substituted in equation (2.64) to determine the potential φ within the triangular element e. Transformation of the equation results in

$$\varphi^{(e)}(x,y) = N_1(x,y)\varphi_1^{(e)} + N_2(x,y)\varphi_2^{(e)} + N_3(x,y)\varphi_3^{(e)} \tag{2.72}$$

This equation includes the shape functions N_1 - N_3

$$N_1(x,y) = \frac{1}{2A^{(e)}} \left[(x_2 y_3 - x_3 y_2) + (y_2 - y_3)x + (x_3 - x_2)y \right] \tag{2.73}$$

$$N_2(x,y) = \frac{1}{2A^{(e)}} \left[(x_3 y_1 - x_1 y_3) + (y_3 - y_1)x + (x_1 - x_3)y \right] \tag{2.74}$$

$$N_3(x,y) = \frac{1}{2A^{(e)}} \left[(x_1 y_2 - x_2 y_1) + (y_1 - y_2)x + (x_2 - x_1)y \right] \tag{2.75}$$

This set of linearly independent shape functions can be interpreted as centroid coordinates of the triangle and are used by the Ritz-Galerkin method to approximate the defined solution on a given triangular mesh. The potential field distribution can be described although the potentials at the nodes are unknown. For this, the potentials will be adjusted so that the global energy stored in the field becomes minimal. This implies that the global energy minimum corresponds to the exact solution. In summary, it can be concluded that the principle approach of FEM is to minimize the stored potential energy in the field. Instead of solving a second order PDE (strong form), an equation can be solved which consists the square of the first derivatives of the potential (weak form).

For this, the following variational approach has to be performed. At first, equation (2.72) has to be partially derived to x and y.

$$\frac{\partial \varphi}{\partial x} = \frac{1}{2A^{(e)}} \left[(y_2 - y_3)\varphi_1 + (y_3 - y_1)\varphi_2 + (y_1 - y_2)\varphi_3 \right] \tag{2.76}$$

$$\frac{\partial \varphi}{\partial y} = \frac{1}{2A^{(e)}} \left[(x_3 - x_2)\varphi_1 + (x_1 - x_3)\varphi_2 + (x_2 - x_1)\varphi_3 \right] \tag{2.77}$$

The total electrostatic potential energy W in a small volume Δv of the field in consideration of equations (2.5) and (2.19) can be calculated as

$$W_{\Delta v} = \frac{1}{2} \iiint_{\Delta v} \vec{E} \cdot \vec{D} \, \mathrm{d}v = \frac{1}{2} \epsilon \iiint_{\Delta v} \vec{E}^2 \mathrm{d}v = \frac{1}{2} \epsilon \iiint_{\Delta v} (\vec{\nabla}\varphi)^2 \mathrm{d}v \tag{2.78}$$

$$= \frac{1}{2} \epsilon \iiint_{\Delta v} \left[\left(\frac{\partial \varphi}{\partial x}\right)^2 + \left(\frac{\partial \varphi}{\partial y}\right)^2 + \left(\frac{\partial \varphi}{\partial z}\right)^2 \right] \mathrm{d}v \tag{2.79}$$

The potential distribution to be determined here is related to a two-dimensional field, which can be regarded as a cross-sectional area of the three-dimensional case and thus independent of the z-axis. Consequently, the energy per unit of length Δz can be written as

$$\frac{W_{\Delta v}}{\Delta z} = X^{(e)} = \frac{1}{2} \epsilon \iint\limits_{A^{(e)}} \left[\left(\frac{\partial \varphi}{\partial x}\right)^2 + \left(\frac{\partial \varphi}{\partial y}\right)^2 \right] dA^{(e)} \tag{2.80}$$

The linear element functional $X^{(e)}$ is a function of the node potentials of the respective 2D-element e, in this case of a triangle.

$$X^{(e)} = f(\varphi^{(e)}(x,y)) \tag{2.81}$$

The functional X and thus the total energy of the entire field can be calculated by summing up all individual element energies:

$$X = f(\varphi(x,y)) = \sum_{e=1}^{N} X^{(e)} \tag{2.82}$$

After equations (2.76) and (2.77) have been squared and added up, the results can be substituted in equation (2.80).

In order to determine the minimum energy, the functional must be partially derived and set to zero according to

$$\frac{\partial X^{(e)}}{\partial \varphi_1} = 0, \quad \frac{\partial X^{(e)}}{\partial \varphi_2} = 0, \quad \frac{\partial X^{(e)}}{\partial \varphi_3} = 0 \tag{2.83}$$

For each finite element this results in the following expression to identify the three unknown potentials φ_1 - φ_3

$$\frac{\epsilon}{4A^{(e)}} \underbrace{\begin{bmatrix} p_{11}^{(e)} & p_{12}^{(e)} & p_{13}^{(e)} \\ p_{21}^{(e)} & p_{22}^{(e)} & p_{23}^{(e)} \\ p_{31}^{(e)} & p_{32}^{(e)} & p_{33}^{(e)} \end{bmatrix}}_{p_{mn}^{(e)}} \underbrace{\begin{bmatrix} \varphi_1 \\ \varphi_2 \\ \varphi_3 \end{bmatrix}}_{\varphi^{(e)}} = \begin{bmatrix} 0 \\ 0 \\ 0 \end{bmatrix} \tag{2.84}$$

with

$$p_{11}^{(e)} = (y_2 - y_3)^2 + (x_3 - x_2)^2 \tag{2.85}$$

$$p_{12}^{(e)} = (y_2 - y_3)(y_3 - y_1) + (x_3 - x_2)(x_1 - x_3) \tag{2.86}$$

$$p_{13}^{(e)} = (y_2 - y_3)(y_1 - y_2) + (x_3 - x_2)(x_2 - x_1) \tag{2.87}$$

$$p_{21}^{(e)} = (y_2 - y_3)(y_3 - y_1) + (x_3 - x_2)(x_1 - x_3) \tag{2.88}$$

$$p_{22}^{(e)} = (y_3 - y_1)^2 + (x_1 - x_3)^2 \tag{2.89}$$

$$p_{23}^{(e)} = (y_3 - y_1)(y_1 - y_2) + (x_1 - x_3)(x_2 - x_1) \tag{2.90}$$

$$p_{31}^{(e)} = (y_2 - y_3)(y_1 - y_2) + (x_3 - x_2)(x_2 - x_1) \tag{2.91}$$

$$p_{32}^{(e)} = (y_3 - y_1)(y_1 - y_2) + (x_1 - x_3)(x_2 - x_1) \tag{2.92}$$

$$p_{32}^{(e)} = (y_1 - y_2)^2 + (x_2 - x_1)^2 \tag{2.93}$$

The linear system as depicted in equation (2.84) corresponds to one finite triangular element e of the domain. The elements of the local coefficient matrix $p_{mn}^{(e)}$ are functions of the node coordinates. Each row represents one element node and the connection to the other two nodes of the triangle. If material parameters, such as the permittivities are not constant for all finite elements of the system, interface conditions have also to be considered in further calculations.

Assembling the global system equations to solve the linear system under consideration of the boundary conditions

Each finite element of the system is coupled to the potentials of neighboring elements. Therefore, a global system matrix P_{mn} must be constructed, based on the sum of all local element functionals. This system equation is based on the previously defined FEM-mesh containing N nodes. According to equation (2.82), the procedure is to connect the global calculation with local operations on the individual elments, as depicted in equation (2.84), which then have to be summarized.

$$P_{mn} = \sum_{e=1}^{N} p_{mn}^{(e)} \tag{2.94}$$

The coefficients of the system matrix P_{mn} are obtained by summing up the corresponding coefficients of the individual element matrices p_{mn}. The procedure will be illustrated by a simplified example as shown in figure 2.6.
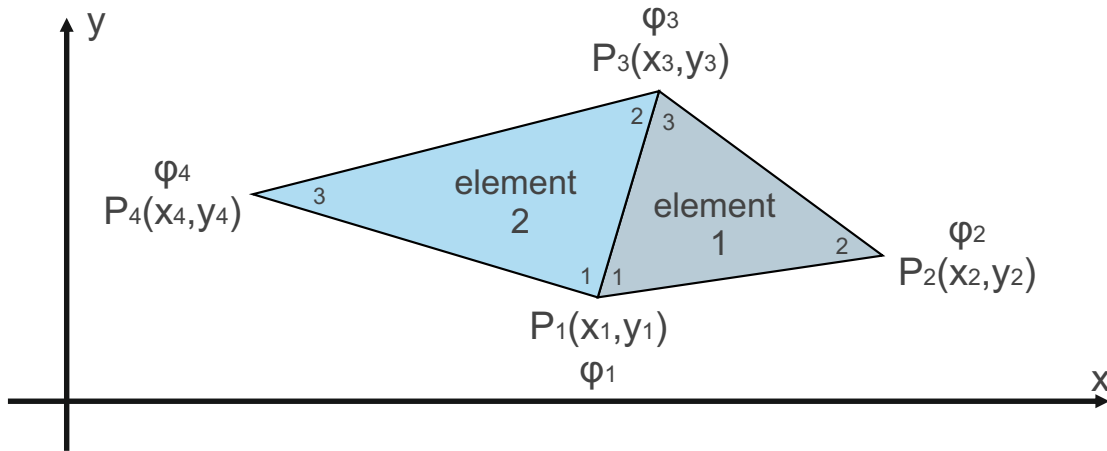
FIGURE 2.6: Simplified example to assemble a global system matrix. The system illustrated here consists of two elements with a total of four nodes. The global numeration of the potentials and also of the global nodes can be found outside, the local numbering is located inside of the single elements. For this arrangement a global coefficient/system matrix will be constructed.

The first step here is to determine equation (2.84) for each separate triangle. According to equation (2.94), these results have to be added in consideration of possibly common nodes or edges.

Hence, the global system matrix P_{mn} for the simplified example in figure 2.6 can be written as follows

$$
\underbrace{\begin{bmatrix}
p_{11}^1 + p_{11}^2 & p_{12}^1 & p_{13}^1 + p_{12}^2 & p_{13}^2 \\
p_{21}^1 & p_{22}^1 & p_{23}^1 & 0 \\
p_{31}^1 + p_{21}^2 & p_{32}^1 & p_{33}^1 + p_{22}^2 & p_{23}^2 \\
p_{31}^2 & 0 & p_{32}^2 & p_{33}^2
\end{bmatrix}}_{P_{mn}}
\begin{bmatrix}
\varphi_1 \\
\varphi_2 \\
\varphi_3 \\
\varphi_4
\end{bmatrix}
=
\begin{bmatrix}
0 \\
0 \\
0 \\
0
\end{bmatrix}
\tag{2.95}
$$

In cases where the nodes of the mesh are not connected, the entry within the global matrix is zero. For a system of N nodes the approach can be generally described as

$$
\sum_{n=1}^{N} P_{mn}\, \varphi_n = 0 \quad with \quad m = 1, 2, ..., N
\tag{2.96}
$$

Thus it is shown, that by means of numerical calculations it is possible to reduce the partial differential equations to algebraic equations. Its solution gives an approximation of the unknown potential values within the mesh and consequently of electromagnetic field quantities like the electric field or flux intensity, which can be calculated at the postprocessing stage.

The FEM-formulation of the problem results in a global system as shown in equation (2.96) consisting of N equations with N conditions. To determine the N unknown coefficients φ_n the linear system of equations must be solved by a numerical solver algorithm. However, the system of equations cannot be uniquely solved without considering the boundary conditions. If the potentials of the nodes at the boundary are known, the lines within the global system of linear equations which represent these boundary nodes can be transferred into a reduced form.

To obtain solutions of linear system, two classes of solver algorithms are provided by COMSOL, the direct and iterative solvers.

Direct solvers use the lower-upper (LU) decomposition (Turing 1948), which is a matrix form of Gaussian elimination. However, considering that there are many nodes within the FEM-mesh that are not connected to each other leads to a large number of entries in the global system matrix which are set to zero. Therefore, an iterative method to solve the linear systems of equations is useful. For this, the conjugate gradient method (Hestenes and Stiefel 1952) is implemented.

In order to achieve a more accurate result, the FEM-mesh has to be modified. This can be achieved by increasing the number of finite elements and/or the degree of the polynomial of the shape functions.

2.3 Dipole field perturbation and its representation with electrical viewpoints

As previously described in chapter 1, weakly electric fish use their self-generated electric fields for active electrolocation. Inspired by this biological model, a simple, biomimetic abstraction of a sensor-emitter array is assumed for further considerations. Figure 2.7 shows a setup which consists of an emitter dipole and a respective orthogonally arranged pair of sensor electrodes. The emitter dipole is represented by squares marked with + for the positive and - for the negative emitter. The sensors are illustrated by circles, which are labelled with S_1 and S_2.

Figure 2.7(a) shows a symmetrical arrangement of the self-generated electric field. The field is symmetrical because it is not disturbed by any object. As a consequence, the sensor electrodes are situated at the same equipotential line, which leads to a measured potential difference of $\Delta\varphi = 0\,V$. The presence of an object, as shown in figure 2.7(b), distorts the field which leads to a potential difference $\Delta\varphi \neq 0$.
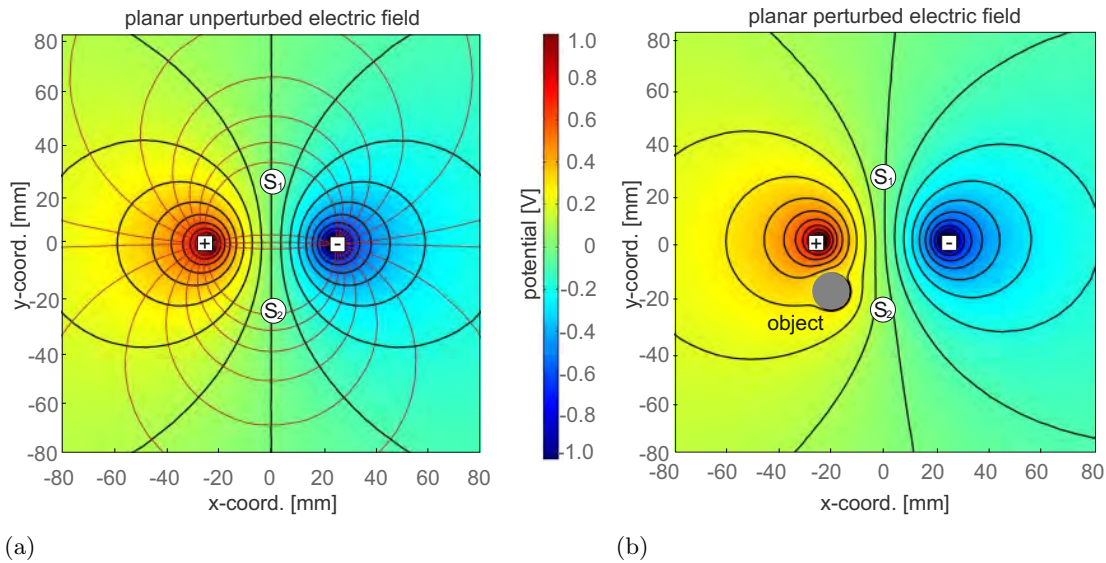
FIGURE 2.7: Biomimetic sensor-emitter setup consisting of an emitter dipole and an orthogonally arranged pair of sensor electrodes (a) Illustration of a planar unperturbed electric field. The electric field is generated by a dipole, labelled + and -. The sensor electrodes S_1 and S_2 are arranged orthogonally to the two emitter electrodes and symmetrically with respect to the origin of the coordinate system. The equipotential lines are shown in black, the field lines in red. If the field generated by the dipole is not disturbed, both sensor electrodes are located on the same equipotential line. In consequence, the potential difference $\Delta\varphi$ is 0V. (b) Planar electric field perturbed by a conducting spherical object with $r = 7\,\text{mm}$. Here the object is placed at position (-20, -20) mm which causes a field disturbance. The change of the equipotential line course leads to a potential difference which can be measured between the two sensors. The composition of object location and the observed potential difference $(\vec{x}, \Delta\varphi)$ is called electrosensory viewpoint (EV).

The composition of the measured potential difference $\Delta\varphi$ and object position $\vec{x}$ in relation to the sensor frame has been termed electrosensory viewpoint (EV_e) by Solberg et al. (2008).

$$\text{EV}_e = (\vec{x}, \Delta\varphi) \tag{2.97}$$

The index e in equation (2.97) indicates environmental parameters like size, shape, material properties of the object, the applied field and of the fluid. The collection of EV_e for each possible object location $\vec{x}$ is called the ensemble of electrosensory viewpoints (EEV). To generate an EEV, an object (in this case a sphere) is placed at each position of a grid and the respective EV is stored in the resulting EEV matrix.

$$\text{EEV}_e(\vec{x}) = (\varphi_1 - \varphi_2) = \Delta\varphi \tag{2.98}$$

Figure 2.8(a) exemplarily shows a contour plot and figure 2.8(b) a 3D-plot of an EEV.

The color code represents the potential difference $\Delta\varphi$ at each position of the grid. The contour-rings of the EEV provide information on possible object positions for a given sensor reading $\Delta\varphi$. By using a previously generated EEV, one measurement of the potential difference $\Delta\varphi$ at the sensor electrodes reduces the possible object positions to locations on symmetrical EEV contour-rings. This means that one single measurement of the potential difference does not uniquely identify the position of an object since a measured voltage difference between the sensors in principle occurs several times in the EEV and forms EEV contour-rings (equipotential line of the same potential difference). This ambiguity can be counteracted by executing shift and rotational movements of the sensor-emitter ensemble. As a result, also the respective EEV is shifted or rotated. For a fixed object position this leads to the identification of different contour-rings, one in each of the moved EEVs. Superposition of these contour-rings reduces the possible object position to intersection points of the EEVs. This approach will be examined in detail in chapter 3. Here, an optimal concatenation of active sensor movements based on numerically extracted EEVs will be investigated.

(a) (b)
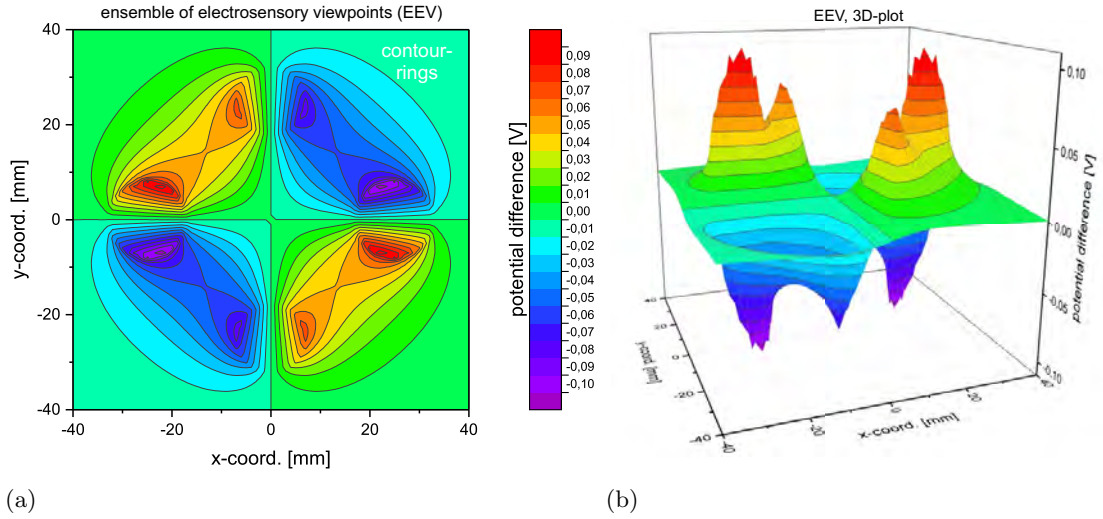
FIGURE 2.8: Ensemble of electrosensory viewpoints (EEV). (a) 2D-visualisation of the EEV. By placing the spherical object at each position of a grid, the corresponding EVs are collected in a matrix to compose an EEV. (b) 3D-plot of the EEV. The uneven appearance of the slim peaks is due to discretization effects rather than noise. For a given sensor-emitter array, the EEV consists of isopotential contour-rings and exhibits mirror symmetries. As a consequence, one measurement of the potential difference $\Delta\varphi$ reduces the possible object position to the locations on symmetrical contour-rings. Thus, a single measurement does not identify a unique object position. This issue can be tackled by moving the sensor-emitter ensemble and thus also the respective EEV.

The strategies presented in chapter 4 also use EEVs as a basis to perform active electrolocalization. Finally, in chapter 5 a fitted histogram representation of EEVs will be examined to estimate the optimal composition of movement sequences.

3

Optimal concatenation of active sensor movements based on numerically extracted EEVs

Abstract

As described in chapter 1, weakly electric fish use self-generated electric fields for active electrolocation to detect objects in their nearby environment. A vast number of electroreceptors are distributed across the skin of the electric fish which represent the sensor part of the biological system. The emitter part is represented by specialized muscle cells, located in the tail region to generate a weak electric field around the fish's body. Furthermore, fish execute stereotyped scanning movements by changing their body shape and position to obtain additional sensory information (Engelmann et al. 2009). Inspired by this biological model, a fixed, minimal scanning strategy, composed of active receptor system movements is developed which allows a unique localization of a spherical object in the vicinity of the sensor system. The derived strategy is based on the superposition of numerical extracted contour-rings of linearly shifted and/or rotated EEVs (Solberg et al. 2008). The electric field characteristics of the receptor system are modelled and simulated by means of FEM (Finite Element Method) which was introduced in section 2.2. To analyze a movement sequence, matrices of unique intersection points and respective contrast functions are introduced. The best resulting concatenation of receptor system movements consists of a linear shift, a rotation and the original EEV.

Most of the scientific results presented in this chapter have been published in:
Wolf-Homeyer et al. (2016).
This manuscript includes Jacob Engelmann and Axel Schneider as co-authors.

3.1 Active sensor movements for disambiguation of object positions

Apart from the setup of the biological electroreceptor system as depicted in figure 3.1(a) which was described in chapter 1 and which represents the general inspiration for this work, weakly electric fish also use a sophisticated repertoire of movement behaviors when approaching objects of their interest. These scanning behaviors are composed of whole body movements (Engelmann et al. 2009) as sketched in figures 3.1(b) and (c) . Furthermore, they consist of motor prototypes with rotational and translational character arranged sequentially in time (Toerring and Moller 1984; Hofmann et al. 2014).
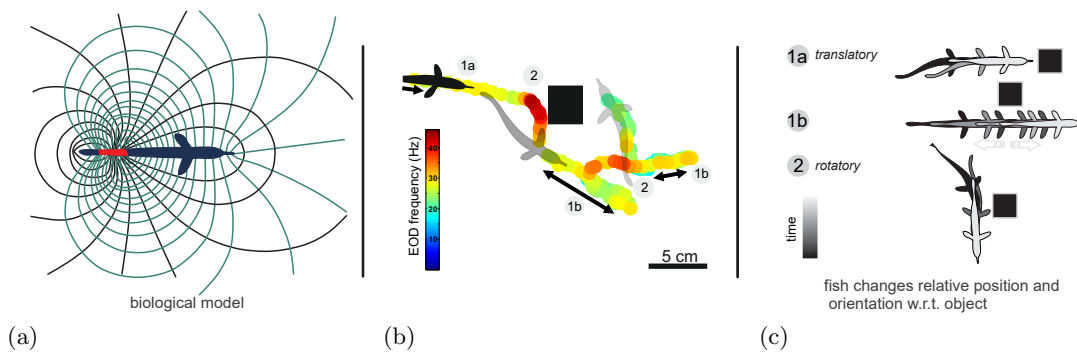
FIGURE 3.1: Exemplary sketch of electrolocation behavior of weakly electric fish. (a) The biological template use their self-generated electric field for active electrolocation. (b) In addition the fish change their relative position and orientation during electrolocation observed in recurring stereotypic motor- and electromotor behaviors. On the one hand, the active scanning movements influence the temporal sequence of sensory input (EOD frequency, middle part) and on the other hand they shape the spatial sensory input. This affects the spatial relation between the emitter organ and the objects in the environment and thus shapes the sensory input. (c) Stereotyped electromotor sequences can be analyzed and quantified (Hofmann et al. 2014). The basic motor aspects involve rotatory and linearly shifted components.

Inspired by this biological model, a scanning strategy is developed, which is based on a minimal set of optimal concatenations of active receptor system movements. The aim of this strategy is to uniquely identify the position of a spherical object in the nearby vicinity of the sensor system. To reach this goal, the biomimetic abstraction of a sensor-emitter ensemble as introduced in section 2.3, consisting of an emitter dipole and an orthogonally arranged pair of sensor electrodes is assumed. This arrangement is used to develop a minimal, yet fixed and non probabilistic scanning strategy for the movement of the whole sensor-emitter array.

The basic principle behind the scanning strategy is the measurement of the potential difference $\Delta\varphi$ between the two sensor electrodes. If there is no object within the self-generated field, as shown in figure 2.7(a), the composition of the electric field is

symmetrical and the sensor electrodes S_1 and S_2 are located at the same equipotential line. This results in a potential difference $\Delta\varphi = 0$ between both sensors. However, the presence of an object within the field as presented in figure 2.7(b) distorts it which leads to a potential difference $\Delta\varphi \neq 0$. Solberg et al. (2008) had termed the combination of the measured potential difference $\Delta\varphi$ and the location of the object in relation to the sensor frame $\vec{x}$ electrosensory viewpoint (EV_e). The collection of EV_s for each object location is called Ensemble of Electrosensory Viewpoints (EEV_e) as described in equations (2.97) and (2.98).

The observation depends on unchanging environmental parameters like size, shape, material properties of the object, the applied field and the conductivity of the fluid. This is indicated by the index e. If a generated EEV is given, a single measurement of a potential difference $\Delta\varphi$ between the sensors does not uniquely identify an object position but it reduces the position that has to be determined to locations on EEV contour-rings. Within the EEV, contour-rings occur in a point symmetrical arrangement. By shifts and rotations of the sensor-emitter ensemble, which also shifts or rotates the EEV, it is possible to solve this ambiguity. The shifted or rotated sensor system leads to a new potential difference $\Delta\varphi$ between the sensors while the unknown position of the object is unchanged. This causes a different isopotential contour which is formed in the shifted or rotated EEV. If the isopotential contours of different movements of the sensor-emitter array are superimposed, their created intersection points mark possible object positions. Solberg et al. (2008) used a particle filter approach (Stachniss and Burgard 2014) to narrow down the possible object position by the concatenation of linear shifts of the sensor-emitter array. In such an approach, each particle represents a possible object location and the direction of movement is defined in a random walk fashion by a probabilistic controller. This approach minimizes the expected variance of particles, which requires calculations of movement consequences in each time step. The described strategy of Solberg et al. (2008) only generates translational movements of the sensor system in order to localize the object. In contrast to this, this chapter describes a fixed, a-priori movement strategy consisting of a concatenation of only a few linear and rotational shifts of the sensor-emitter ensemble and the respective EEVs. Based on superimposed EEVs, a unique identification of object positions is possible. Simply because of the utilization of rotations, the strategy developed here is already closer to the described movement behavior of weakly electric fish (Hofmann et al. 2014). Furthermore, it can be easily integrated into an actively moveable technical sensor configuration.

To examine different concatenations of movements of the sensor-emitter array, EEVs of all possible rotational movements and linear shifts are created numerically based on COMSOL Multiphysics® to derive an optimal concatenation of movements. To evaluate the results, a contrast measure will be defined, which assesses the uniqueness of

a given concatenation. Additional conditions such as measurement accuracy and local topography of the EEVs have to be considered. In the end, this results in a minimal and fixed scanning strategy of rotations and linear shifts of the sensor-emitter array which can be used for further localization approaches.

3.2 Object localization by means of rotated and linearly shifted EEVs

As explained in section 2.3, the EEV describes the influence of an object onto the self-generated electric dipole field. There are several ways to characterize the perturbation of the electric field due to a spherical object. In order to implement the analytical description as shown in equation (2.60) which has the benefit of fast computation, several assumptions have to be considered. As already described in section 2.1, this equation is only applicable for a spherical object. Furthermore, Rasnow (1996) has assumed a uniform electric source field for calculations. Due to the azimuthal symmetry of the boundary-value problem the latter was later on exchanged for a dipole field by Solberg et al. (2008). However, if the simplified analytical model is used, deviations from the real solution are especially serious in those places where emitter and sensor electrodes are situated (singularities). In addition, real applications must deal with inhomogeneous fields and with objects, the shapes of which are generally different from those of ideal spheres. Because of this, detailed FEM-simulations are used in this section instead of the simplified analytical description to accurately determine field perturbations due to objects by taking their material properties into account. This numerical modelling approach is used to identify an ideal and minimal set of sensor system movements to localize objects in the electric field. Figure 2.7 exemplary shows an FEM-simulation result of a simple two-dimensional dipole model which was computed by COMSOL Multiphysics®. It represents the solution of a classical stationary electric field problem for which material properties of object and surrounding medium where considered.

As explained in detail in section 2.2, electrostatic equations are numerically solved in different ways. Depending on material properties, COMSOL's electrostatics interface or electric currents interface has to be used. The derivations of the fundamental equations (2.20) and (2.62) which are used here can also be found in chapter 2. In general however, the electric field problem which is numerically treated here solves equation (2.19) for the scalar electric potential φ as the dependent variable. This is independent of the interface (electrostatic or electric current) which is used. Based on these equations, the numerical calculation of the electric field is possible. Figure 2.7(b) exemplary depicts an

electric field distorted by an object. Thus, a potential difference $\Delta\varphi$ between the two sensor electrodes can be measured and an EEV can be generated.

Based on the previously introduced sensor-emitter array, figure 3.2(a) illustrates a contour plot of the original EEV. For this example, a spherical conducting object with radius $r = 7\,\text{mm}$ is located at position $\vec{x} = (\text{-20}, \text{-20})\,\text{mm}$. This represents the reference point for subsequent assumptions. The measured potential difference for an object at the reference point is not unique because this value also can be found along the two contours, here emphasized as black contour-rings.
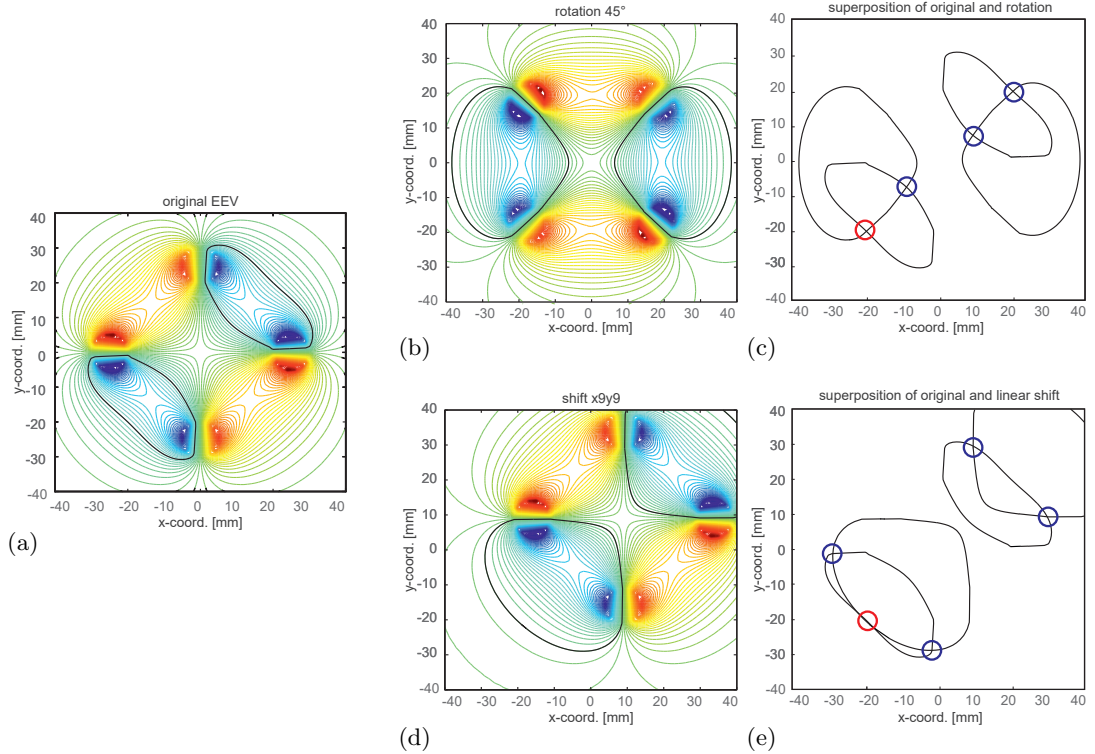
FIGURE 3.2: Strategies for active object localization based on EEVs which provide information about possible object positions. (a) EEV for a conducting object at here at reference point $\vec{x}$ (-20, -20) mm which results in a potential difference $\Delta\varphi$ measured between the sensors. All along the extracted EEV contour-rings, here marked in black, the same measured potential difference can be found. That means that a single measurement of the observed potential difference does not reveal the wanted object position. (b) The sensor-emitter ensemble and thereby also the EEV is rotated by 45° while the object is maintained fixed. This results in a new potential difference measured between the two sensor electrodes. Therefore, a new set of EEV contour-rings emerges. (c) The superposition of the contour-rings of the original and rotated EEV leads to intersections between the extracted contours. In addition to the true intersection point at (-20, -20) mm which indicates the correct object's location, three additional and symmetrically arranged possible object positions exist. (d) Same as in (b) but for a linear shift by 9 mm both in x- and y- direction of the sensor-emitter ensemble and thereby also for the EEV. A new potential difference between the sensors can be measured and new contour-rings of possible object positions can be extracted. (e) Superposition of original and linearly shifted EEV contour-rings which reduces the number of possible object locations to five intersections.

This means, that a single measurement of the observed potential difference between the sensors does not uniquely determine the position of the object but reduces it to the locations of the black marked EEV contour-rings. In order to further narrow down the object position, it is possible to rotate or shift the sensor-emitter ensemble. In figure 3.2(b), the array is rotated clockwise by 45° and thus also the respective EEV. Since the object remains in the same location but the relative orientation to the sensor-emitter array has changed as compared to figure 3.2(a) a new potential difference can be measured between the two sensor electrodes. The newly measured potential difference belongs to a new set of contour-rings, also marked in black. Once again, the identification of the object position is not unique because the object must be situated at locations along the new contour-rings. The same applies in the case, in which the sensor-emitter ensemble is linearly shifted. The example in figure 3.2(d) shows such a linearly shifted EEV. The ensemble was shifted by 9 mm both in x- and y-direction. As a result, two new contour-rings are emphasized in relation to the newly measured potential difference. The superposition of the extracted EEV contour-rings of the original and rotated EEV as shown in figure 3.2(c) and of the original and linearly shifted EEV as depicted in figure 3.2(e) is used to create intersection points. This method is used to reduce the possible object locations from contour-rings to single spots, the intersection points of the extracted EEV contour-rings.

Figure 3.3(a) shows the superposition of perfectly separated contour-rings of original and rotated EEV once again. This is to emphasize that rotational movements alone create symmetric points of intersections. Hence, for pure rotations, strictly speaking no uniqueness of object positions can be achieved. Instead, a significant 2-ambiguous prediction of the location is possible. In contrast to that, the superposition of perfectly separated contour-rings of original and linearly shifted EEV as displayed in figure 3.3(b) breaks the symmetry and results in asymmetric points of intersections. Mixed information of rotational and shifted movements, as exemplary illustrated in figure 3.3(c), leads to contour-ring intersections which reduce the possible object position to just one location. Here, the superposition of original, rotated and linearly shifted EEV detects the wanted object position at the reference point $\vec{x} = (\text{-}20, \text{-}20)$ mm.

In the subsequent sections it will be examined, how many rotational and linearly shifted movements in which combination are needed to determine the unique position of an object by means of contour-ring intersections. An optimal sequence of movements of the sensor-emitter system has to be found, which leads to a preferably unique object position.
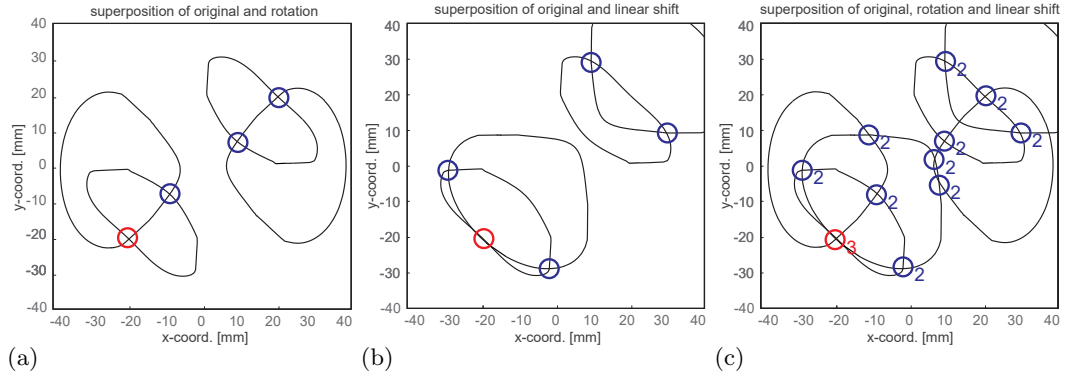
FIGURE 3.3: Mixed information on EEV contour-ring intersections of different movements of the sensor-emitter ensemble. (a) Superposition of perfectly separated contours of original and rotated EEV is repeatedly shown as in figure 3.2(c). Purely rotational movements create symmetric intersection points. Hence, only a significant 2-ambiguous prediction of object localization is possible. (b) Superposition of perfectly separated contour-rings of original and linearly shifted EEV as in figure 3.2(e). In this case the symmetry is broken which results in asymmetric intersection points. (c) Mixed information of different sensor-emitter movements, here the combination of perfectly separated of original, rotated and linearly shifted EEV is illustrated. Since only at one location three contour lines intersect (here marked with a red number three), the possible object position can be reduced to just one location. At the remaining intersections, each marked with a blue number two, only two EEV contour lines intersect. Therefore, these positions can be excluded as possible object positions. The wanted object can be uniquely detected at the reference point $\vec{x} = (\text{-}20, \text{-}20)$ mm.

3.3 Numerical extraction and superposition of EEV contour-rings

In order to assess each possible reference point if a chosen combination of original, rotated and linear shifted EEV leads to a unique identification of that point as the possible object position, the following steps have to be taken. By means of the described FEM-simulation, an EEV matrix consisting of a defined number of discrete points is created. For this, a parametric sweep study with specified resolution of the object positions is performed in COMSOL to achieve the so called original EEV matrix. Both rotational and linear shift operations will be applied to the computed original EEV matrix thus generating EEV matrices for arbitrary rotations and linear shifts without re-simulation. Arbitrary rotations and shifts, however, do not necessarily fit into the chosen resolution of the original grid. Therefore, the described process adds rounding noise to the resultant matrices which, in turn, also creates signal-to-noise problems comparable to measuring the real potential differences for rotated or shifted sensor-emitter setups. For a given EEV matrix (independent of whether it represents an original, rotated or linearly shifted EEV matrix) a discretization operation is introduced to extract contour-rings which have approximately the same potential difference as the reference point. In this process the value one is stored in a newly introduced discretization-matrix **D**, if an entry in

the EEV matrix ($\Delta\varphi_{MP}(x,y)$ = measurement point) is similar enough to the potential of a reference point ($\Delta\varphi_{RP}$ = reference point e.g. measured by the sensor pair). If the similarity is too small, the value zero will be stored in the discretization-matrix. In the ideal case, the numerical extraction process would create thin and closed EEV contour-rings composed of ones within the resulting discretization-matrix **D**.

3.3.1 Extraction of EEV contour-rings by means of discretization strategies

Two different strategies of numerical extraction of EEV contour-rings are implemented which decide, if a potential difference at the measurement point $\Delta\varphi_{MP}$ is similar enough to the potential difference at the reference point $\Delta\varphi_{RP}$. The first discretization strategy is based on a *constant epsilon-neighborhood (CEN)* and the second on a *relative potential distance (RPD)*, which will be described in more detail below.

Strategy 1: Constant epsilon-neighborhood (CEN)

In this strategy, a defined constant epsilon ϵ will be adapted to the range of the values within the EEV matrix. The resulting discretization-matrix $\mathbf{D}_{CEN}$ can be calculated as follows:

$$\mathbf{D}_{CEN}(x,y) = \begin{cases} 1 & \text{if } |\Delta\varphi_{MP}(x,y) - \Delta\varphi_{RP}| < \epsilon \\ 0 & \text{otherwise} \end{cases} \tag{3.1}$$

If the absolute value of the potential difference between an EEV matrix entry $\Delta\varphi_{MP}(x,y)$ and the reference point $\Delta\varphi_{RP}$ lies in a pre-defined ϵ-neighborhood, the corresponding entry in the matrix $\mathbf{D}_{CEN}$ is a one. If this is not the case, the corresponding entry is a zero. Depending on the value of ϵ, this strategy generates further possible object position in addition to the reference point. These positions also represent possible candidates for the wanted object position. By definition, the potential difference at the reference point must be unique, because the matrix will not contain another identical value. The advantage of strategy 1 is that it is easy to implement. Furthermore this strategy is closely related to the concept of measurement accuracy of a real world measurement. Besides, the number of similar object positions within the discretization-matrix is adjustable by the value ϵ. The disadvantage of strategy 1 is that a constant ϵ value considers no different gradients of the potential differences within the EEV matrix. As illustrated in figure 2.8(b), low values of potential difference can result in many possible object

positions (large contour-rings in flat valleys). As described below, this disadvantage will be managed by the second strategy.

Strategy 2: Relative potential distance (RPD)

In contrast to a fixed ϵ value, this strategy is based on a relative potential distance $\Delta\varphi_r$ between measured value and reference value. This is to decide whether an EEV matrix entry (measurement point) is similar enough to the reference point. In this case, the discretization-matrix $\mathbf{D}_{RPD}$ can be calculated as follows:

$$\mathbf{D}_{RPD}(x,y) = \begin{cases} 1 & \text{if } \frac{|\Delta\varphi_{MP}(x,y) - \Delta\varphi_{RP}|}{|\Delta\varphi_{RP}|} < \Delta\varphi_r \\ 0 & \text{otherwise} \end{cases} \tag{3.2}$$

If the relative potential distance $\Delta\varphi_r$ between an EEV matrix entry $\Delta\varphi_{MP}$ and the reference point $\Delta\varphi_{RP}$, which is normalized with respect to the potential difference at the reference point, lies below a threshold $\Delta\varphi_r$, the corresponding entry of the discretization-matrix $\mathbf{D}_{RPD}$ is set to a value of one. Thus, this matrix point represents a possible object position. If this condition is not fulfilled, this entry is assigned a zero. As in strategy 1, the advantage of strategy 2 is that it is also easy to implement. As a result, the EEV contour-rings extracted by strategy 2 have a thinner edge than those obtained by using strategy 1. This difference between the two strategies is depicted in figures 3.4 and 3.6, which will be discussed later.

3.3.2 Superposition of EEV contour-rings based on localization matrices D

In order to determine how many movement conditions are required to uniquely detect an object, the previously introduced two strategies are applied to original, rotated and linearly shifted EEV matrices. The resulting matrices generated by the respective discretization method will be superimposed to determine intersection points.

The general procedure can been structured as follows:

- Simulation of an original EEV which takes environmental parameters of the object, fluid, field, sensor arrangement and number of sensors and emitters into account

- Determination of the potential difference $\Delta\varphi_{RP}$ at one single reference point (object location)

- Applying one of the two strategies CEN or RPD to extract the EEV contour-rings and to discretize the resulting matrix. For this, the potential difference $\Delta\varphi_{RP}$ which was determined for the reference point is used as reference value.

- The original EEV is linearly shifted or rotated, while the object remains at the position of the reference point.

- The extraction and discretization process will be repeated for the shifted or rotated EEV, considering a newly determined potential value $\Delta\varphi_{RP}$ at the reference point. This leads to a different extracted EEV contour-ring.

- Superposition of the numerically separated EEV contour-rings. For this purpose, the discretization-matrices $\mathbf{D}_n$, which correspond to the respective movement conditions n, is added up.

- The number of intersections is determined by counting the number of hits for a certain matrix entry. This predicts the uniqueness of the object positions.

3.3.3 Combination of rotational EEV contour-rings

In this subsection the difference between strategy 1 (CEN) and strategy 2 (RPD) will be discussed. Using strategy 1, figures 3.4(a)-(c) illustrate the numerical extraction and superposition of an original and a rotated EEV matrix, whereas in figures 3.4(d)-(f) the same is shown for strategy 2. In both strategies, the EEV contour-rings are extracted for the determined potential value $\Delta\varphi_{RP}$ at the reference point. Then the results are stored separately in discretization matrices $\mathbf{D}_{i,s}$ with index i being a counter index and index s indicating the strategy. For a single observation at the reference point $\Delta\varphi_{RP}$, each EEV contour is represented by its localization subspace $\mathbf{D}_{i,s}$. Subsequently, the superposition of the extracted EEV contour-rings is realized by adding up N discretization matrices:

$$\mathbf{D}_{\text{res},s} = \sum_{i=1}^{N} \mathbf{D}_{i,s} \quad s \in \{1, 2\} \tag{3.3}$$

For each coordinate of the resulting matrix $\mathbf{D}_{\text{res},s}(x, y)$, its entry contains the number of discretization matrices in which the given coordinate is a candidate for an object position. Intersection points of EEV contour-rings can be detected, if this number is larger than one.
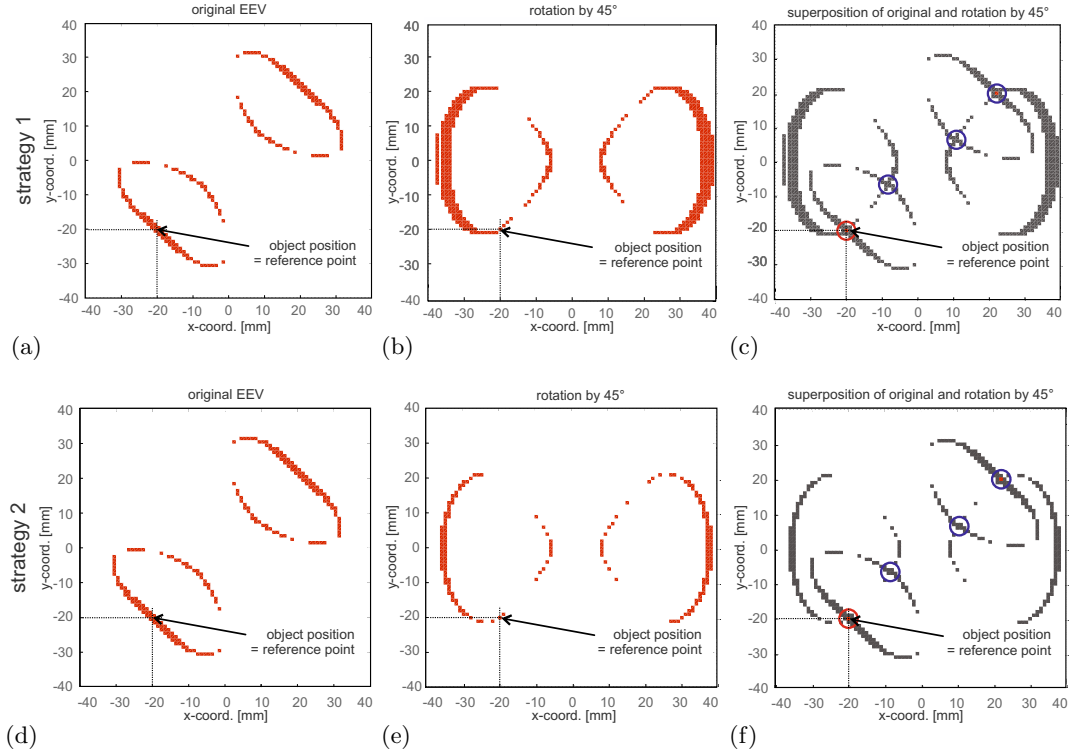
FIGURE 3.4: Two strategies for object localization using extraction, discretization and superposition of rotated EEV contour-rings. At the reference point, a spherical object (indicated by dashed lines) is placed at (-20, -20) mm, which remains at this position. In subfigures (a)-(c) an example for strategy 1 (CEN) is shown. In this case, the potential difference $\Delta\varphi_{RP}$, determined at the reference point, is used to identify those entries within the EEV matrix which contain potential differences that lie in a pre-defined ε-neighborhood of $\Delta\varphi_{RP}$. Those entries represent possible object locations. Strategy 2 (RPD) is depicted in subfigures (d)-(f). Here, the relative potential distance between an EEV matrix entry ($\Delta\varphi_{MP}$) and the reference point ($\Delta\varphi_{RP}$) is normalized with respect to this potential difference at the reference point. If the resulting value lies below a threshold $\Delta\varphi_r$, the entry of the EEV matrix represents a possible object location. (a) Based on strategy 1, an original EEV is used for extraction and discretization of contour-rings. (b) Sensor-emitter ensemble is rotated by 45°. New contour-rings, based on the same strategy as in (a) are extracted and stored in a discretization matrix. (c) The resulting discretization matrices from (a) and (b) are added up (superposed). At the intersection points of all EEV contour-rings, the superimposed matrix contains the value two. At other locations, the values are one or zero. (d) and (e) By using strategy 2, contour-rings for original and a 45° rotated EEV matrix are extracted which results in thinner contour-rings. (f) The discretization matrixes from (d) and (e) are superposed. Again, the maximum value two can be found at the intersection points of the added EEV contour-rings. The uniqueness of the possible object position can be evaluated by the resulting count values in (c) and (f).

The most likely object position $\tilde{\mathbf{p}}_{\mathrm{max},s}$ for the given strategy s can be identified at matrix coordinates of maximum value.

$$\tilde{\mathbf{p}}_{\mathrm{max},s} = \arg\max_{(x,y)} \mathbf{D}_{\mathrm{res},s}(x,y) \qquad (3.4)$$

If several coordinates with the same maximum are present, they will be collected in the set $\mathbf{P}_{\mathrm{max},s}$:

$$\mathbf{P}_{\mathrm{max},s} = \{(x, y, c_{\mathrm{max}}) \mid \mathbf{D}_{\mathrm{res},s}(x, y) = \max \mathbf{D}_{\mathrm{res},s} = c_{\mathrm{max}}\} \tag{3.5}$$

In addition, the set $\mathbf{P}_s$ of all coordinates with at least one intersection of EEV contour-rings ($\mathbf{D}_{\mathrm{res},s}(x, y) > 1$) is given by

$$\mathbf{P}_s = \{(x, y, c) \mid c = \mathbf{D}_{\mathrm{res},s}(x, y) > 1\} \tag{3.6}$$

$\mathbf{P}_{\mathrm{max},s}$ is a subset of $\mathbf{P}_s$ containing possible candidates for an object position. The probability of that coordinate representing an object position increases as the corresponding count value c in an element of $\mathbf{P}_s$ raises. If $c = c_{max} = N$, the corresponding coordinate represents the most probable object position.

In the example shown in figure 3.4, a spherical object is assumed at the reference point (-20/-20) mm, which will be retained for following considerations. Based on strategy 1, the result of the superposition $\mathbf{D}_{\mathrm{res},1} = \mathbf{D}_{1,1} + \mathbf{D}_{2,1}$ of figures 3.4(a) and (b) is depicted in figure 3.4(c). Here, the set $\mathbf{P}_1 = \mathbf{P}_{\mathrm{max},1} = \{(-20, -20, 2), (-8, -8, 2), (8, 8, 2), (20, 20, 2)\}$ contains the real object position and three phantom objects (all $c_i = c_{\mathrm{max}} = 2$). Note, that original and rotated discretization matrices always lead to mirrored intersection points. The reason can be found in the mirror symmetry of the EEV contour-rings. Even if a large number of purely rotational discretization matrices are used, the number of intersection points will be reduced to a minimum of two in best case. Given these conditions, the prediction of an object position can only be 2-ambiguous. However, depending on the thickness of the EEV contour-rings, the set $\mathbf{P}_s$ can also have more than four entries.

Based on strategy 2, figure 3.4(f) contains the superposition $\mathbf{D}_{\mathrm{res},2} = \mathbf{D}_{1,2} + \mathbf{D}_{2,2}$ of figures 3.4(d) and (e). Here, the resulting set $\mathbf{P}_2 = \mathbf{P}_{\mathrm{max},2}$ is in principle the same as for strategy 1. But in figures 3.4(d) and (e) it can be noticed that the extracted EEV contour-rings are thinner. This is an advantage of strategy 2 (RPD) over strategy 1 (CEN).

Because there is always an ambiguity of the object positions when concatenating purely rotated EEVs, it seems advisable to use also discretization matrices of translational or mixed movements to break the mirror symmetry. Section 3.4 will examine this issue.

3.3.4 MUP for combination of rotational EEV contour-rings

In the last section, the idea of concatenated movements of the sensor-emitter array to localize objects is demonstrated. One specific object position is to be uniquely identified by adding up the discretization matrices of the respective movement conditions. In figure 3.4 the concatenation of original and rotated EEV by 45° for only one matrix-point (reference point) is demonstrated. The respective concatenation sequence $S_{c,s}$ can be described by a series of original EEV and rotated (later also translated) versions of the EEV. In this example, the sequence is $S_{R45,s} = [\text{ORIG, ROT45}]$ (where the suffix $R45$ indicates the purely rotational character of this concatenation sequence and the suffix s denotes the discretization strategy). If the concatenation sequence $S_{R45,s}$ is used for this reference point, the position of the object can not be uniquely identified but this given sequence can be tested for each possible object position. Depending on the cardinal number of the set $\mathbf{P}_{\text{max,s}}$ from equation (3.5) it can be decided whether an object position can be uniquely identified by a given concatenation sequence. The resulting matrix for all possible object positions and the respective decisions is called *Matrix of Unique intersection Points* $\mathbf{MUP}_{c,s}$.

$$\mathbf{MUP}_{c,s}(x,y) = |\mathbf{P}_{\text{max,s}}| \tag{3.7}$$

Each point within the MUP indicates, whether the corresponding object position can be uniquely identified. Figure 3.5(a) exemplary illustrates a $\mathbf{MUP}_{R48,1}$ by using strategy 1 (CEN) with an ϵ of $0.5\,\text{mV}$ and the concatenation sequence $S_{R48,1} = [\text{ORIG, ROT48}]$. In this case, the prediction of an object position can only be 2-ambiguous because always a second, point symmetric localization exists. In consideration of this given concatenation sequence, the 2-ambiguous positions are indicated by white pixels. Positions with higher ambiguity are marked as black pixels.

3.3.5 Contrast function of rotational EEV contour-rings

Considering the above assumptions, it is possible to create a $\mathbf{MUP}_{R_\alpha,s}$ for each concatenation sequences $S_{R_\alpha,s} = [\text{ORIG, R}_\alpha]$ with a rotation angle $\alpha \in [0°...90°]$. In each case the $\mathbf{MUP}$ contains the number of object positions which can be identified uniquely (2-ambiguously) by the sequence and strategy underlying that specific $\mathbf{MUP}$. The percentage of unique points within the $\mathbf{MUP}$ can be plotted over the respective rotation angles. This results in a *contrast function CF*.

$$CF_{RT} = f(\alpha), \quad \alpha \in \mathbb{N} \wedge (0° \leq \alpha \leq 90°) \tag{3.8}$$
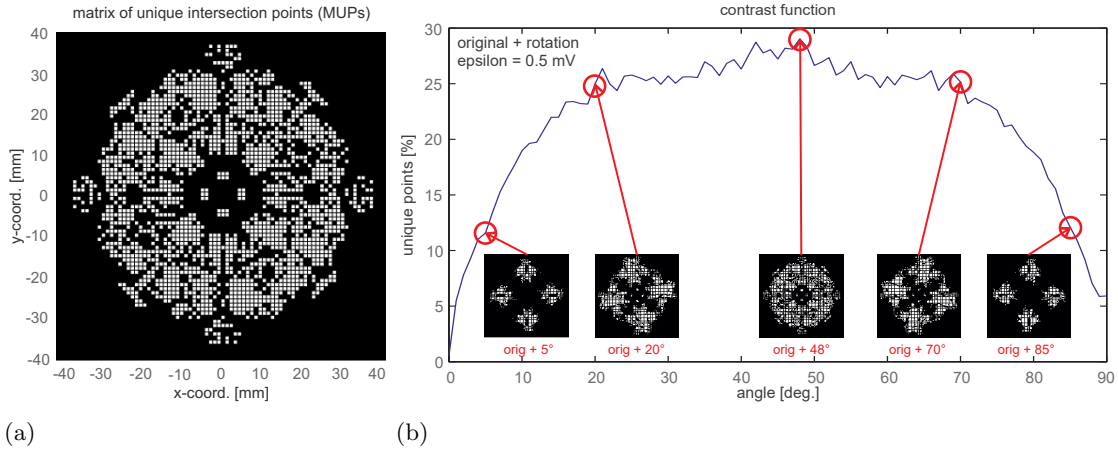
FIGURE 3.5: Matrix of unique intersection points (MUPs) and contrast function of rotational EEV contour-rings used to indicate an optimal movement strategy. The MUP is the basis to find the set of those consecutive movements which allows the unique identification of as many hypothetical object positions as possible. (a) Exemplary visualization of a MUP in which each point (pixel) indicates, whether the corresponding object position can be uniquely identified. Uniquely here means 2-ambiguously, because the concatenation of rotations always creates intersection points which exhibit mirror symmetry. Based on strategy 1 using an ϵ of 0.5 mV for a rotation by 48° ($S_{R48,1}$), the superposition of the discretized EEV contour-rings allows an identification of an object position. Unique positions are indicated by white pixel, which are set to one within the discretization matrix. Positions with higher ambiguity are set to zero, here illustrated as black pixel. As a measure for the quality (uniqueness) of the movement strategy (here for the original and consecutive rotation of the sensor-emitter ensemble) the relative number of white pixels within the MUP is used. (b) Contrast function, for a given concatenation of movement conditions, which illustrates the percentage of unique points within the MUP for combinations of the original EEV and different rotation angles of the sensor-emitter array. In this case, the optimum can be found for the combination of original EEV and an EEV rotated by 48°.

As an example, a contrast function by using strategy 1 with a fixed ε of 0.5 mV is shown in figure 3.5(b). Here, the optimum and thus the highest value of the contrast function, can be identified for a rotation angle of $\alpha = 48°$. It indicates the best movement strategy of the sensor-emitter array when only rotations are allowed. The respective $\mathbf{MUP}_{R48,1}$ is illustrated in figure 3.5(a). In order to derive an optimal movement strategy, the rotation angle that provides the maximum contrast value (here for example $S = [\text{ORIG, R48,...}]$) is used when further movements are subsequently added to the movement strategy. Once this angle is set, it will not be modified, which reduces the number of permutations for a given strategy and the related computational burden.

3.3.6 Combination of linearly shifted EEV contour-rings

In the previous section, the results for the combination of original and rotated EEV contour-rings were analyzed. Figure 3.6 shows an example of a linearly shifted EEV contour-ring which represents an additional possibility in the concatenation of sensor-emitter movements.
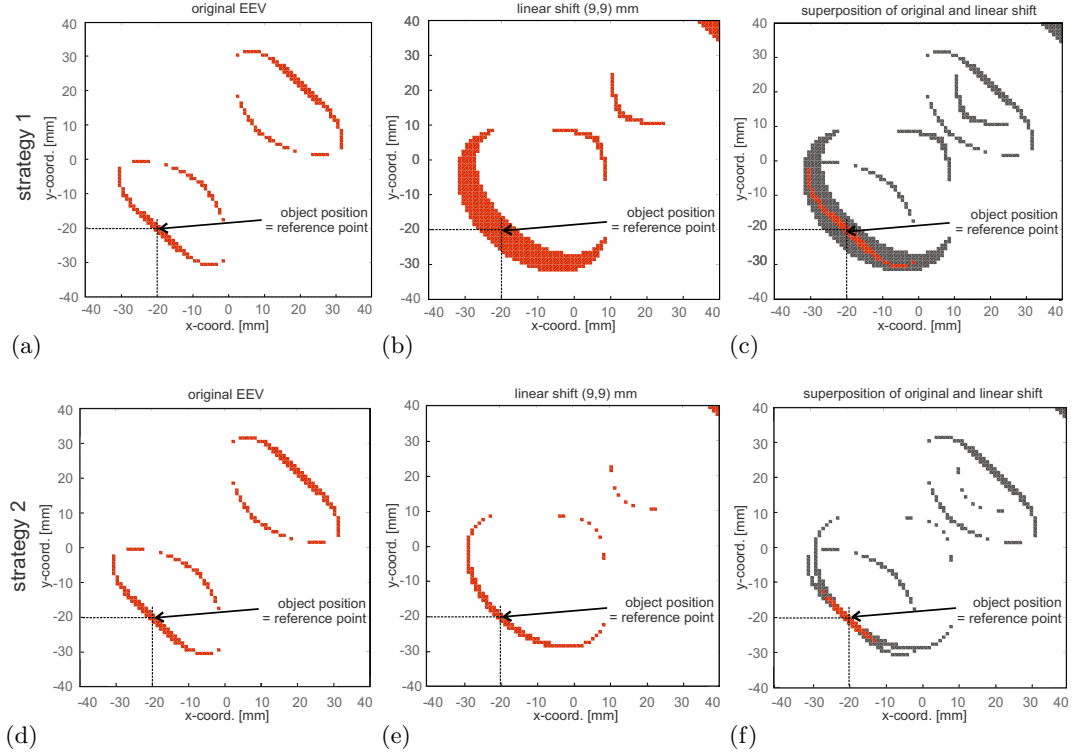
FIGURE 3.6: Two strategies for object localization using numerical extraction, discretization and superposition of linearly shifted EEV contour-rings. As shown in figure 3.4, a spherical object is placed at a fixed reference point (here at (-20, -20) mm). In (a)-(c), strategy 1 (CEN) and in (d)-(f) strategy 2 (RPD) is used for the numerical extraction. (a) Discretization matrix of original EEV matrix. (b) Extracted EEV contour-rings following a shift by 9 mm in x- and y-direction, respectively. (c) Superposition of discretization matrices of (a) and (b). The intersections of the added EEV contour-rings exhibit the maximum values, which in this case is a count value of two (highlighted in red). (d)-(f) Same as in (a)-(c) but strategy 2 is used for discretization. Compared to the results of strategy 1, thinner contour-rings can be observed. The resulting count values in (c) and (f) provide information on the uniqueness of possible object positions.

This example uses identical conditions (material parameters, size of object, position of reference point) as compared to those of the previously presented rotational concatenations. Figures 3.6(a)-(c) visualize the numerical extraction and superposition of an original and a linearly shifted EEV matrix for strategy 1 (CEN). By using strategy 2 (RPD), the same is shown in figures 3.6(d)-(f). In both strategies a linearly shift movement of the sensor-emitter ensemble of 9 mm in x- (horizontal) and 9 mm in y- (vertical) direction is applied. As already described for the rotational case, the EEV contour-rings are

numerically extracted and stored separately in different discretization matrices $\mathbf{D}_{i,s}$. As opposed to the combination of original and rotated EEVs, which at best provide 2-ambiguous object positions, the combination of original and linearly shifted EEVs breaks the symmetry. This potentially results in a unique object position. It should be stressed, that the usage of strategy 2 (RPD) leads to thinner EEV contour-rings as compared to strategy 1 (CEN). Comparing figures 3.6(c) and 3.6(f) shows that thinner EEV contour-rings are to be preferred. After superposition of the extracted contour-rings and counting of the intersection points, the number of possible object positions (red pixels) is smaller for strategy 2. However, both strategies show phantom objects at several positions. That means, that for the given operation the position of the object is still not unique.

3.3.7 MUP for combination of linearly shifted EEV contour-rings

For linearly shifted EEV contour-rings, the matrix of unique intersection points ($\mathbf{MUP}$) can in principle be generated in a similar way as for the case of rotation. Each matrix entry indicates whether the corresponding object position can be uniquely identified by a concatenation sequence $S_{c,s}$ of movements of the sensor-emitter ensemble. In this case, the sequence is composed of an original (ORIG) and a linearly shifted (LS) EEV matrix ($S_{LS,s} = [\text{ORIG}, \text{LS}_{xy}]$). As an example, figure 3.7(a) illustrates the $\mathbf{MUP}_{x9y3,1}$ with a fixed ε of $0.5\,\text{mV}$ for the extracted EEV contour-rings. Compared to purely rotational movements as depicted in figures 3.4 and 3.5, linearly shifted operations of the sensor-emitter array identify truly unique (as opposed to 2-ambiguous) object positions in the $\mathbf{MUP}$.

3.3.8 Contrast function of linearly shifted EEV contour-rings

It is possible to generate one $\mathbf{MUP}_{LS_{xy},s}$ for each linear shift in different x- and y-directions which results in a two dimensional contrast function.

$$CF_{LS} = f(x,y), \quad x,y \in \mathbb{N} \wedge (0 \le x \le x_{\max})$$
$$\wedge (0 \le y \le y_{\max}) \tag{3.9}$$

In the example depicted in figure 3.7(b) strategy 1 was used with an ϵ of $0.5\,\text{mV}$ and x_{max} and y_{max} restricted to $9\,\text{mm}$. The percentage of unique points for a given shift operation is represented on the vertical axis. In this figure, the largest value of the contrast function can be found for a shift of $9\,\text{mm}$ in x- and $3\,\text{mm}$ in y-direction (see

FIGURE 3.7: Matrix of unique intersection points (MUPs) and 2D-contrast function of linearly shifted EEV contour-rings. (a) MUP by using strategy 1 with ϵ of 0.5 mV for the combination of an original and a linearly shifted sensor-emitter array (9 mm in x- and 3 mm in y-direction). (b) In contrast to rotational operations, which result in scalar parameter, the linear shift operation is a two dimensional parameter. This leads to a 2D-contrast function, which visualizes the percentage of unique points in the combination of the original EEV and different linear shifts of the sensor-emitter ensemble.

$\mathbf{MUP}_{LS_{x9y3,1}}$ in figure 3.7(a)), which indicates the locally best movement strategy of the sensor-emitter ensemble.

3.4 Estimation of unique object positions for permutations of rotational and linearly shifted movements

To obtain an efficient measurement strategy for a preferably unique estimation of object positions, this section analyses the results of different movement sequences of the sensor-emitter array. In figure 3.8(a), the results for an increasing number of purely rotational movements of the sensor system, concatenated in a movement sequence, is shown. The results of an increasing number of concatenated linear shifts are demonstrated in figure 3.8(b). Mixed sequences of rotations and linear shifts are finally depicted in figure 3.9. Since strategy 2 (RPD) generally provides better results than strategy 1 (CEN), this strategy was used for all results presented here. The optimum value of uniqueness is determined after each procedural step (rotation in figure 3.8(a) or linear shift in figure 3.8(b)). The best movement operation in each case (e.g. a rotation angle or a linear shift) is stored in the current movement sequence S. Subsequently, the next best movement condition can be looked up in the respective contrast function and will again be added to the exisiting movement sequence S.

(a)

(b)
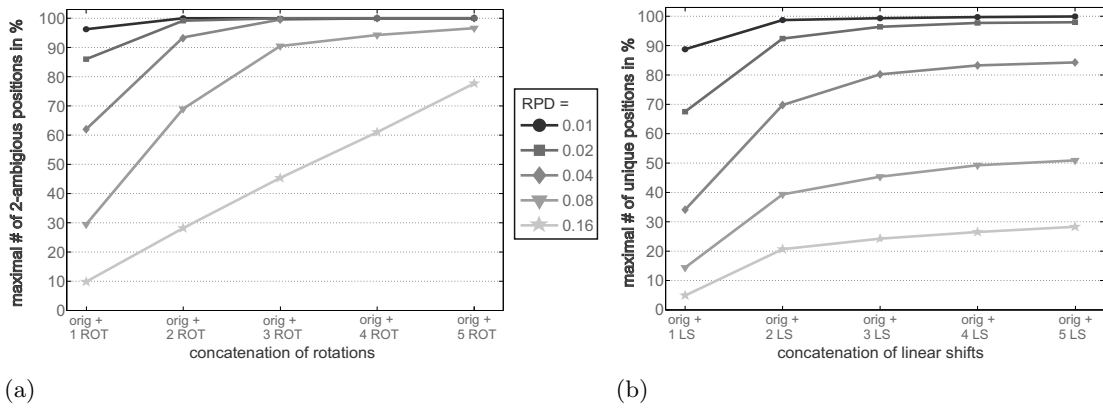
FIGURE 3.8: Comparison of uniqueness in object localization for purely rotational and purely linearly shifted concatenations of movements. (a) Concatenations of original EEV and an increasing number of rotated EEVs. The resulting maximum number of 2-ambigious positions in percent is displayed as a function of different relative potential differences (RPD, see different shades of gray). For concatenations of purely rotational movements, symmetry effects have to be considered. This implies that a maximal uniqueness of 100 % in this case does not represent unique object locations but mirror symmetric locations of objects (2-ambiguous). (b) Concatenations of original EEV and an increasing number of linearly shifted EEVs. In contrast to (a), shift movements lead to unsymmetrical intersection points. Hence, symmetry effects are irrelevant such that truly unique object positions can be identified.

Figure 3.8(a) visualizes the results of the concatenation of an original EEV and an increasing number of purely rotated EEVs in dependence of different RPD-values. If a small value of RPD is defined, which represents a high measuring accuracy, even the concatenation of a small number of rotational movements generates a high percentage of 2-ambigious object positions. With an accuracy of 1 % of relative potential distance with respect to the reference point, a concatenation of original and two rotational EEVs is sufficient to achieve a 100 % accuracy of 2-ambiguous object positions. For large RPD-values, a large number of concatenations or a high measurement accuracy is required. The results of concatenations of an original EEV and an increasing number of purely linear shifted EEVs is shown in figure 3.8(b). In contrast to figure 3.8(a), comparable RPD-values indicate lower results for the maximal number of unique points for the same number of movements (e.g. ORIG + 3 LS vs. ORIG + 3 ROT). The results imply that combinations of rotations and linear shifts form an optimal strategy in which the symmetry is broken and to achieve a high number of uniquely identifiable object positions.

Figure 3.9 illustrates results of uniqueness for mixed movement sequences. Here the maximum number of unique positions is plotted over different RPD-values. The best value of uniqueness is achieved by the concatenation of an original EEV, one linear shift and one rotational movement (ORIG + LS + ROT). Even purely linearly shifted movements (ORIG + LS + LS + LS) do not achieve higher values. The graphs of purely rotational movements are set to zero because they are only 2-ambiguous. For an

RPD-value of 4 %, the concatenation composed of the original EEV, one rotation and one linear shift, enables an over 90 % unique identification of all possible object positions.
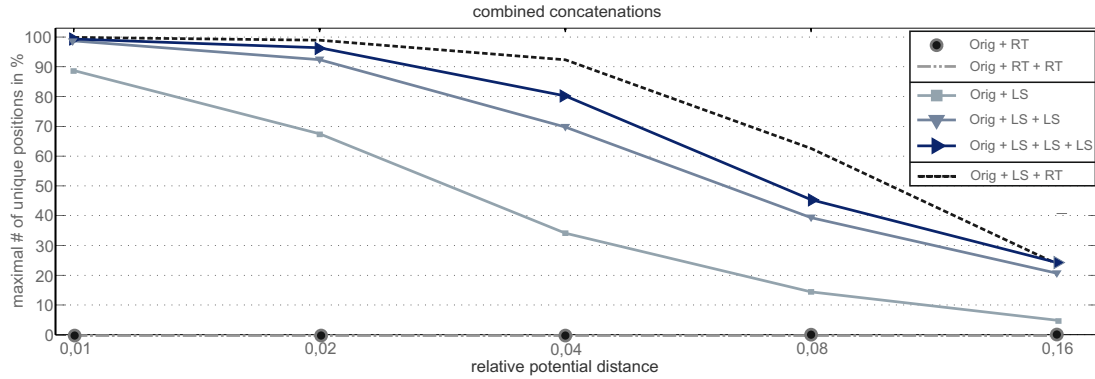
FIGURE 3.9: Visualization of uniqueness for concatenations of mixed sequences of rotations and linear shifts. Note that the movement sequences are not commutative. The combination of an original EEV followed by one rotational and one linearly shift movement (ORIG + LS + ROT) shows the best uniqueness values for a given RPD in comparison to purely linearly shift concatenations as depicted in figure 3.8(b). For purely rotational sequences (ORIG + ROT),(ORIG + ROT + ROT) the values are set to zero, because they are only 2-ambiguous and not unique.

3.5 Summary

As described in detail in the in the introductory chapter 1, weakly electric fish are able to generate and sense electric fields. They use this ability for communication and active electrolocation. Specialized electroreceptors, distributed all over the fish's skin, allow to receive the emitted electric field and its distortions, caused by objects (Nelson and MacIver 1999). In this chapter, the biological model was reduced to a simple emitter and sensor dipole whose axis is arranged orthogonally and symmetrically to each other. This reduced example was used to find an optimal, active movement strategy of the sensor-emitter ensemble that leads to a unique identification of an object position in the nearby environment of the array. This issue has been already pursued based on probabilistic (e.g. Bayes filter, Kalman filter) approaches (Lebastard et al. 2013; Y. Silverman et al. 2012; Y. Silverman et al. 2013). However, before these more complex approaches are adopted, the very basic movement strategy of the sensor-emitter array can first be optimized as such. Thus, the concept of EEVs (Solberg et al. 2008) was revised, which contains the placement of objects at different positions relative to the sensor frame. The object positions and the potential difference measured here are mapped in an array (EEV). When a sufficient number of movements is arranged in a sequence, a clear identification of the object positions is possible. Therefore, the sensor-emitter array has to be moved actively and the respective EEV contour-rings, which are based on the potential measurement at the sensors, have to be superimposed.

In this chapter it was also shown, that the concatenation of purely rotational movements has the disadvantage of mirror symmetries. Mirror symmetries can not be prevented by superposition of contour-rings from rotated EEVs. For this reason, the notion of 2-ambiguous object positions was introduced for concatenations of pure rotations. In contrast, the concatenation of pure linear shifts of the ensemble generates potentially unambiguous results. But the highest percentage of object positions can be uniquely identified by using a concatenation of the original EEV, a linearly shifted and a rotated EEV (ORIG + LS + ROT). Based on the concept of MUPs (matrix of unique intersection points) and respective contrast functions which have been defined in this chapter, an evaluation of the uniqueness was performed.

The scanning strategy introduced in this chapter is based on the ability of a technological measuring system to record the movement of the sensor-emitter system with a certain accuracy in an egocentric reference frame. The biological model solves this problem by receiving and processing of proprioceptive information of active body or body parts movements. An example for an actively moved body part of fish is the Schnauzenorgan (Engelmann et al. 2009) which is covered with hundreds of electroreceptors. By moving the Schnauzenorgan, a fish presumably obtains additional information on its own location and objects in its vicinity.

Furthermore, the movement velocity of the object to be observed must be taken into account for position measurement accuracy. The measurement strategy proposed in this chapter consists of the two sensor movements rotation and linear shift and the corresponding measurements of the potentials at the sensors. The necessary EEV is used like a lookup table and can be calculated beforehand. The movement of the sensor-emitter ensemble could be realized in a technological implementation just by switching from one pair of sensor electrodes to another one in an array of sensors. This further reduces the time required for the measurement process.

In addition, this chapter focuses on the localization of a single object. If for example more than one object is present in a symmetrical configuration with respect to the sensor-emitter array, the sensor reading might cancel out and the system would be blind. In a more general and natural situation, objects successively enter the boundary of the measurement volume of the sensor-emitter array. This problem could be solved, at least in part, by a higher system level that takes object tracking into account.

If the size and shape of objects are also to be determined, an electric imaging system with considerably more than just two sensors would be required. This could be used to receive an electrical projection of the object shape onto a sensory surface. An examplary shape recognition strategy is presented by Ammari et al. (2014). The arrangement with

multiple sensors as described above would therefore be beneficial both for speeding up the measurement and for shape recognition.

In order to avoid computational expensive FEM-simulations for EEVs, the next chapter will focus on a simplified analytical representation for EEV contour-ring calculations. Faster calculations based on algebraic methods also allow the development of strategies for an active design of the emitted field and for optimizing the arrangement of the sensors. The results will finally be implemented in a real physical experiment in order to transfer the active localization strategy shown here e.g. in marine robotics.

4

Search area partitioning and contour-ring fragmentation as a strategy in an application for active electrolocation

Abstract

Chapter 1 explained that weakly electric fish use active electrolocation and scanning behavior to detect objects and additional sensory information of their nearby environment. Inspired by this biological example, this chapter carries the bioinspired approach an important step further by introducing an *application* for active electrolocation based on reduced sensor movement sequences as introduced in chapter 3. The reduced sensor movements are used as a precursor for search area partitioning. In chapter 3 and in Wolf-Homeyer et al. (2016), a minimal set of scanning movements was proposed. Conducted with an initially simulated receptor system consisting of an emitter dipole and an orthogonally arranged pair of sensor electrodes, sensor measurements are used to look up EEV contour-rings (Solberg et al. 2008). The algorithm introduced in the present chapter requires only fragments of discrete EEV contour-rings. It is based on an analytical representation of the electric field and the EEVs rather than using computationally expensive FEM-simulations. A close inspection of the scanning movements allows an exclusion of sectors of the general search area (search area partitioning). Discrete two-dimensional EEV contour-ring points (CRPs) of desired accuracy are extracted. Using a nearness metric, sets generated for each sensor-emitter orientation are analyzed to find subsets containing corresponding points which allow to estimate the object position. The conception of two resulting localization algorithms concludes this chapter.

Most of the scientific results presented in this chapter have been published in:

Wolf-Homeyer et al. (2018)

This manuscript includes Jacob Engelmann and Axel Schneider as co-authors.

4.1 Short range sensor application based on a biomimetic abstraction for active electrolocation

Already at an early stage, realistic FEM-based field models were used to investigate the field generated by fish and distortions caused by objects located within this field. The biological model acted as inspiration to develop different approaches for short range sensors for underwater systems. The sensor system in Boyer et al. (2012) is composed of a mosaic of electrodes intended to measure currents. This includes a complex analytical model for electrolocation of objects and also for the recognition of their different shapes. The robotic electrolocator application developed by Bai et al. (2015) and Fang et al. (2016) contains five or seven pairs of differential electrodes for sensing the perturbation due to objects and for the evaluation of the resultant electric image. In this case, the number of sensors used here compared to the biological model is small. In the following, different approaches for the acquisition and analysis of measured data are identified. The synergy between simulations and physical models have been investigated by Neveln et al. (2013) for the study of bioinspired and biomimetic robotics which is based on electric fish model approaches. For processing and analyzing the data of the electrolocation system, Peng et al. (2017) presents three location algorithms in the frequency domain. In Boyer et al. (2015), robotic systems are proposed which use a reactive control strategy for electric sensing. The sensing system demonstrated in Bai et al. (2016) is based on a capacitive method for object identification. In Lebastard et al. (2013), a model-based approach by using a Kalmann filter is presented to uniquely localize objects. A dipole approximation and a non-iterative multi-frequency location search algorithm is applied in Ammari et al. (2013) which is based on a mathematical model.

In this chapter, the design of the sensor-emitter ensemble was deliberately reduced to a minimum. As in chapter 3, the setup is composed of a simple emitter dipole and an orthogonally arranged pair of sensor electrodes. This reduced system is used to develop an application algorithm for active electrolocation. It contains a compact analytical model of the electric field and the corresponding EEV and introduces two scanning strategies based on a minimal set of scanning movements (Wolf-Homeyer et al. 2016) to transfer it to future robot systems e.g. to AUVs (Autonomous Underwater Vehicles). In a first step, an FEM-simulation used to create a *ground truth* and thus optimal measurement source to be compared with the simplified, analytical calculation of an ensemble of electrosensory viewpoints (EEV) for object localization as introduced in the course of this section. In section 4.4, real test measurements will be introduced for reference.

The biomimetic abstraction as presented in section 2.3 and also used in Wolf-Homeyer et al. (2016) is assumed to identify the position of a nearby object. The reduced sensor-emitter system used here is based on the shape and kind of measurement introduced

in Solberg et al. (2008). It is composed of a simple and orthogonally arranged sensor and emitter dipole. The electrodes are assumed to be fixed on a joint electrode mount, consequently they maintain their relative positions with respect to each other when the mount is moved. Combined with the minimal movement strategy proposed in Wolf-Homeyer et al. (2016), consisting of a combination of the original condition, a rotational movement and a linear shift, a unique identification of an object position is possible. The aim pursued in this chapter is to derive and assess an efficient algorithm, which implements electrolocation based on this minimal movement strategy without the computational costs of an FEM-simulation. A single sensor reading of the potential difference $\Delta\varphi$ at the sensor electrodes can be used to look up EEV contour-rings, but it does not uniquely identify the position of the object. A unique identification can be achieved by shifting or rotating the sensor-emitter array. As a result, the respective EEV is also moved according to the movement condition. If a measurement at the sensors before and after the movement is given, in principle two sets of different contour-rings can be looked up from the EEV. By superposition of these EEV contour-rings, the number of possible object positions is reduced to the intersection points of the rings. In this chapter, this primary movement strategy which performs the superposition of contour-rings to find intersections will be replaced by a simple estimation of nearness.

4.1.1 Analytical calculation of electric field in a 2D-plane and the charge of the dipole to determine the EEV

In a first approach, the EEV matrix was simulated by using FEM. The goal of this section is to calculate EEVs analytically, that means independent of computationally expensive FEM-simulations, which is based on a simplified analytical formulation. In figure 4.1(a) the 2D-abstraction of the sensor-emitter array is presented. As shown in figure 4.1(b), it is assumed that the electric field is caused by two parallel conducting cylinders of infinite length and opposing line charge density λ in a homogeneous medium. Both cylinders exhibit the same size, with radius R and their center points are arranged at a distance of 2d apart.

A constant potential $\pm V_0$ at the emitter electrodes and consequently a constant voltage V between these electrodes is required for the arrangement to be considered and for following calculations. Here, the surfaces of the cylinders represent equipotential surfaces. Thus, the dipole field caused by the two cylinders is equal to a field generated by two charged wires. As a consequence, the line charge densities $\pm\lambda$ of these wires and their distance b to the origin have to be found such that these conditions are satisfied. To find a solution for b, the *method of images* is used which represents a special technique in
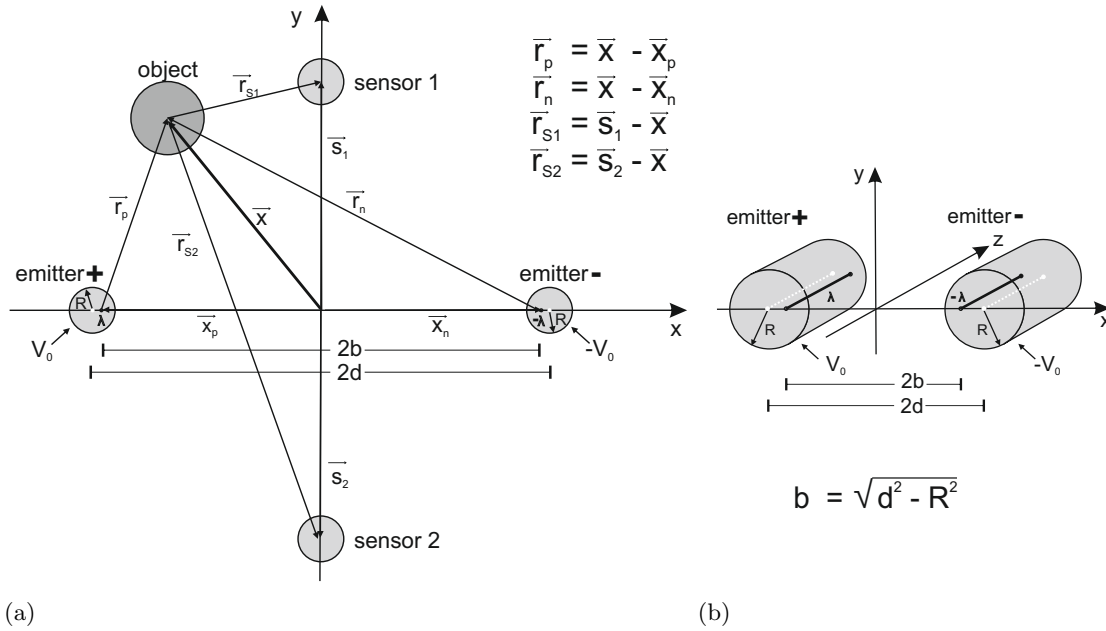
FIGURE 4.1: Sensor-emitter ensemble in vector representation. (a) 2D-abstraction of the sensor-emitter array. On the x-axis, the set of two emitter electrodes are arranged orthogonally to the set of sensor electrodes, which are located on the y-axis. In addition, the arrangement contains a spherical object. With reference to the equations shown in section 4.1.1, the relationships within the configuration are represented by vectors. (b) 3D-abstraction of two parallel conducting cylinders of infinite length which represent the emitter electrodes. All drawings are not to scale.

electrostatics. In case that the potential V corresponds with the surfaces of the emitter electrodes, the distance b can be calculated as:

$$b = \sqrt{d^2 - R^2} \tag{4.1}$$

The derivation of equation (4.1) is based on the analysis of *Apollonian circles* which can be found in Appendix A. The line charges $\pm\lambda$ of the wires are equal to the charges on the surface of the emitters and are located at positions $\vec{x}_p = (-b, 0)$ and $\vec{x}_n = (b, 0)$.

As depicted in detail in figure 4.1(b), the line charges $\pm\lambda$ (and the respective wires) are aligned with respect to the z-axis if cartesian coordinates are assumed. In this case, the electric field can be displayed as a function of the coordinates x and y. The emitter electrodes in this 2D-plane are represented as circles of radius R. A constant charge density can be observed within the cross-sectional area of these electrodes due to the spatial distribution of the charge. The individual electric fields $\vec{E}_p$ and $\vec{E}_n$ at position $\vec{x}$ (point of observation) outside the cylinders can be analytically calculated for the corresponding line charge density:

$$\vec{E}_p(\vec{x}) = \frac{\lambda}{2\pi\epsilon} \cdot \frac{\vec{r}_p}{(r_p)^2} \qquad \vec{r}_p = \vec{x} - \vec{x}_p \qquad (4.2)$$

$$\vec{E}_n(\vec{x}) = \frac{-\lambda}{2\pi\epsilon} \cdot \frac{\vec{r}_n}{(r_n)^2} \qquad \vec{r}_n = \vec{x} - \vec{x}_n \qquad (4.3)$$

where r_p and r_n are the distances between position $\vec{x}$ and the electrically charged conductors. The permittivity ϵ is composed of the vacuum permittivity ϵ_0 and the relative permittivity ϵ_r of the medium as shown in equation (2.8).

The total electric field at the point of observation can be calculated by superposition of the contributions of two opposing line charges and the corresponding individual electric fields $\vec{E}_p$ and $\vec{E}_n$:

$$\vec{E}(\vec{x}) = \vec{E}_p(\vec{x}) + \vec{E}_n(\vec{x}) \qquad (4.4)$$

$$\vec{E}(\vec{x}) = \frac{1}{2\pi\epsilon} \cdot \left(\frac{\lambda(\vec{x} - \vec{x}_p)}{\|x - x_p\|^2} - \frac{\lambda(\vec{x} - \vec{x}_n)}{\|x - x_n\|^2} \right) \qquad (4.5)$$

The line charge density λ which is shown in equation (4.5) has to be determined in consideration of the applied constant voltage V between the emitter electrodes. The relationship between the scalar potential φ and the electric field vector $\vec{E}$ over the surface of a conductor is generally defined as:

$$\varphi = - \int \vec{E} d\vec{s} \qquad (4.6)$$

Applying this to equation (4.5) for the dipole field consisting of two opposite line charges leads to the formulation of equation (4.7), which defines the potential distribution on the 2D-plane.

$$\varphi(\vec{x}) = \frac{\lambda}{2\pi\epsilon} \cdot ln\left(\frac{r_n}{r_p} \right) \qquad (4.7)$$

A constant potential $\pm V_0$ at the emitter electrodes is assumed. Here, the positive line charge can be found at $(-b, 0)$ and the negative at $(b, 0)$. Thus, the voltage V between the charges can be calculated from:

$$V = V_0(\vec{x}_p) - (-V_0(\vec{x}_n)) = \frac{\lambda}{4\pi\epsilon} ln\left(\frac{\sqrt{(x-b)^2 + y^2}}{\sqrt{(x+b)^2 + y^2}}\right) \tag{4.8}$$

By converting and simplifying equation (4.8), the respective line charge density at one emitter electrode with fixed potential V_0 can be determined (Landau et al. 1984):

$$\lambda = \frac{V_0 \cdot 2\pi\epsilon}{ln(\frac{d}{R} + \sqrt{(\frac{d}{R})^2 - 1})} = \frac{V_0 \cdot 2\pi\epsilon}{cosh^{-1}(\frac{d}{R})} \tag{4.9}$$

For all following steps, the line charge λ, as calculated in equation (4.9), remains constant and will be inserted in equation (4.5).

The EEV, as already mentioned in section 2.3, describes the perturbation $\delta\varphi$ of a spherical object of radius a in the uniform electric field E_0 for a point $\vec{r}$ outside the sphere. To create such an EEV, the analytical description derived in equation (2.60) can be used. Adapted initially from Rasnow (1996), Solberg and co-workers (Solberg et al. 2008) as well as Boyer et al. (2012); Bai et al. (2015); Fang et al. (2016); Neveln et al. (2013) and, Lebastard et al. (2013) utilise a reduced form of this algebraic description.

Contrary to the calculation of the electric field described above, now the coordinate origin is assumed to be in the center of the spherical object. Based on the 2D-solution of Laplace's equation (Landau et al. 1984), the perturbations $\delta\varphi_{S1}$ at sensor S_1 and $\delta\varphi_{S2}$ at sensor S_2 of the electric field due to the sphere at point $\vec{r}_{S1}$ and point $\vec{r}_{S2}$ in the 2D-plane can be calculated as:

$$\delta\varphi_{S1}(\vec{r}_{S1}) = \frac{\vec{E}(\vec{x}) \cdot \vec{r}_{S1} \cdot a^2}{r_{S1}^2} \cdot \chi \qquad \vec{r}_{S1} = \vec{s}_1 - \vec{x} \tag{4.10}$$

$$\delta\varphi_{S2}(\vec{r}_{S2}) = \frac{\vec{E}(\vec{x}) \cdot \vec{r}_{S2} \cdot a^2}{r_{S2}^2} \cdot \chi \qquad \vec{r}_{S2} = \vec{s}_2 - \vec{x} \tag{4.11}$$

where r_{S1} and r_{S2} are the distances between the point of observation x and the respective sensor electrodes. Here, the electric field $\vec{E}(\vec{x})$ is based on equation (4.5). The real part of the electrical contrast factor χ as introduced in equation (2.50) provides information on whether the object is perfectly conducting (real(χ)=1), a perfect insulator (real(χ)=-0.5) or if the spherical object has the same resistivity ρ and dielectric constant ϵ as the surrounding medium (real(χ)=0). The potential difference $\delta\varphi$ between the sensor electrodes S_1 and S_2 can be determined by

$$\delta\varphi(\vec{x}) = \delta\varphi_{S1}(\vec{r}_{S1}) - \delta\varphi_{S2}(\vec{r}_{S2}) \tag{4.12}$$

$$\delta\varphi(\vec{x}) = \left(\frac{\vec{E}(\vec{x}) \cdot (\vec{s}_1 - \vec{x}) \cdot a^2}{\|\vec{s}_1 - \vec{x}\|^2} - \frac{\vec{E}(\vec{x}) \cdot (\vec{s}_2 - \vec{x}) \cdot a^2}{\|\vec{s}_2 - \vec{x}\|^2} \right) \cdot \chi \tag{4.13}$$

where $\delta\varphi(\vec{x})$ is an implicit function which represents the numerical discription of an EEV. In the following, equation (4.13) is referred to as *simplified analytical EEV representation*. In this chapter, the approach to analytically calculate the EEV distribution will replace the numerical simulations performed by FEM as presented in Wolf-Homeyer et al. (2016).

To determine the accuracy of the analytical EEV description from equation (4.13) as compared to the numerical (FEM-based) representation, the same fixed set of parameters as in Wolf-Homeyer et al. (2016) is used. Especially, the deviation between the solutions of the simplified analytical EEV representation and the FEM-simulation has to be estimated and analyzed to consider them during further development of an application for active electrolocation.

Figure 4.2 illustrates a comparison of FEM-simulated (a) and simplified analytical EEV representation (b). In this example, EEV contour-rings caused by a spherical object at a fixed position are shown. The comparison of the electric field components along cut line 1 (figure 4.2(c) and (d) shows a close match of the curves. This indicates that the applied electric field of the dipole and the corresponding calculation of the line charge density is similar in both cases. Also the comparison along cut line 1 and 2 of the simplified analytical EEV representation (cmp. equation (4.13)) and the FEM-simulated EEV in figure 4.2(e) and (f) shows a close match with decreasing precision in the vicinity of the electrode sides. Additionally, a cut through the measured EEV is demonstrated. The measuring system and experimental conditions will be described in detail in chapter 4.4.1. The difference between the analytical and FEM-simulated EEV will be tolerated in the development of the application.

4.2 Localization algorithm based on a basic movement sequence

Weakly electric fish show an increased movement activity close to interesting objects. The correspoding movement behavior consists of linear shifted and rotational movements, which seem to be crucial for the fish to collect information on an object (Hofmann et al. 2014). Based on the preliminary work (Wolf-Homeyer et al. 2016) an algorithm
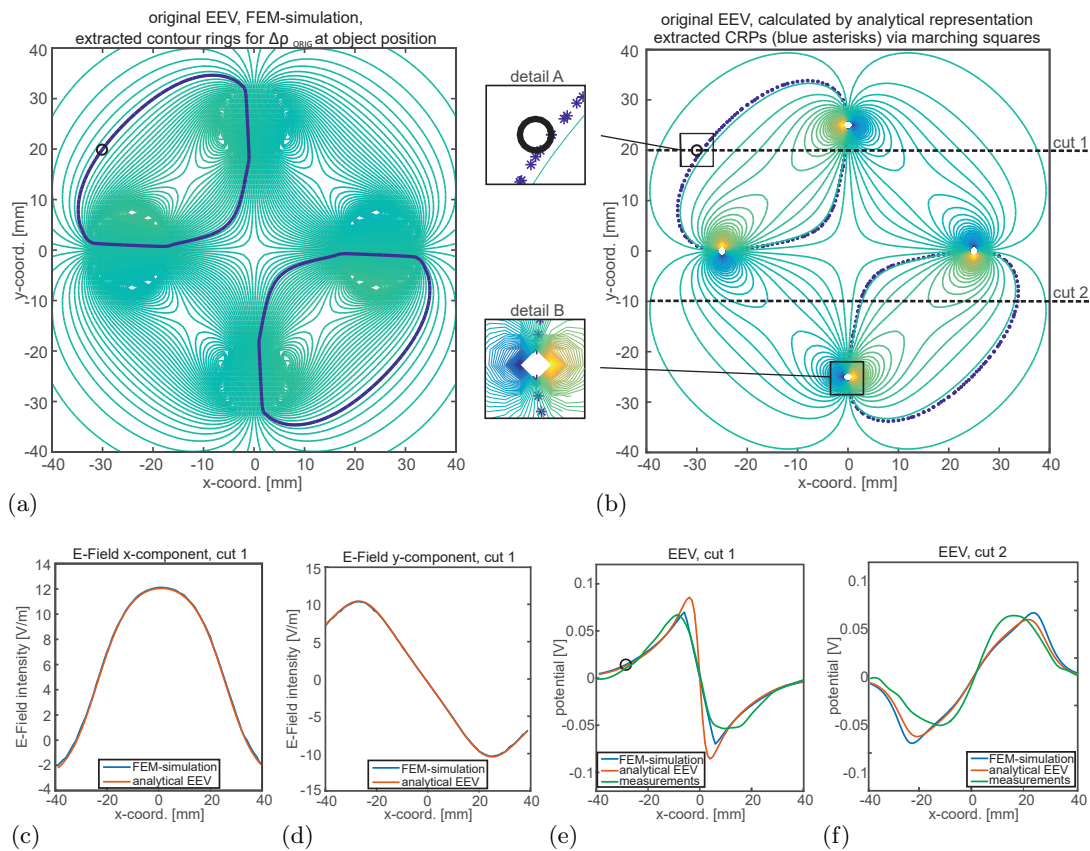
FIGURE 4.2: Comparison of FEM-simulated and analytical EEV representations. (a) FEM-based EEV of a conducting object of radius 7 mm located at position (-30, 20) mm. The object causes the potential difference $\Delta\varphi_{\mathrm{ORIG}}$ between the sensors. This potential difference can also be measured for object positions located along the blue EEV contour-rings. (b) Analytical EEV with identical conditions. The potential difference $\Delta\varphi_{\mathrm{ORIG}}$ which is determined in (a) is used to extract EEV contour-ring points (CRPs) by means of the marching squares algorithm (Schroeder et al. 2006). In detail A, the deviation between the FEM-simulation (green contour line), the analytically calculated CRPs (blue asterisks) and the real object position (black circle) is illustrated. Detail B depicts a singularity point at the position of sensor S_2, which can also be found at all electrode positions. The two horizontal cuts (dotted lines) visualize, where the data for panels (c)-(f) were obtained: (c) x-component of the electric field based on FEM-simulation (blue) and on the analytical solution (red) along cut line 1; (d) y-component of the electric field with same conditions as in (c). The overlay of the results demonstrates a close match for both cases. (e) Comparison of FEM-simulated, analytically calculated and real measured EEV along cut line 1. The results include the marked object. (f) Same as in (e) but for cut line 2. It should be noted that the analytical, the FEM-based and the measured EEV are again in general agreement. The largest deviations can be observed close to the electrode locations.

is developed which combines a minimal set of scanning movements, with intermediate sensor measurements for object localization. Hereafter, the minimal set of scanning movements, composed of linear and rotational movements of the sensor-emitter ensemble (shown in figure 2.7(a)) , will be referred to as *basic movement sequence*.

4.2.1 Active electrolocation by means of a basic algorithm

In figure 4.3, a flow chart of a localization algorithm for calculating an object position is presented. It is based on the basic movement sequence which contains reduced sensor movements as determined in Wolf-Homeyer et al. (2016) and in chapter 3. The combination of a linear shift, a rotation and the original EEV has proven to be an optimal movement sequence. Furthermore, it is described in Hofmann et al. (2014) and Lebastard et al. (2016) that fish alternately exhibit sequences of linear and curve swimming behavior when scanning interesting objects in their environment. This can be considered to be a precursor for search area partitioning, which will be introduced in section 4.2.3. In parallel with the four main steps of the algorithm shown in figure 4.3, this, this method of search area partitioning is also implemented. Search area partitioning is also dependent on the measured potential difference and the respective movement condition of the sensor-emitter array. The first step contains the acquisition of readings from the sensor electrodes for the reduced sequence of movements of the sensor-emitter array. It consists of the three measurements of potentials ($\Delta\varphi_{ORIG}, \Delta\varphi_{ROT45}, \Delta\varphi_{LS}$) which result from a 45° rotation (ROT45) and a linear shift (LS) of the sensor-emitter setup. For real measurements, as explained in the example in section 4.4, the sensor-emitter array is attached to a real robot arm. The arm actively executes the required movements (rotation and linear shift) of the sensor and emitter electrodes, which maintain a constant relative position with respect to each other. Subsequently, it is also possible to construct an array containing electrodes at the original, rotated and displaced positions. For the particular measurement, the electrodes corresponding to the respective rotated or shifted positions would then have to be activated.

The second step of the algorithm from figure 4.3 deals with the definition of source field parameters and calculates the EEV based on the simplified analytical representation as described in section 4.1.1. This step requires the specification of the dipole charge and the material properties (contrast factor, see equation (2.50)). Based on the three measurements performed in step one, the EEV contour-ring points (CRPs) are extracted in step three. According to the respective movement sequence, the orientation and position of the contour-rings have to be modified. This method will be explained in detail in sections 4.2.2 and 4.2.3. The final step (section 4.2.4) includes a nearness metric to identify the object candidates.
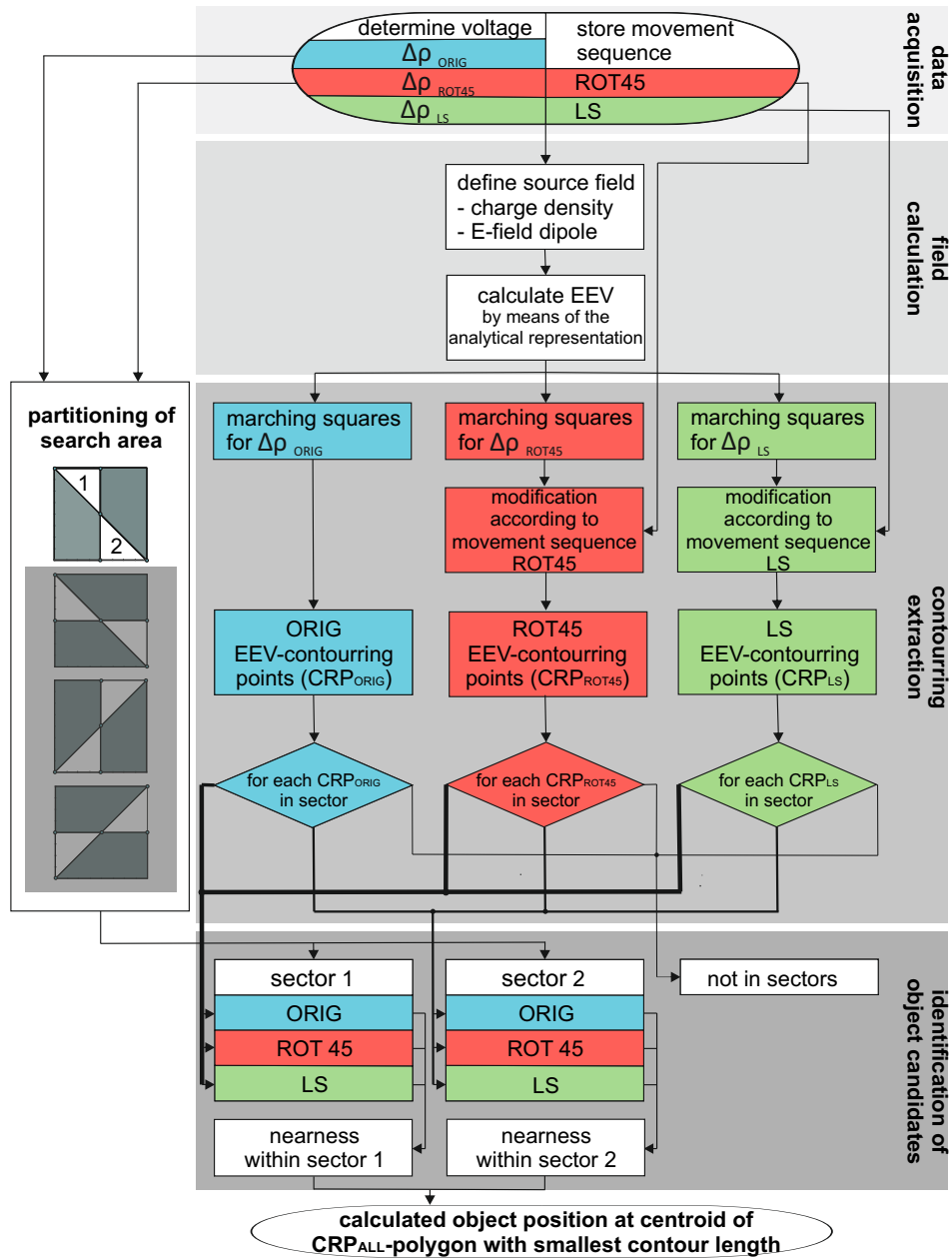
FIGURE 4.3: Basic movement sequence for active electrolocation illustrated in a flow chart. The sequence can be devided into four steps from top to bottom: The first step contains the data acquisition of sensor readings for a sequence of movements of the sensor-emitter array. In the second step, the source field parameters are defined and the basic EEV for the original position is calculated based on the simplified analytical representation. Third, EEV contour-ring points (CRPs) which fit to the measured potential difference $\Delta\varphi$ are extracted. Depending on the underlying movement sequence, the detected CRPs are then either used directly, or rotated or shifted. As illustrated in the parallel box on the left, the search area can be reduced to triangular sectors. The detected CRPs of the third step then can be assigned to the associated sectors. The fourth step is concerned with the identification of object candidates. Intersections of EEV contour-ring fragments of different orientations and shifts within the search sectors are candidates for the true object positions. Instead of intersection, in this sequence the nearness, that means the shortest distance of fragments, is calculated. The centroid of the CRP_{ALL}-polygon with smallest contour-length represents the calculated object position

4.2.2 Extraction of EEV CRPs and modification according to the respective movement sequence

A discrete EEV matrix of object positions with defined resolution can be generated by using the simplified analytical EEV representation according to equations (4.13) and (4.5) as presented in section 4.1.1. If an object is placed within the dipole field, a potential difference $\Delta\varphi$ between the sensor pair can be determined. Within the previously generated EEV matrix, all possible positions which correspond to this measured potential difference have to be extracted. The extraction is based on a marching squares algorithm (Schroeder et al. 2006) which tracks the course of the respective EEV contour-ring. While following a defined threshold isovalue line, this algorithm is used to extract contours in a 2D-matrix. This results in the extraction of discrete 2D EEV contour-ring points (CRPs) as illustrated in figure 4.2(b). Detail A depicts the extracted CRPs as blue asterisks with a slight deviation to the real object position. To begin with, this operation will always be performed by using the original, analytically calculated EEV matrix. In consideration of the identified potential differences $\Delta\varphi_{ORIG}$, $\Delta\varphi_{ROT45}$ and $\Delta\varphi_{LS}$ it is initially independent of the respective movement condition. In a subsequent step, a transformation (rotation or shift operation) according to the movement condition will be applied to the EEV matrix.

The marching squares algorithm determines whether an entry (pixel) of the matrix is larger than or equal to a defined threshold value. In this case, the potential difference $\Delta\varphi$ represents the threshold. In a 2D contour-plot, this algorithm computes the isoline, which follows the isovalue in this given contour sequence. The general procedure of the marching squares algorithm is based on a linear interpolation along edges and corners which is a modification of the marching cubes algorithm, published by Lorensen and Cline (1987) to extract a polygonal mesh of an isosurface from a 3D scalar field. The advantage here is that the algorithm generates CRPs in sorted order with desired accuracy. Afterwards, these CRPs can be transformed by using a suitable rotation or linear shift operator according to the respective movement condition. The rotation operator transforms the extracted CRPs anticlockwise around the origin (0,0) and maps the points onto a new rotated position. By using the shift operator, the points are linearly shifted in the selected x- and y-directions. Original EEV CRPs do not require any transformation. For each movement condition, the resulting CRPs are stored in separate lists.

4.2.3 Search area partitioning

The combination of an original EEV and an EEV rotated by 45° allows the exclusion of polygonal sectors of the search area. As will be shown, the search area can be reduced to

a quarter of the original area. This also leads to a fragmentation of the contour-rings and thus also of the extracted CRPs, which minimizes the number of ambiguous object positions. In Boyer et al. (2013); Lanneau et al. (2017) and Bazeille et al. (2018) a similar method for partitioning, but these cases in consideration of the sign of currents, measured here, is demonstrated. The strategy introduced here is used as a precursor step which reduces the complexity of the actual process of active electrolocation. To determine the polygonal sectors which can be excluded from the search area, the actual movement and the respective sign of the measured potential difference between the sensor electrodes have to be considered. In figure 4.4, four possible cases are illustrated: Figures 4.4(a)-(c) for case 1, (d)-(f) for case 2, (g)-(i) for case 3 and (j)-(l) for case 4. Each of the four cases represents one distinct combination of the signs of the potential differences $\Delta\varphi_{ORIG}$ and $\Delta\varphi_{ROT45}$. The association to one of these four cases always creates two triangular sectors, composed of different basic points for each case. In figure 4.5 an example of the partitioning procedure is demonstrated. The example contains positive values for the two potential differences which means that it is covered by case 1. This leads to a fragmentation of the selected EEV contour-rings as depicted in figure 4.5(d). However, the contour-rings are extracted as a set of CRPs, so it is required to examine whether each individual CRP is located within one of these two sectors. If so, the CRP is assigned to the respective sector and movement condition. If not, the CRP will not be considered during further processing because it represents not an object candidate.

4.2.4   Active electrolocation strategy based on a nearness metric

As derived in Wolf-Homeyer et al. (2016), the position of an object can, in principle, be determined at the intersections of the extracted EEV contour-rings of the original (ORIG), the rotated (ROT45) and linearly shifted (LS) movement condition of the sensor-emitter ensemble. These EEV contour-rings for the respective movement condition are shown in figures 4.6(a)-(c). The EEVs are generated by means of FEM. In addition, this movement sequence was determined in Wolf-Homeyer et al. (2016) as being the optimal movement strategy. The movement conditions ORIG and ROT45 are not sufficient to uniquely locate an object, because a symmetry of the contour-ring intersections are always present in this combination. That means that in the worst case, four intersection points can be identified for each pair of EEV contour-rings. This issue can be counteracted by including the linear shift condition (LS). As a result, a reduction to just one solution is possible. By using the marching squares algorithm, contour-ring intersections might be blurred, caused by inaccuracies and spatial discretization effects. Hence, the identification of precise intersections is replaced by the determination of spatial distances between CRPs of different EEV fragments. Here, this modified strategy is referred to as *nearness metric*.
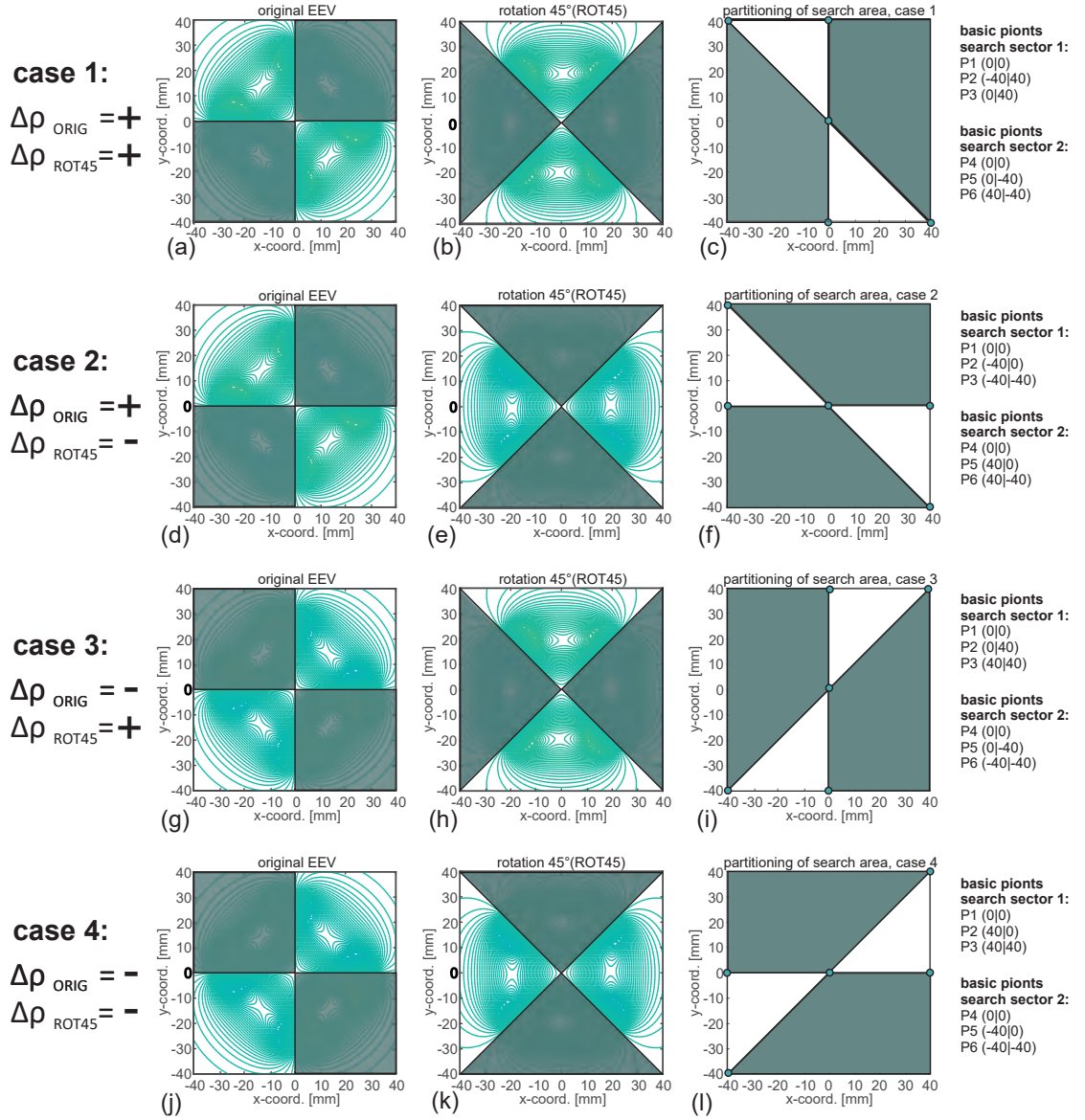
FIGURE 4.4: Partitioning and reduction of search area as a precursor for active electrolocation. It is based on case discrimination of a fixed set of movements (ORIG and ROT45) of the sensor-emitter array and the sign of the measured potential difference. Four possible cases can be identified according to the permutations of the potential differences. Consequently, the association to one of the four cases reduces the search area to a quarter of the original area. (a)-(l) The minimal and fixed set of sensor movements allows the exclusion of sectors of the search area. This leads to a fragmentation of a subset of EEV CRPs. In consideration of the sign of the potential differences $\Delta\varphi_{\mathrm{ORIG}}$ ((a), (d), (g), (j)) and $\Delta\varphi_{\mathrm{ROT45}}$ ((b), (e), (h), (k)) determined at the sensors for the respective movement condition, the search area can be reduced to a combination of two triangular sectors ((c), (f), (i), (l)).

This means that all CRPs of EEV fragments which belong to one type of sensor-emitter array orientation and position are tested with respect to their distances to all other CRPs of the remaining EEV fragments of different orientation and position.

As illustrated in figure 4.6(d), CRPs for each movement condition in consideration of the
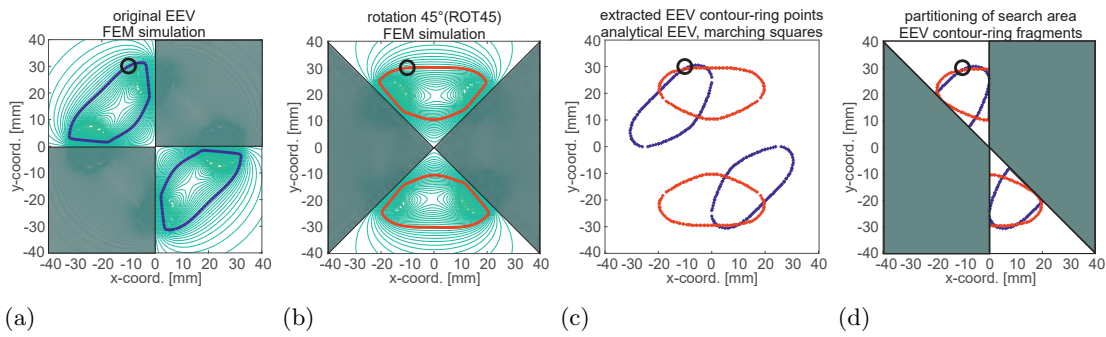
FIGURE 4.5: Example to illustrate the procedure of partitioning. (a)-(d) An object at position (-10, 30) mm is related to two EEV contour-rings for each movement condition. In this case $\Delta\varphi_{\text{ORIG}}$ and $\Delta\varphi_{\text{ROT45}}$ are both positive. This leads to a selection of the partitioning of the search area as depicted in case 1 (see figure 4.4 (a)-(c))

respective potential difference $\Delta\varphi$ between the sensors are extracted. This is based on the analytical formulation, the marching squares algorithm and subsequent modification according to the respective movement operation (ROT45 or LS). In figure 4.6(e), contour-ring fragments composed of those CRPs are shown which remain after using the method of search area partitioning. An close-up view is depicted in detail A in figure 4.6(f). Subsequently, the nearness of the remaining CRPs has to be investigated within the reduced search area to estimate the position of the object. Thus, one contour-ring fragment in figure 4.6(e) results from the original position of the sensor-emitter array (ORIG, blue), one fragment results from the 45° rotation (ROT45, red), and one fragment is due to the linear shift (LS, green). Consequently, out of these three fragments, three CRPs have to be found which show the closest distance to each other as demonstrated in the detail A in figure 4.6(f). As a result, a triangle (black) is composed of the three CRPs. Instead of e.g. the surface area, the contour-length of the triangle is chosen as a metric for the nearness of these three CRPs. The reason for this choice is that if the three points are located far away from each other, but reside almost on one line, the triangle would exhibit a small surface area. Consequently, a high nearness would erroneously be indicated. To detect the triangle with the smallest nearness within the search area, a permutation of all CRPs of the different contour-ring fragments is stored in a matrix. This method is performed separately for the CRPs within search sectors 1 and 2 (upper and lower triangle). The best result is the triplet with the smallest contour-length. The calculated object position is located at the centroid of the identified triangle CRP_{ALL} with the smallest contour-length. If the special case occurs that the triangle collapses to a line, the centroid will also be located on the line. The nearness metric can also be maintained if a movement strategy is chosen which contains n instead of three positions/orientations of the sensor-emitter ensemble. In this case, the triangle changes into a polygon with n vertices.
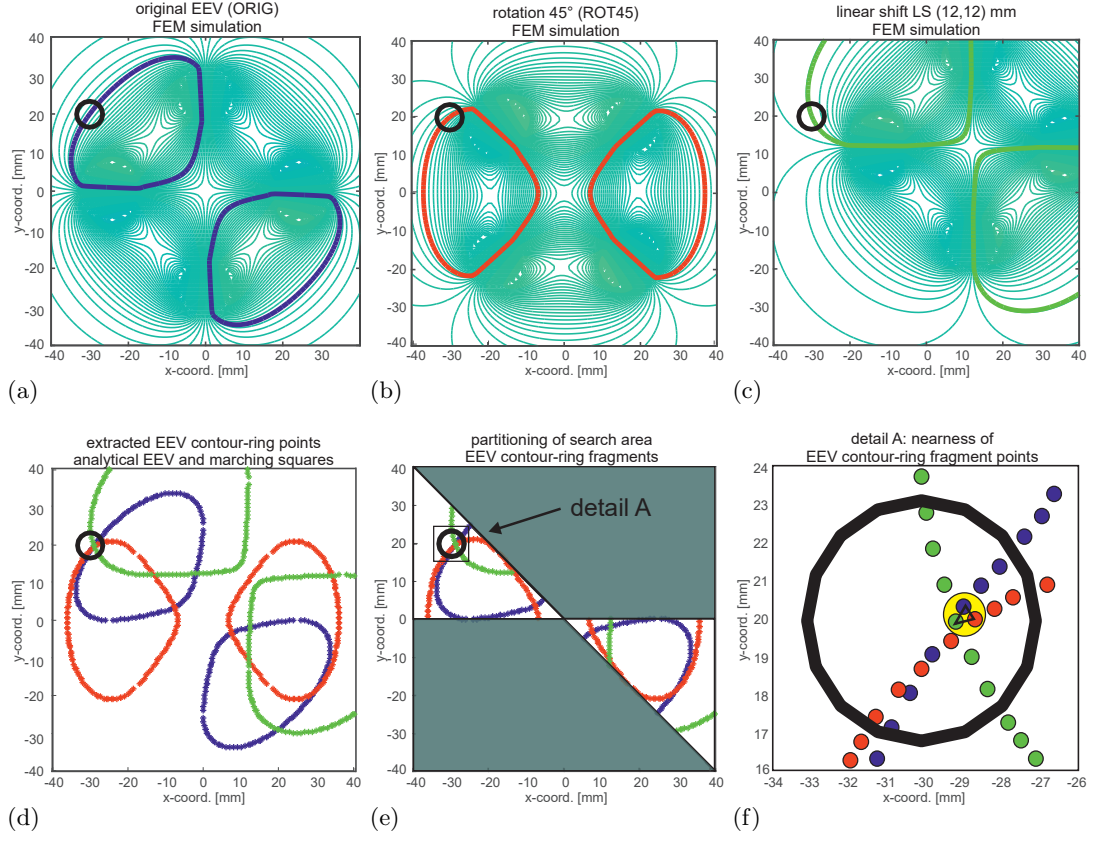
FIGURE 4.6: Modified strategy for active electrolocation based on the EEV intersection method developed in Wolf-Homeyer et al. (2016). In contrast to the intersection method, here the nearness of EEV CRPs is investigated. The CRPs are extracted by a marching squares algorithm (Schroeder et al. 2006). (a) Original EEV contour-rings (ORIG) for an object at position $(-30, 20)$ mm, generated by an FEM-simulation. The potential difference $\Delta\varphi_{\mathrm{ORIG}}$ can also be found along the blue EEV contour-rings. As a consequence, the object position is not unique. (b) The object remains fixed while the sensor-emitter ensemble is rotated by $45°$. It follows that the simulated EEV (ROT45) is also rotated. Consequently, a new potential difference $\Delta\varphi_{\mathrm{ROT45}}$ can be measured at the sensors. This leads to the corresponding extracted EEV contour-rings highlighted in red. (c) Same EEV as in (a) and (b) but for a linear shift of the sensor-emitter array by 12 mm in the x- and y-directions (LS $(12, 12)$ mm). Again, the object remains fixed. The new potential difference $\Delta\varphi_{\mathrm{LS}}$ can be identified along the green EEV contour-rings. (d) In consideration of $\Delta\varphi_{\mathrm{ORIG}}$, $\Delta\varphi_{\mathrm{ROT45}}$ and $\Delta\varphi_{\mathrm{LS}}$, EEV CRPs are extracted. The extraction is based on a marching squares algorithm. Depending on the corresponding movement sequence, the points will be moved accordingly. (e) Method of reduction of the search area for possible object positions. A partitioning of EEV CRP fragments is performed. (f) Detail A with regard to (e). The nearness of the remaining points of the EEV fragments is analyzed to calculate the object position within the reduced search area (see figure 4.4). A triangle composed of one point for each individual movement condition has to be created for all permutations. The calculated object position is identified at the centroid of the CRP_{ALL}-polygon (highlighted in yellow) with the smallest contour-length. In this example, the intersection area (yellow circle) differs from the real center of the object (center of the black circle). On the one hand, it is caused by a low resolution of the marching squares algorithm and, on the other hand, the general differences between the simulated EEV and the analytically calculated EEV as shown in figures 4.2(e) and 4.2(f).

4.2.5 Results by using the basic movement sequence

The basic movement sequence for electrolocation was introduced in section 4.2.1. Additionally, detailed aspects such as CRP extraction (section 4.2.2), search area partitioning (section 4.2.3) and the nearness metric for the actual identification of possible object positions (section 4.2.4) were introduced. They represent central aspects of the algorithmic core of the localization process. The implementation of the simplified, analytical representation for calculating the electric field and the respective EEV, as shown in section 4.1.1, represents another significant aspect for the intended application for active electrolocation. The lowered computational burden by using analytical solutions for object localization is a basic requirement if the entire process is to be performed on a small-scale processor system, e.g. in mobile robotic applications. In this section, the differences between the analytically calculated object positions $\vec{x}_{CAL}$ by means of the above basic movement sequence are compared to the real object position $\vec{x}_{OBJ}$. At first, instead of a physical measurement of the potential differences $\Delta\varphi$ for each object position $\vec{x}_{OBJ}$ with a real sensor-emitter ensemble, the actual potential difference is taken from a high-precision FEM-based COMSOL field simulation, in the sense of an optimal reference. The results are fed into the algorithm proposed in this chapter. The reason for this is that the accuracy of the algorithm can be assessed independently of errors caused by a physical measurement process. The calculated object position $\vec{x}_{CAL}$ is the output of the algorithm.

In figure 4.7 an example to determine the uniqueness of all object positions within the search area is presented. Figure 4.7(a) shows the matrix of Euclidean distance (MOED) which visualizes the Euclidean distance between real ($\vec{x}_{OBJ}$) and those positions identified by using the basic movement sequence. In order to determine whether an object position was calculated with sufficient accuracy, a threshold value has to be introduced. For each possible object position, the result is entered into a binary matrix $\mathbf{D}$ in which the value 0 is stored if the normalized distance lies below the threshold. Here, the distance is normalized with respect to the diagonal distance of the search area. The diagonal distance of the search area is the maximal possible diagonal distance between the minimal position $\vec{x}_{min}$ (here: (-40,-40) mm) and the maximal position $\vec{x}_{max}$ (here: $(40, 40)$ mm) of the defined grid.

Therefore, the binary discretization-matrix $\mathbf{D}$ can be written as follows:

$$\mathbf{D}(x,y) = \begin{cases} 1 & \text{if } \frac{||\vec{x}_{OBJ} - \vec{x}_{CAL}||}{||\vec{x}_{min} - \vec{x}_{max}||} > threshold \\ 0 & \text{otherwise} \end{cases} \tag{4.14}$$
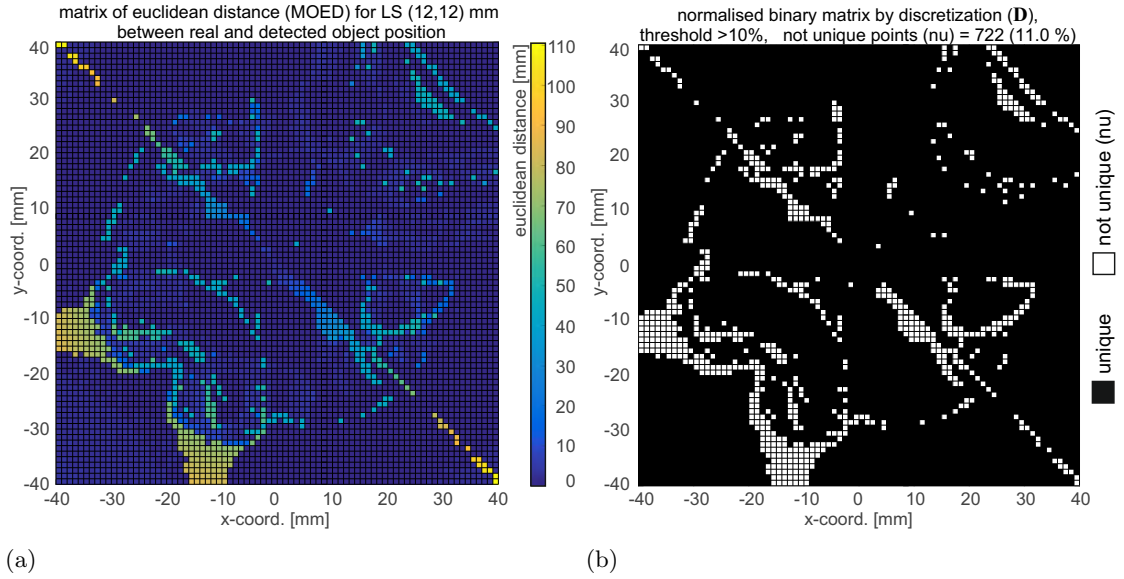
FIGURE 4.7: Matrix of Euclidean distance (MOED) and corresponding normalized binary matrix by discretization **D** to examine deviations between real ($\vec{x}_{OBJ}$) and detected (analytical solution) object positions ($\vec{x}_{CAL}$). (a) MOED as a result of a basic movement sequence consisting of the original sensor-emitter position (ORIG), a rotation by 45° (ROT45) and a linear shift by 12 mm in the x- and y-directions (LS (12, 12) mm). The colour of each pixel indicates the the Euclidean distances between real ($\vec{x}_{OBJ}$) and detected ($\vec{x}_{CAL}$) object position. (b) Normalized discrete matrix **D**, in this example for a threshold value larger than 10 %. The normalized distance corresponds to the maximum possible diagonal distance of the search area. White pixels within the discrete matrix **D** indicate that the object position cannot be uniquely identified, while black pixels identify unique object positions.

Figure 4.7(b) illustrates a binary matrix **D** for a threshold value of 10. White pixels represent non-unique object positions (nu-points), which will be counted for further processing and analysis. Figure 4.7 only visualizes one linear shift movement condition (LS (12, 12) mm) within the basic movement sequence (ORIG, ROT45, LS). If all cases of linear shift movements are to be evaluated and trends have to be investigated, an evaluation matrix as presented in figure 4.8 is used.

This example illustrates normalized tolerances of Euclidean distances between known real ($\vec{x}_{OBJ}$) and calculated ($\vec{x}_{CAL}$) object positions in dependence of different threshold values (from (a) 1 % to (i) 20 %). In figure 4.8 a single pixel within one of the evaluation matrices visualizes the percentage of nu-points within the binary matrix as shown in figure 4.7(b). The relative number of nu-points is represented in relation to the total number of pixels per search matrix. Here, all cases of LS-conditions (LS (0...14, 0...14) mm) for different threshold values are explored. For thresholds larger than 3 %, a diagonal trend to the upper right corner can be observed. The resulting uniqueness for these cases is better than 85 %. In each matrix, the red pixel indicate the shift condition with the highest number of unique object positions.
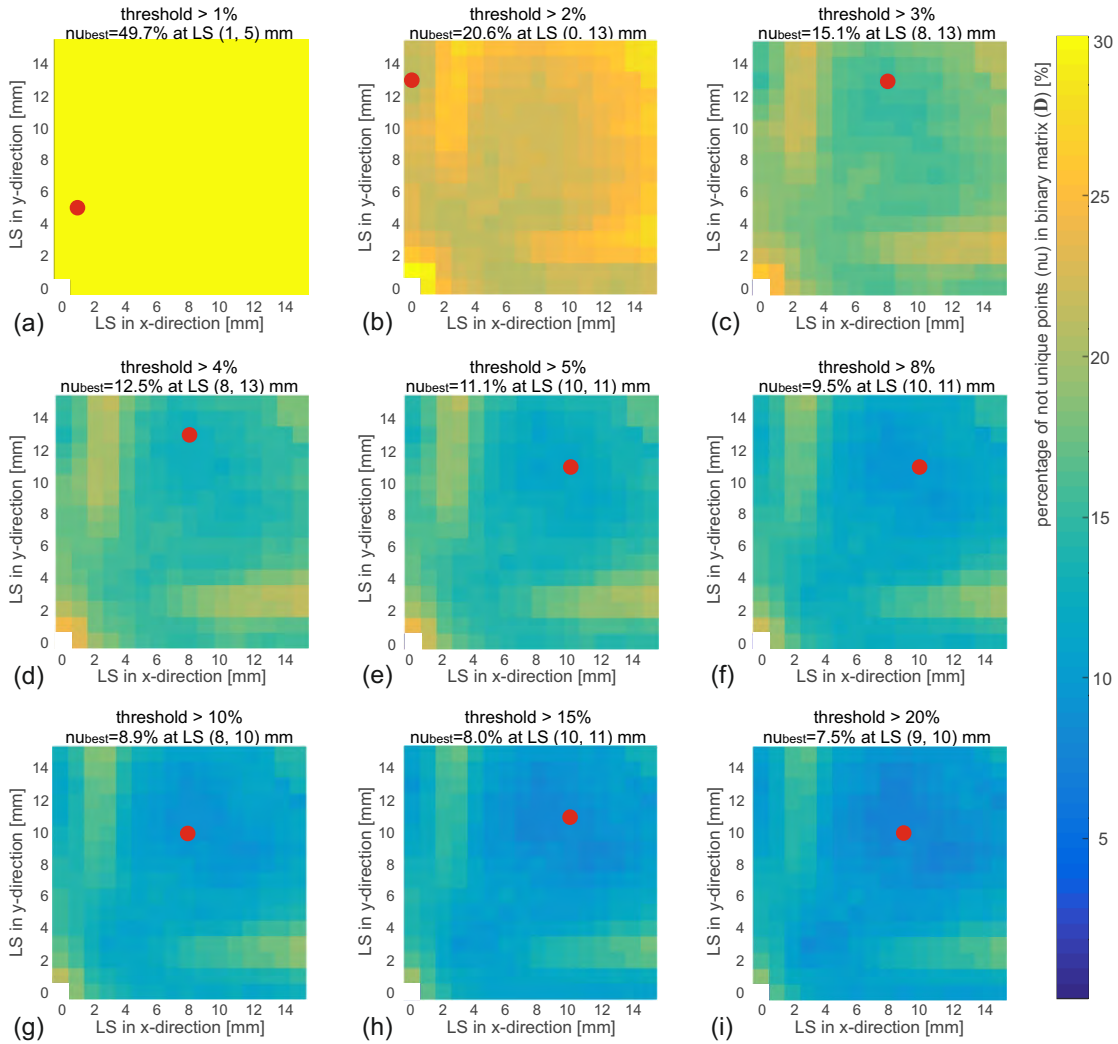
FIGURE 4.8: Evaluation matrix for all cases of linear shift movements according to different threshold values for normalized tolerances of Euclidean distances between real ($\vec{x}_{OBJ}$) and calculated object positons ($\vec{x}_{CAL}$). The evaluation is performed by using the basic movement sequence (ORIG, ROT45, LS). (a)-(i) The colours within the the matrices indicate the percentage of nu-points within the binary matrix **D**. Here, real object positions are represented by inputs from an FEM-simulation. All cases of linear shifts (LS (0...14, 0...14) mm) are investigated. A linear shift of 0 (LS (0, 0) mm) was not considered and is marked in white. The best result of a linear shift condition according to the evaluation matrix with a given threshold value is indicated by a red marker point. A diagonal trend to the upper right corner (darker shades of blue) can be noticed for thresholds more than 3 %. The uniqueness in these cases is better than 85 %.

4.3 Active electrolocation by means of a majority voting approach

In order to partition the search area into sectors, the basic localization algorithm includes a rotation of the sensor-emitter ensemble as a movement strategy. The linear shift movement is performed to prevent symmetrical intersections of the contour-rings. To increase the number of those locations in the search area where objects can be uniquely

localized, the basic movement sequence is extended by additional linear shift movements. When each of these different linear shifts is combined with the original EEV and the rotated EEV, an evaluation can be performed by using the basic localization algorithm. This results in several estimates of the possible object position. To decide on the best estimate of the position, a *majority voting approach* is applied subsequently.

4.3.1 Process sequence of the majority voting approach

Three linear shift movements constitute the basis for the majority voting approach introduced in this chapter. In figures 4.8(c)-(i), a diagonal shift direction is suggested as a first movement. Furthermore, a second shift in the x-direction and a third shift in the y-direction is assumed. Figure 4.9 illustrates an example application of this extended movement combination composed of three basic movement sequences. Here, in each line (a)-(e), (f)-(j) and (k)-(o) one different LS-condition has been applied, ORIG and ROT45 and the real object position ($\vec{x}_{OBJ}$) are fixed conditions.

As a result, three object positions $\vec{x}_{CAL1}$, $\vec{x}_{CAL2}$ and $\vec{x}_{CAL3}$ are calculated. They form the basis for a majority voting approach to determine the most likely object position. For this, the minimal Euclidean distance of all permutations of the calculated object positions has to be investigated.

$$\Delta \vec{x}_{i,j} = \vec{x}_{CALi} - \vec{x}_{CALj} \tag{4.15}$$

Let i,j $\in$ {1,2,3} such that

$$\|\Delta \vec{x}_{i,j}\| = arg\,min(\|\Delta \vec{x}_{m,n}\| : m \neq n \quad \wedge \quad m,n \in \{1,2,3\}) \tag{4.16}$$

The final resulting object position $\vec{x}_{RES}$ is determined at the center point of the two positions with the smallest Euclidean distance.

$$\vec{x}_{RES} = \frac{\vec{x}_i + \vec{x}_j}{2} \tag{4.17}$$

The next section examines by how much the localization accuracy is improved when using the triple LS-approach.
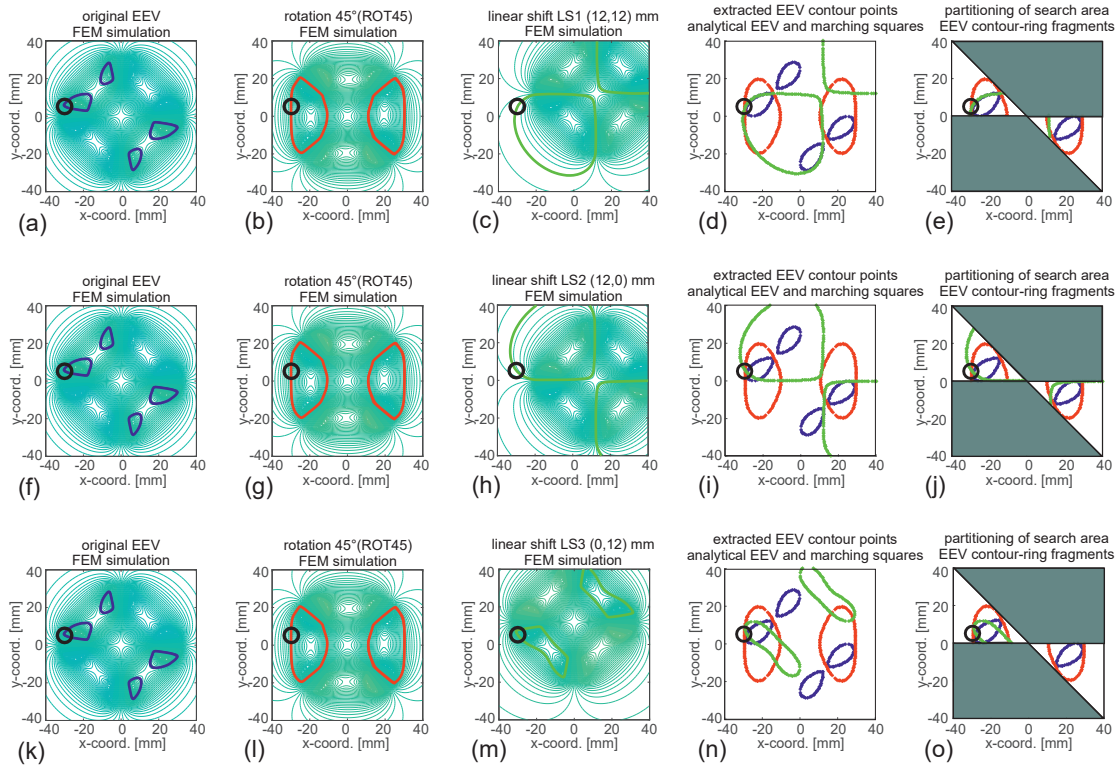
FIGURE 4.9: Application example of an extended movement approach which consists of three basic movement sequences. Each sequence contains a different LS, ORIG and ROT45 are fixed conditions. The three results are the foundation for a majority voting approach to find the most likely object position. In this example, the known real object position is x_{OBJ} (-30, 4) mm. (a)-(e) Basic movement sequence for a linear shift of 12 mm in the x- and y-directions LS1 (12, 12) mm. The calculated object position for this composition/sequence is x_{CAL1} (-29.1, 3.9) mm. (f)-(j) Same conditions but for a linear shift of 12 mm in the x-direction only LS2 (12, 0) mm. Here, a large deviation of the calculated object position at x_{CAL2} (12,4, -8.0) mm can be noticed. (k)-(o) Linear shift of 12 mm in the y-direction only LS3 (0, 12) mm. This results in a calculated object position at x_{CAL3} (-29.1, 5.2) mm. The three resulting possible object positions x_{CAL1}, x_{CAL2} and x_{CAL3} are used to search for the minimal Euclidean distance of all their permutations. According to the idea of a majority voting approach, the center point of the two results with minimal Euclidean distance represents the object position x_{RES}. In this example x_{CAL1} and x_{CAL3} show the smallest Euclidean distance. As a consequence, the final resultant object position is located at the center point x_{RES} (-29.1, 4.5) mm. The distance (error) between known real and calculated object locations is 1.04 mm or 0.92 % with regard to the normalized distance.

4.3.2   Method of separate discretization for the superposition process

In figure 4.9 the result of the majority voting approach using one triple LS-condition is shown for a single object position only. However, all permutations of linear shifts for all object positions have to be investigated in order to obtain information concerning the uniqueness of all object positions and to provide recommendations for optimal LS movement combinations. For this, a strategy is pursued that searches for the best combination of triple LS movements with the smallest number of nu-points.

Based on a defined threshold, binary matrices for each of the three movement sequences containing one of the triple LS-conditions (ORIG, ROT45, LS1...3) are generated according to equation (4.14). This is the precondition for the *superposition process* of these three discretized matrices with different linear shifts. As a result, a majority voting approach matrix ($\mathbf{D}_{MVA}$) consisting of values between 0 and 3 is generated.

$$\mathbf{D}_{MVA}(x,y) = \sum_{i=1}^{3} \mathbf{D}_i(x,y) \tag{4.18}$$

Within this matrix $\mathbf{D}_{MVA}$, the values 0 and 1 identify unique object positions, the values 2 and 3 represent positions which are not unique. Thus, the resulting matrix $\mathbf{D}_{RES}$ is determined as follows:

$$\mathbf{D}_{RES}(x,y) = \begin{cases} 1 & \text{if} \quad \mathbf{D}_{MVA}(x,y) = 2 \quad \vee \quad \mathbf{D}_{MVA}(x,y) = 3 \\ \\ 0 & \text{otherwise} \end{cases} \tag{4.19}$$

The values 1 within matrix $\mathbf{D}_{RES}$ represent nu-points, which are counted. Here again, the result is used for an assessment of the uniqueness of object positions.

An example of the majority voting approach for all object positions by using three different linear shifts is illustrated in figure 4.10. For a defined and fixed threshold value, the results of this *separate discretization method* are depicted in figure 4.10(e)-(g). In this case, all binary matrices $\mathbf{D}$ are generated with a threshold larger than 10 %. By using the majority voting approach, the final matrix $\mathbf{D}_{RES}$ as shown in figure 4.10(h) can be generated. For this, the three single matrices $\mathbf{D}$ (equation (4.18)) have to be added up and treated according to equation (4.19).

4.3.3 Results of majority voting approach compared to the basic movement sequence

Based on each LS-condition, the separate discretization and superposition process can be used for a fast investigation of all permutations of the triple LS combinations by applying the majority voting approach. For a defined threshold the aim is to find the best combination with the smallest number of nu-points. The comparison of the results of nu-point object positions between the basic movement sequence and the majority voting approach depending on different combinations of linear shifts and threshold values is demonstrated in table 4.1. The best results of the basic movement sequence presented
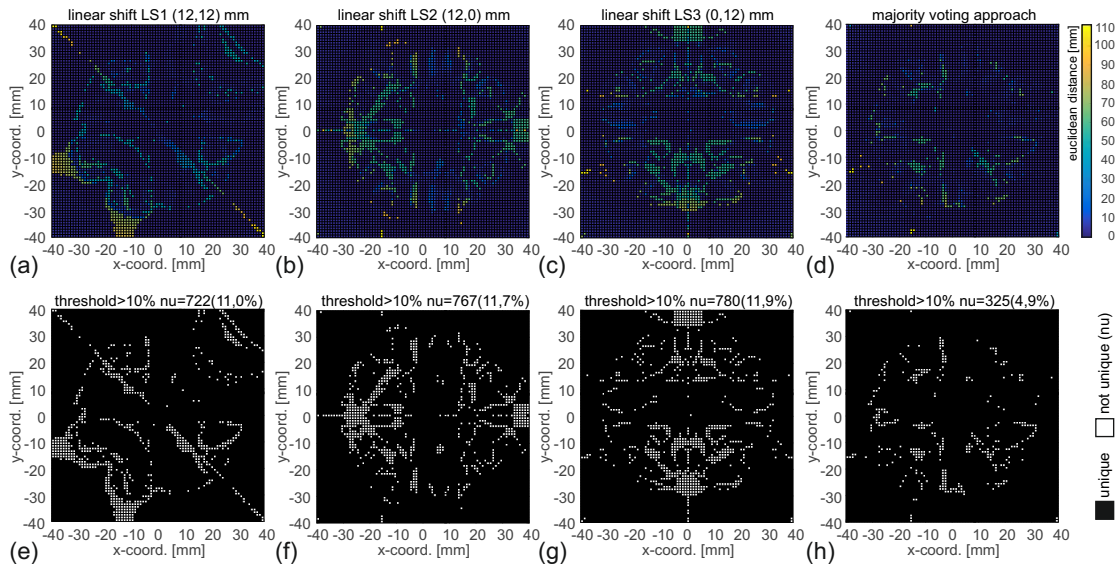
FIGURE 4.10: Example result of majority voting approach for all object positons within the search area using different linear shifts. (a) MOED for a linear shift of 12 mm in the x- and y-directions (LS1 $(12, 12)$ mm). The colors indicate Euclidean distances between known and calculated object positions. (b) MOED for a linear shift of 12 mm in the x-direction only (LS2 $(12, 0)$ mm). (c) MOED for a linear shift of 12 mm in the y-direction only (LS3 $(0, 12)$ mm). (d) Resultant matrix after using the majority voting approach. In comparison to the results of the basic movement sequence, this approach reduces Euclidean distances between known real and calculated object positions. (e) Normalized binary matrix by discretization $\mathbf{D}$ for a threshold value larger than 10 %. In figure 4.7, the illustrations of (a) and (e) were already shown before. (f) $\mathbf{D}$ related to the linear shift of 12 mm in the x-direction only, as shown in (b). (g) $\mathbf{D}$ for a linear shift of 12 mm in the y-direction only, referring to (c). (h) Resulting matrix $\mathbf{D}_{RES}$ for an implemented majority voting approach. Here again, the threshold value is larger than 10 %. This application uses the method of separate discretization and the superposition process as introduced in section 4.3.2. To analyze the uniqueness of possible object positions, the values of nu-points are counted. In this example, a significant improvement in comparison to the single results of the basic movement sequence demonstrated in (e)-(g) can be noticed.

in this table are already shown in figure 4.8 as red markerpoints. A trend towards diagonal shifts at approximately half the distance between the sensors and the center of the sensor-emitter array for a threshold larger than 3% can be noticed. Depending on these conditions, the uniqueness is better than 85%.

Furthermore, in table 4.1 the best results in terms of smallest number of nu-points and the respective best combinations of all permutations of linear shifts for different threshold values by using the majority voting approach are presented. In comparison with the results of the basic movement sequence, the uniqueness is considerably improved. In the last column of table 4.1, a modified majority voting approach for a specific case combining pure x-, pure y- and diagonally-directed linear shifts is shown. Compared with the best combinations of all permutations of the majority voting approach, no significant deterioration of nu-points can be observed. For this reason, this specific case

basic movement sequence			majority voting approach							best combination of	
best result of one linear shift			best combination of all permutations of linear shifts							pure x-, pure y and diagonal directed LS	
(LS)			(LS1-LS3)							(LSx, LSy, LSd)	
threshold	nu-best	nu-best at		nu-best			nu-best at				nu-best	for
[%]	[%]	LSx	LSy	[%]	LS1x	LS1y	LS2x	LS2y	LS3x	LS3y	[%]	comb.
1	49.7	1	5	48.3	10	5	2	4	1	5	49.6	5
2	20.6	0	13	14.3	15	0	9	11	0	13	14.9	13
3	15.1	8	13	8.7	15	1	9	11	0	13	9.6	13
4	12.5	8	13	6.7	13	0	10	12	0	13	7.4	13
5	11.1	10	11	5.6	13	0	10	12	0	13	6.5	13
8	9.5	10	11	4.2	14	1	10	11	6	5	5.4	13
10	8.9	8	10	3.7	14	1	10	11	6	5	4.9	12
15	8.0	10	11	2.7	15	0	11	9	0	11	3.8	12
20	7.5	9	10	2.3	15	0	11	9	0	11	3.4	12

TABLE 4.1: Comparison of results between the basic movement sequence and the majority voting approach. For this, different combinations of linear shift directions and pure x-, y- and diagonally-directed shifts are used. As a result, the smallest number of nu-points, their positions and the best combination are presented. For evaluation, different threshold values define the maximum permissible deviation (normalized Euclidean distances) between the known real ($\vec{x}_{OBJ}$) and the calculated object position ($\vec{x}_{CAL}$). The basic movement sequence uses only one linear shift within the corresponding movement sequence (ORIG, ROT45 and LS). In figure 4.8, the results and tendency are already illustrated. The majority voting approach uses the basic movement sequence three times, each with a different linear shift. For a threshold value of 8 %, the best result of using the basic movement sequence creates a share of 90 % of uniquely determinable object positions. By using the majority voting approach, these results can be improved to a value of 95 %.

is used for further investigation to find the best triple-LS combination with the smallest number of nu-point object positions for a defined threshold value. The percentage of nu-points within the binary matrix only for a combination of pure x-, pure y- and diagonally-directed linear shifts in which all three values are the same. The result is presented in figure 4.11. The best result of nu-points for all threshold values can be found for a value equal to approximately half the distance between the sensors and the center of the sensor-emitter ensemble.

4.4 Results of majority voting approach using real measurements

In the preceding sections, sensor inputs from FEM-simulations were used instead of real measurements to analyze the fundamental applicability of the introduced majority voting approach. The benefit of using FEM-simulations was the provision of perfect and noise-free potential differences between the sensor electrodes for all possible object positions.
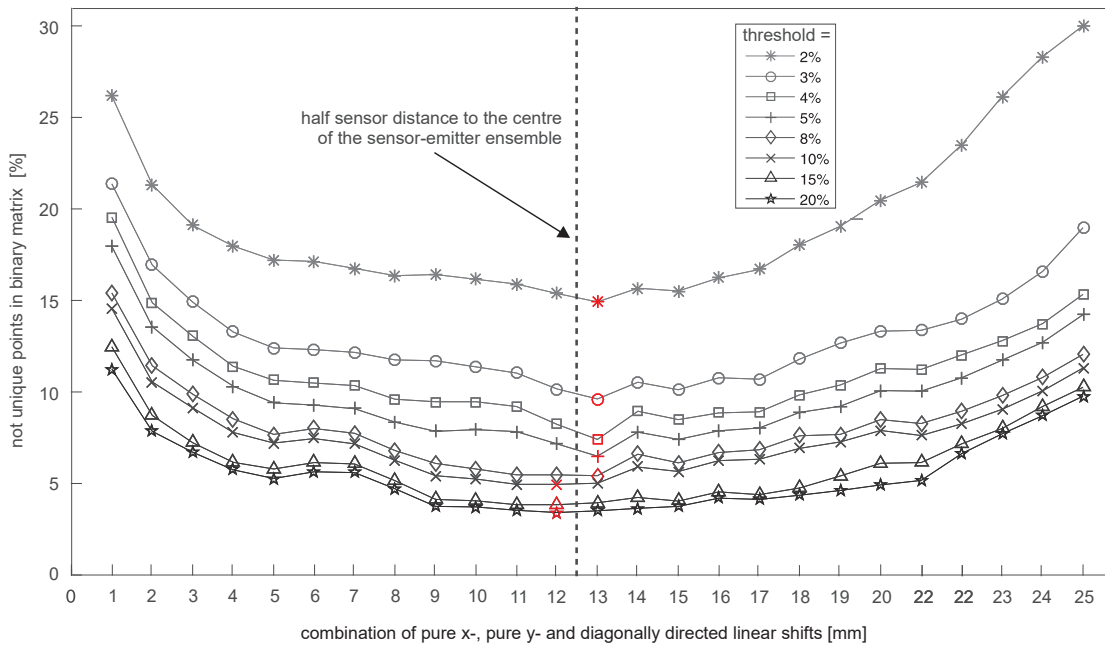
FIGURE 4.11: Percentage of nu-points within binary matrix for combinations of pure x-, pure y- and diagonally-directed linear shifts. The results are dependent on different thresholds for normalized Euclidean distances between real ($\vec{x}_{OBJ}$) and calculated object position ($\vec{x}_{CAL}$). By using the majority voting approach, a triplet of a pure x-, pure y- and diagonally-directed shift is applied to analyze the method and data. As an example represents the value 13 on the x-axis the combination $LSx = (13, 0)$ mm, $LSy = (0, 13)$ mm, $LSd = (13, 13)$ mm. In addition, in each curve a red markerpoint is included, which illustrates the best result with the lowest percentage of nu-points. For all threshold values, the best result of nu-points can be found at approximately half the distance between the sensors and the center of the sensor-emitter ensemble.

These perfect sensor values are used as reference for the evaluation of the algorithm for object localization. Thus, the accuracy of the proposed localization algorithm could be explicitly validated without the undesired side-effects of real measurements, such as noise. Furthermore, results should be obtained that are initially unaffected by constraints such as different object and fluid parameters, temperature, polarization effects at the electrodes and setup inaccuracies. The use of FEM-simulations enables identical boundary conditions with different test parameters to be repeated several times with reproducible results. In this section it is shown that the strategy can also be used on the basis of noisy data from a real measurement system.

4.4.1 Implementation of a real measurement system and first results

Inputs of real measurements, which represent object positions, are required during the validation of the majority voting approach. Therefore, a physical measurement system has been set up, containing a sensor pod which consists of four sensor-emitter electrodes. The electrodes are connected to an embedded mixed-signal hardware. As demonstrated in

figure 4.12(a), the entire setup is mounted on a robot with SCARA-kinematics (selective compliance assembly robot arm).

embedded hardware implemented on real robotic-setup   sensor pod with electrodes and object

(a)   (b)
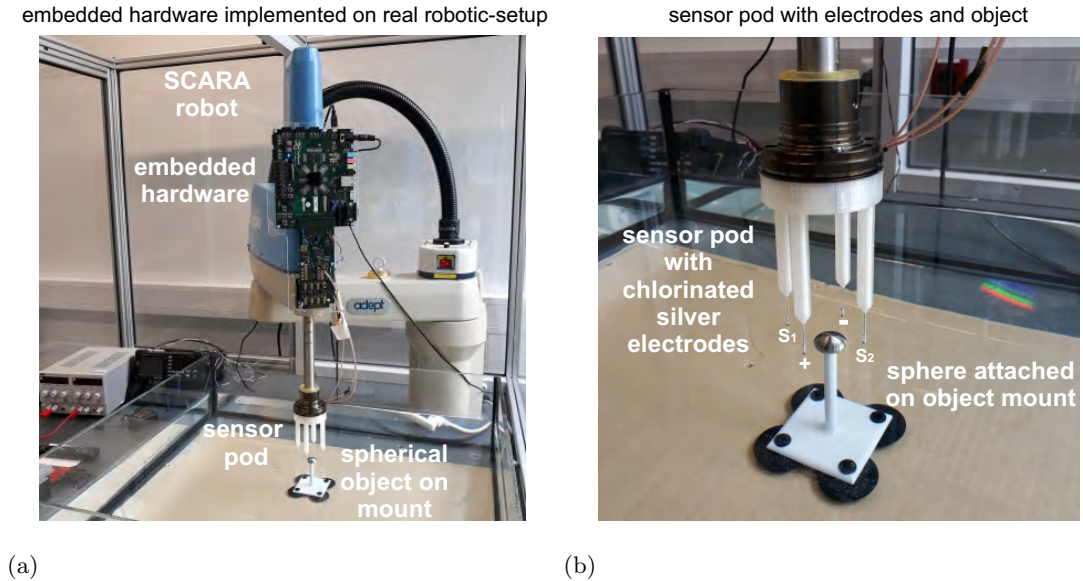
FIGURE 4.12: Robotic and sensor pod setup with embedded mixed-signal hardware for real measurements. (a) Real robotic setup, consisting of a four-axis SCARA robot on which a sensor pod is attached to its end-effector. The setup is used to generate EEVs by moving the sensor pod on a meandering path relative to a spherical object which is fixed on a mount and placed in a water-filled basin. By means of an external frequency generator, the electric dipole field is emitted via the emitter electrodes of the pod. Embedded hardware is used to perform the analysis and digital processing of the measured signals and their transfer to a PC. (b) Sensor pod with four chlorinated silver electrodes which are arranged orthogonally to each other. One pair acts as an emitter dipole, the other as sensor electrodes. All measurements are performed in the water at a distance of 1 mm above the spherical object.

The sensor pod, which is attached to the robots end-effector, is moved by the four-axis SCARA robot through a water-filled basin. In this case, the water has a defined conductivity of 400 μS/cm^{-1}. A conducting stainless steel sphere (r = 7.5 mm) is fixed on a mount which is placed in the water basin. A close-up view of the sensor pod including the electrodes and of the object on a mount is depicted in figure 4.12(b). The sensor pod contains four chlorinated and orthogonally arranged silver electrodes with radius r = 1 mm. One pair generates the electric dipole field, the other pair acts as measuring electrodes for sensing the signals. As already shown in figure 2.7(a), the distance between the two electrodes of each pair is 50 mm. Each electrode is inserted into a glass pipette which is sealed with glue as proposed by Rasnow (2005). An external frequency generator is used to generate an electric dipole field at the emitter electrodes with a 1 kHz sine signal with an RMS value of 1 V. The analogue signal measured at the differential electrode pair is amplified by a gain factor of G = 275. Subsequently, the analogue signal is converted into a digital signal by the embedded hardware for further

processing and analysis. To measure EEVs, a grid of 160 mm by 160 mm is scanned by the robot in 4 mm steps. The intermediate values are interpolated bicubically. At each position, the measuring time is 0.02 s (20 periods) with a sampling frequency of 100 MS/s. All measurements are carried out at a distance of 1 mm above the conductive sphere.

By application of a fast Fourier transform (FFT), the amplified signal is transferred to the fequency domain. To construct the entry for the EEV matrix at the respective measurement position, the amplitude of the 1 kHz component is selected from the amplitude spectrum. If an asymmetrical sensor arrangement is given due to inaccuracies in the physical setup, an offset may be recorded, which has to be subtracted from the measured values. Figure 4.13 demonstates measured and smoothed EEV matrices without offset.

Figure 4.13(a) illustrates a 3D-plot of a measured EEV. Particularly at the base region of the EEV in the range of about 0 V, a noise carpet can be observed. Based on this measured EEV, a 3D-plot of a smoothed EEV with a Gaussian filter with a standard deviation of $\sigma = 8$ can be seen in figure 4.13(b). In figure 4.13(c), a 2D-plot related to figure 4.13(a) is depicted. The smoothed 2D-plot in figure 4.13(d) corresponds to the 3D-plot in figure 4.13(b). In this example, an object is located at (-30,-30) mm which causes the blue highlighted EEV contour-rings. The comparison of the measured EEV and the smoothed EEV shows that the smoothed contour-rings emphasizes the natural partitioning of the EEV into four quadrants. It follows that the accuracy of the measurements is improved although the total range of the EEV is getting smaller because of the Gaussian filter. By multiplying the EEV by a suitable factor, the range of the EEV can be re-adjusted. Therefore, by subtracting both EEVs, the mean value of the absolute error between the analytically calculated EEV matrix and the measured EEV matrix can be calculated and subtracted from the EEVs. For further measurements, this calculated factor will be retained as a constant value.

The validation process of the majority voting approach includes the results of unfiltered and filtered measurements. The same method as in section 4.3 is applied to analyze the results but here real measurements are used as inputs instead of simulations. By using the majority voting approach, table 4.2 shows the results of real measurements for a fixed triple combination, composed of pure x-, pure y- and a diagonally-directed shift of half the distance between sensor electrode and the center of the sensor-emitter array (12.5 mm). Here, the results are depending on different threshold values for normalized Euclidean distances between the known real ($\vec{x}_{OBJ}$) and calculated ($\vec{x}_{CAL}$) object positions. Furthermore, unfiltered and various filtered EEV matrices (Gaussian filter with $\sigma = 6...10$) are analyzed. A standard deviation of $\sigma = 9$ causes the best result
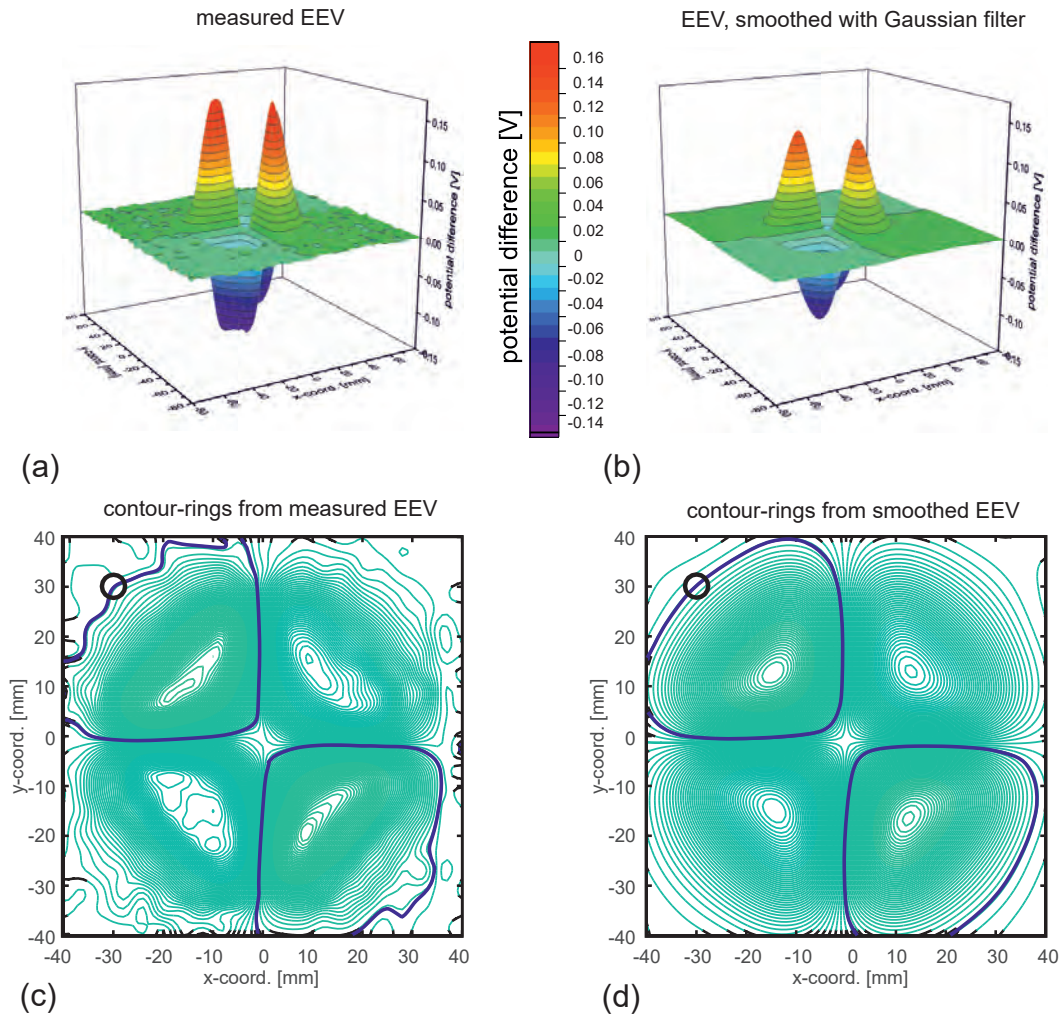
FIGURE 4.13: Comparison of measured EEV matrix and an EEV matrix smoothed with a Gaussian filter. (a) 3D-plot of a measured EEV. Particularly at the base area at potential differences of about 0 V, a noise carpet can be observed. (b) 3D-plot of a measured EEV matrix as in (a) but smoothed by a Gaussian filter (standard deviation $\sigma = 8$). (c) 2D-plot of a measured EEV corresponding to (a) with an object located at (-30, -30) mm. The object causes a potential difference that can also be measured along the blue EEV contour-rings. The noise, especially in the range about 0 V, leads to the distortion of contour-rings in the exterior region of the EEV. (d) 2D-plot of smoothed EEV, corresponding to (b). For an object at the same position as in (c), the EEV contour-rings are extracted. The deviations are reduced by the smoothing which improves the measurement accuracy in the area that exhibits small gradients.

with a share of about 80 % unique object positions ($\sim$20 % non-unique object positions). This is indicated in table 4.2 by a red rectangle.

4.4.2 Optimization of the measurement results

Compared to the results of simulation shown in table 4.1 which represent ideal and reproducible values, the results of real measurements presented above contains potential

majority voting approach (real measurements)						
for combination LSx = (12.5,0) mm, LSy = (0,12.5) mm, LSd = (12.5,12.5) mm						
filtered EEV-matrix by Gaussian filter with standard deviation specified by σ						
filter	no filter	σ = 6	σ = 7	σ = 8	σ = 9	σ = 10
factor	0.4	0.49	0.52	0.55	0.6	0.6
threshold	∩∪-best	∩∪-best	∩∪-best	∩∪-best	∩∪-best	∩∪-best
[%]	[%]	[%]	[%]	[%]	[%]	[%]
1	94.8	90.2	88.0	89.0	93.5	95.9
2	83.4	72.0	72.0	72.5	77.2	83.9
3	71.0	55.6	55.8	57.7	62.8	68.9
4	63.7	44.6	42.2	42.1	50.7	56.7
5	58.5	39.4	36.2	33.1	37.1	46.0
8	50.8	33.6	29.6	24.5	23.5	26.6
10	48.2	31.8	27.5	22.6	21.4	23.9
15	44.3	30.5	26.4	21.5	19.8	21.3
20	41.9	29.9	26.3	21.5	19.8	21.1

TABLE 4.2: Results of real measurements based on the majority voting approach. They are determined for different threshold values for normalized Euclidean distances between the known real ($\vec{x}_{OBJ}$) and the calculated object position ($\vec{x}_{CAL}$). A fixed triple combination composed of pure x-, y- and a diagonally-directed shift in half-distance (12.5 mm) between the sensors and the center of the sensor-emitter ensemble is applied. An EEV matrix without filter is compared to different filtered EEV matrices which are created by a Gaussian filter with standard deviation specified by different σ. The best result with a share of 80% unique object positions is indicated in the table by a red rectangle.

for optimization. In order to get as close as possible to the quality of these ideal results, the following optimizations have to be carried out:

- An offset will be reduced by maintaining a precise symmetry in all dimensions of the real sensor pod.

- First measurements were realized at a small distance above the spherical object. To intensify distortions of the electric field, caused by the object, and their resultant EEVs, upcoming measurements could be performed at the height level of the object. To avoid collisions with the object, the positioning of the sensor pod has to be monitored.

- The errors caused by interpolation could be reduced by a field scan with a smaller step size (higher resolution).

- Long-term measurements are influenced by temperature. This effect has to be examined by further measurements. Like for all other parameters of the fluid and the object it has to be ensured, that the temperature is also kept constant.

4.5   Summary

Based on EEVs, a general movement strategy for active electrolocation of an object was introduced in chapter 3 and (Wolf-Homeyer et al. 2016). Here, the composition of EEV contour-rings of an original position (ORIG), a 45° rotated (ROT45) and of a linearly shifted (LS) sensor-emitter ensemble was identified as the minimal necessary set of scanning movements. These results were determined by means of FEM-simulations of the electric field. Based on an analytical calculation of EEVs, the current chapter examined open questions without computationally expensive FEM-simulations. Hereby, the advantage arises that the calculations can be conducted on embedded hardware systems for robotic applications.

In the first step of the strategy introduced in this chapter, the minimal set of scanning movements is applied. The rotation by 45° within the composition of movements allows a partitioning and a resultant exclusion of sectors of the search area. Beforehand, a discrete EEV matrix is generated from the simplified analytical formulation. Depending on the potential difference measured at the sensors, the contour-ring points (CRPs) are extracted by application of a marching squares algorithm. The partitioning of the search area leads to a fragmentation of the extracted EEV CRPs. As a result, for each orientation of the sensor-emitter array, a subset of 2D discrete EEV CRPs of desired accuracy can be determined. In Wolf-Homeyer et al. (2016) the intersections of EEV contour-rings were used to calculate the position of the object. Instead of intersections, in this chapter a nearness metric from the CPR subsets is introduced and used for object localization. This strategy is less sensitive to inaccuracies of measurements or discretization effects that possibly lead to blurred EEV contour-rings. As a consequence, this strategy reduces the number of ambiguous object positions.

The application for active electrolocation introduced in this chapter is implemented independently of probabilistic models (e.g. Kalman filter, Bayes filter) as opposed to Lebastard et al. (2013); Solberg et al. (2008); Y. Silverman et al. (2012) and Y. Silverman et al. (2013). In contrast to these more complex and high level procedures this method goes a step back and takes up the concept of EEVs again. Thus, existing information from unprocessed data can be extracted. The application is only dependent on direct sensor readings of a simple sensor-emitter ensemble. Thus, the measured potential differences at the sensor electrodes allow the generation of EEVs, which provide direct information on possible object positions. In combination with a minimal set of movement conditions arranged in a fixed sequence, a unique localization of an object is enabled. This concept differs from probabilistic approaches like particle filters but it can be used as a pre-processing step for such higher level algorithms. Within the particle filter algorithm, each possible object position is represented by discrete particles with different likelihood

weightings. The aim is to minimize the expected variance of the particles. Therefore, the controller continuously has to predict and update this probability to make a hypothesis of where the object can be identified. However, the application introduced here can be implemented independently of recursive procedures.

On basis of the time complexity of each single algorithmic part, the time consumption of the complete application can be determined. The four general steps of the algorithm are demonstrated in the flow chart in figure 4.3. At first, the initial data acquisition and the calculation of the field is performed once. Hence, a low computing time with constant time complexity is consumed in both steps. The EEV contour-rings are extracted by means of a marching squares algorithm. This exhibits a low and linear time complexity of O(n). This step can be implemented in a computationally efficient way. Within the last step, the identification of the object candidates is based on a nearness metric. This shows a cubic time complexity of O(n^3). The reason for this is that the contour-lengths of the triangles of all possible permutations from the three subsets (ORIG, ROT45, LS) have to be compared with each other. As a result, the triangle with the smallest nearness in each sector has to be selected. An improvement of the time consumption is possible if the resolution of the marching squares algorithm is reduced. Furthermore, the method of partitioning reduces the search area to a quarter of the original area. Consequently, the number of CRPs is approximately reduced to one quarter of its initial value.

The weakly electric fish is used as biological inspiration for the application presented here. An electric field is generated by specialized muscle cells in the tail region of the fish. A large number of electroreceptors distributed all over the fish's skin perceive distortions of the self-generated field, caused by objects (Nelson and MacIver 2006). Compared to the biological receptor-emitter system of fish, the technical equivalent realized in this application is composed of a simple emitter dipole and a pair of sensor electrodes which are arranged symmetrically and orthogonally with respect to each other.

As an improved strategy to the above described basic movement sequence, a majority voting approach was also introduced in this chapter as an active electrolocation algorithm. Therefore, the minimal set of scanning movements is used three times, each with a different linear shift. Based on the three results, the majority voting approach is applied to extract the most likely object position. The algorithm uses the calculated object position from each of the three trials and determines the Euclidean distance of all possible combinations of these results. At the center point of the two results with minimal Euclidean distance, the final resulting object position is assumed.

A composition of a pure x-, a pure y- and a diagonally-directed linear shift is used for a modified majority voting approach. The best triple combination of linear shifts for this specific case can be located at a value of approximately half the distance between the

sensors and the center of the sensor-emitter array. It is caused by the general shape of the EEV as illustrated in figures 2.8(a) and 2.8(b). In the base region of the EEV at a measuring range of about $0\,\mathrm{V}$, EEV rings with a large contour-length are extracted. As a consequence, a high number of possible object positions can be detected. Furthermore, this region exhibits a small gradient which leads to significant divergences of the possible object positions, even if the measurement accuracy shows only slight deviations. In contrast to this, the higher level regions of the EEV, for both positive and negative values of potential differences, show larger gradients and smaller contour-lengths of the extracted EEV rings. The advantage of this is that the number of possible object positons is reduced and possible measurement deviations cause only minor effects. Consequently, the search area can be reduced again and the ambiguous object position can be determined more accurately if a combination of EEV contour-rings is used which contains a large number of extracted contour-rings from higher regions of the EEVs. The results in figure 4.11 show that it can be achieved by shifting the sensor-emitter ensemble by a value of half the distance between the sensors and the center of the array. The realization of the movement conditions of the sensor-emitter ensemble could be carried out by switching between different sets of sensor electrodes in a sensor array. Both localization algorithm introduced in this chapter are prepared for implementation on an application-oriented embedded hardware system.

5

Evaluation of a fitted histogram representation of EEVs for the estimation of an optimal composition of movement sequences

Abstract

Weakly electric fish are capable of performing active electrolocation. This ability is supported by performing swimming movements, presumably to scan interesting objects. Based on this, bioinspired approaches have already been introduced in chapters 3 (Wolf-Homeyer et al. 2016) and 4 (Wolf-Homeyer et al. 2018) for the unique localization of an object. At first, a minimum set of scanning movements of a sensor-emitter system, composed of an original, a rotational and a linear shift movement was proposed as an optimal concatenation of movements. Based on this, an application for active electrolocation was introduced. As in the present chapter, a symmetrical receptor system consisting of a sensor pair and an orthogonally arranged emitter pair is chosen in all investigations. The basic principle behind all localization strategies is the superposition of extracted EEV contour-rings. Intersections or the nearness of the individual rings provide information about possible object positions.

In this chapter, a fitted histogram representation of the EEVs, based on the kernel density estimation, is used to be able to compare a large number of different movement sequences. The examination is performed by means of histograms which are created by the simplified analytical representation of the potential differences from the resulting EEVs as introduced in chapter 4. By using a histogram fit strategy, all possible movement combinations, consisting of original, rotated, and shifted sensor-emitter ensemble can then be tested in a brute force approach. The overall best sequence can be determined by finding exactly the movement sequence whose combined EEV is represented by a density fit curve with the smallest maximum.

5.1 Consideration of the general shape of an EEV by means of a histogram representation and density fit curve

Inspired by the biological model of weakly electric fish, in chapter 3 and in Wolf-Homeyer et al. (2016) a minimal set of scanning movements of a receptor system was proposed to detect objects by active electrolocation. The optimal concatenation of movements derived here is composed of the original EEV, a rotation and a linear shift of the original EEV. The basic principle behind the scanning strategy is based on the superposition of numerical extracted contour-rings of FEM-simulated and differently moved EEVs which leads to intersections of the extracted contours. These intersections provide possible object positions. At each point of the search area, different potential differences can be measured, hence different sized contour-rings are formed. Two different discretization strategies (CEN and RPD) are implemented for the numerical extraction of EEV contour-rings. However, the strategies depend on the respective parameters ϵ and $\Delta\varphi_r$ which have to be defined beforehand. In addition, blurred measured values have to be compensated by adjusting these parameters. Since the strategy is also dependent on time-consuming simulation results, an optimal movement sequence was only determined by solely concatenating the prior best movement conditions and not by investigating all possible permutations. Furthermore, the test conditions were limited to a linear shift of $0\,\mathrm{mm}$ to $9\,\mathrm{mm}$ in $1\,\mathrm{mm}$ steps, both in x- and y-direction, due to the high computational effort.

Chapter 4 and Wolf-Homeyer et al. (2018) introduce an application for active electrolocation based on the minimum set of scanning movements proposed in chapter 3. A reduced sensor movement sequence composed of the original EEV and an EEV rotated by $45°$, is used as a precursor for a fragmentation of the contour-rings. This fixed rotational movement is required to perform the maximal reduction of the search area. Based on an analytical calculation of the EEVs and independently of computationally expensive simulations, two localization algorithms are introduced in this chapter 4, which require only the fragments of discrete EEV contour-rings. As modification of the intersection method, the localization algorithms use a nearness metric to examine for each sensor-emitter shift (orientation of $0\,\mathrm{mm}$ to $25\,\mathrm{mm}$ in $1\,\mathrm{mm}$ steps, both in x- and y-direction), whether the identified object positions are unique. By using the majority voting approach, in which again each point of the matrix has to investigated, the best triple combination of linear shifts can be located by shifting the sensor-emitter ensemble by a value of approximately half the distance between the sensors and the center of the sensor-emitter array. This extensive investigation in chapter 4 was possible because the rotational movement was a fixed parameter, but it would have been overly time-consuming if all rotations had been involved in the study.

The empirically determined results shown in the preceding chapters suggest that the basic shape of the EEV, as depicted in figure 5.1(a) as a 2D-plot and 5.1(b) as a 3D-plot, plays a major role in estimating an optimal composition of a movement sequence. The EEV's extensive base region at a range of about $0\,\text{V}$ causes extracted EEV contour-rings with a large contour length. Consequently, a high number of possible object positions can be identified. In addition, this region exhibits a small gradient of the potential differences. Even if slight deviations in the measurement accuracy are present, significant differences of possible object positions may result. On the contrary, regions of larger potential differences (higher level regions) in the EEV show smaller contour-lengths of the extracted contour-rings with larger gradients. Hence, the number of possible object positions is reduced and only minor effects are caused by possible deviations of the measurements e.g. due to noise.

The example in figure 5.2 compares the superposition of extracted EEV contour-rings using the same movement sequence but the object is assumed at different positions. In figure 5.2(a)-(d) the object is located far away from the sensors and emitters. As a consequence, large contour-rings in the range of about $0\,\text{V}$ are extracted for the three movement operations in the sequence. The result of the superposition in figure 5.2(d) illustrates, that a unique object localization is not possible, since several contour-rings run almost in parallel to each other at very low distances. If a combination of EEV contour-rings is used, which contains a large number of extracted contour-rings from higher levels of the EEV, a unique object position can be identified more accurately. The example in figure 5.2(e)-(h) demonstrates such a case. Since the object is located closer to the sensor-emitter array, smaller contour-rings are selected. Furthermore, the result in figure 5.2(h) also shows that the linear shift movement is required in order to break the mirror symmetry caused by purely rotational movements on the one hand and to provide combinations of extracted EEV contour-rings, consisting of the base region and regions from higher levels on the other. It is easier to identify points of intersection which favor the uniqueness of the object localization.

To avoid that contour-rings have to be extracted again for each point in the search matrix and for each movement condition, so that the result can be examined for uniqueness by a superposition and by using an intersection method or nearness metric, a new strategy is introduced. For this, fitted histogram representations of the EEVs are required to identify an optimal composition of movements from a large number of movement sequences. The histogram depicted in figure 5.1(c) is based on the EEV already shown in 5.1(a) and (b). The heights of the bins illustrate the relative frequency density of the potential difference of the EEV. In addition, a smoothed density fit curve of the histogram, generated by a *kernel density estimation* (KDE) (Rosenblatt 1956; Parzen 1962), is presented in black. This fit curve allows the estimation of the probability distribution within the EEV for
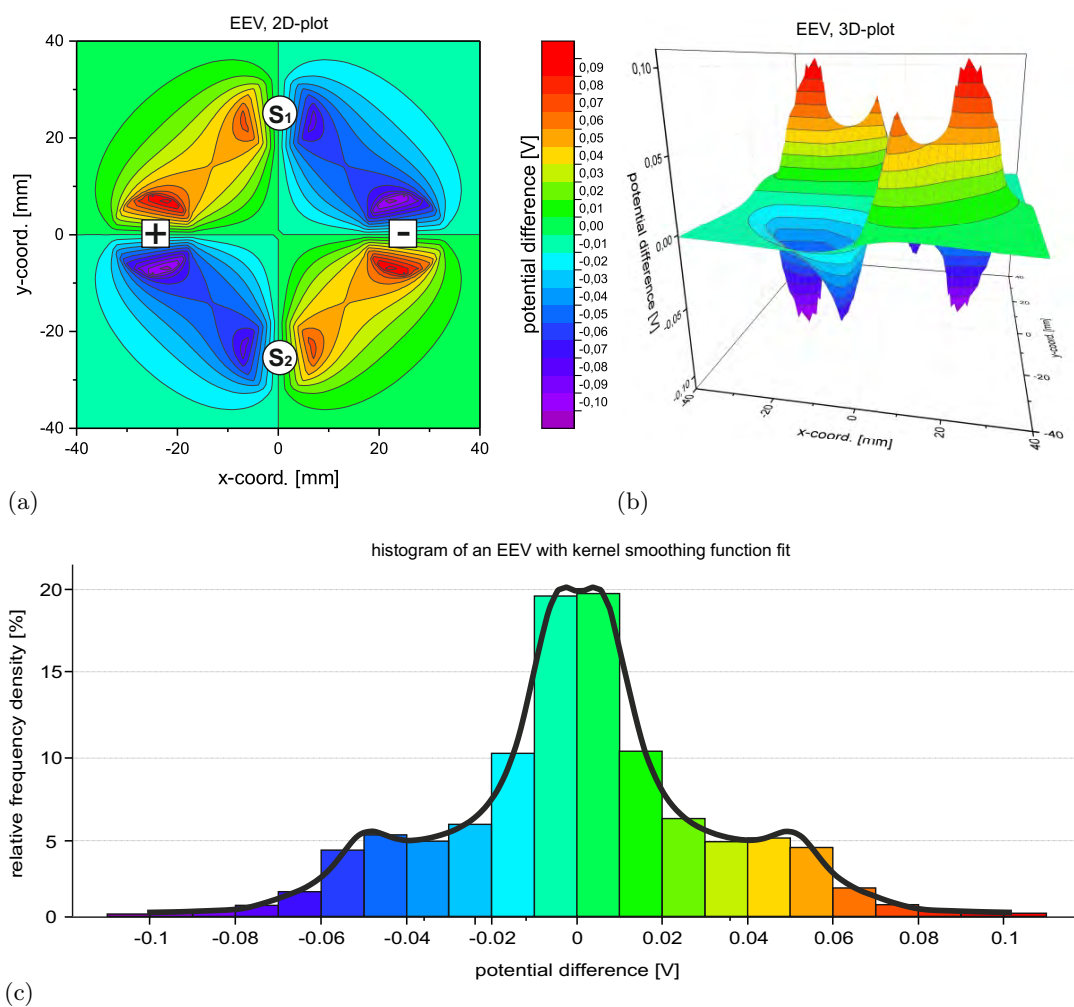
FIGURE 5.1: 2D- and 3D-plot of an EEV and the corresponding histogram with kernel smoothing density fit curve. (a) 2D-plot of a FEM-simulated EEV. This visualization also shows the sensors S_1 and S_2 and emitters (labelled + and -), which are symmetrically and orthogonally arranged to each other. Depending on the potential difference measured at the sensors, mirror symmetrical EEV contour-rings of different sizes can be extracted. (b) The general form of the EEV is represented as a 3D-plot. In the range of about $0\,\text{V}$ only small gradients of the potential differences can be found which leads to contour-rings with large contour-lengths. As a consequence, a high number of possible object positions can be identified. In the higher level regions of the EEV the contour-lengths of the extracted EEV rings are smaller and the gradients of the potential differences are larger. The advantage of this is that the number of possible object positions is reduced and inaccuracies in potential measurements show smaller effects. (c) Histogram of an EEV with a kernel smoothing density fit function. The individual bins of the histogram, which are of equal width, are also color-coded according to the legend shown between (a) and (b) to indicate the respective potential difference at the sensors. The heights of the bins indicate the relative frequency density, i.e. their total sum equals 100 %. The smoothed density fit curve, illustrated in black, was generated based on a kernel density estimation as introduced in section 5.2.

discrete points independently of a parameterization. This will play an important role in the strategy elucidated in the following section.

FIGURE 5.2: Comparison of a superposition of extracted EEV contour-rings using the same movement sequence but for different object positions. The two examples shown in (a)-(d) for an object at position 1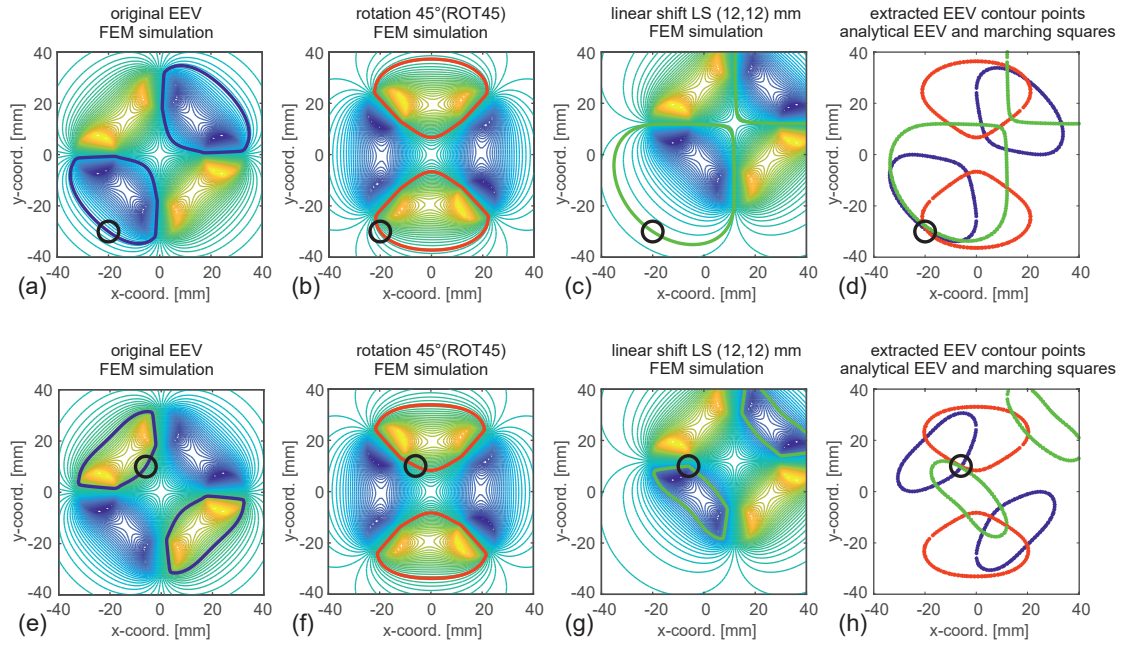 (-10, -30) mm and in (e)-(h) for an object at position 2 (-6, 10) mm were based on the composition of the original EEV matrix ((a) and (e)), a rotational movement by 45° ((b) and (f)) and a linear shift of 12 mm in both x- and y-directions ((c) and (g)). (d) Result of the superposition of extracted EEV contour-rings for position 1. In this case, the object is situated far away from the emitters and sensors, so the contour-rings extracted for all three movement sequences are comparably large. In this case, it is not possible to identify a unique object position by using the intersection method or the nearness metric derived from it, because several contour-rings run in parallel at a close distance to each other. In addition, large EEV contour-rings also imply many possible object positions. (h) Result of the superposition of extracted EEV contour-rings for position 2. A combination of small and large contour-rings enables a unique object localization, since intersection points of the rings can be clearly identified.

5.2 Estimation of an optimal composition of movement sequences based on a fitted histogram representation of EEVs

As mentioned in the introductory section 5.1, the aim of the fitted histogram representation is to determine optimal combinations from a large number of movement sequences that provide a unique localization of objects in the widest possible search area. For the introduced strategies, each discrete point within the search matrix has to be examined for uniqueness. For each point the potential difference has to be measured separately with respect to each movement condition. After that, the corresponding EEV contour-rings have to be extracted and the intersection points or the nearness of the rings have to be determined to be able to perform a localization and to obtain a prediction about the uniqueness. The method introduced in this chapter, referred to as *histogram fit strategy*,

examines the totality of the points contained in a search matrix, which significantly reduces the analytical effort. A second advantage of this strategy is that only the superposition and not each individual movement condition of the sequence to be observed will be analyzed.

In figure 5.3, the histogram fit representations of EEVs is illustrated to identify an optimal composition of movement sequences. Based on a kernel density estimation, the density fit curve, which is an envelope of the histogram of EEV potential differences, can be determined to estimate an optimal composition of movement sequences. Figures 5.3(a)-(c) show an example of a sequence, composed of an analytically calculated original EEV (ORIG), a rotated EEV by 45° (ROT45) and a linearly shifted EEV both in x- and y-direction (LS $(12.5, 12.5)$ mm). Figures 5.3(d)-(f) exemplary depict the respective histogram fit representations. Here, the absolute values of the potential differences within the analytically calculated EEV matrix are used. In addition, the matrices are normalized to a value range between 0 and 1. The resulting data is plotted as a histogram for which the number of bins was arbitrarily set to 20. It has to be emphasized that the KDE is independent of the choice of bin numbers of the histogram, since the latter only serves the visualization of the value distribution. The estimation of the density fit curve itself, however, is based on a sample of 100 values from the respective EEV.

The essential part of the strategy is visualized in figure 5.3(g). Again, a histogram fit representation is shown, but in this case it was obtained from a superposition of the absolute matrices of ORIG, ROT45 and LS$(12.5, 12.5)$ mm. To improve the comparability of different movement sequences, the superposition is followed again by a normalization. Compared to the results of each single movement condition presented in figures 5.3(d)-(f), the maximum value of the density fit curve (colored in red) decreases when a superposition is used. A further effect that can be observed in the histogram is that the frequency is more evenly distributed and thus also the mean value of the gradient of the curve is reduced. As the most important aspect of the procedure, it is this uniform distribution of potential differences which is desired. By superposition of EEV matrices from a sequence composed of different movement operations, a combination of potential values is obtained for each discrete point. Now the objective is to find those combinations for which the number of potential differences in the range of 0 V is minimized, since these values are the main reason for a non-unique object localization. In the histogram, respectively in the density fit curve, these unwanted combinations can be found in the left part, i.e. in the region of the first bins. The strategy does not examine each individual point of the superimposed EEV matrices but the totality of the points within the resulting matrix. Thus, also a large number of movement combinations can be examined to identify the best sequences using a suitable selection of movements. The movement sequence with the lowest maximum value of the density curve represents the best combination.
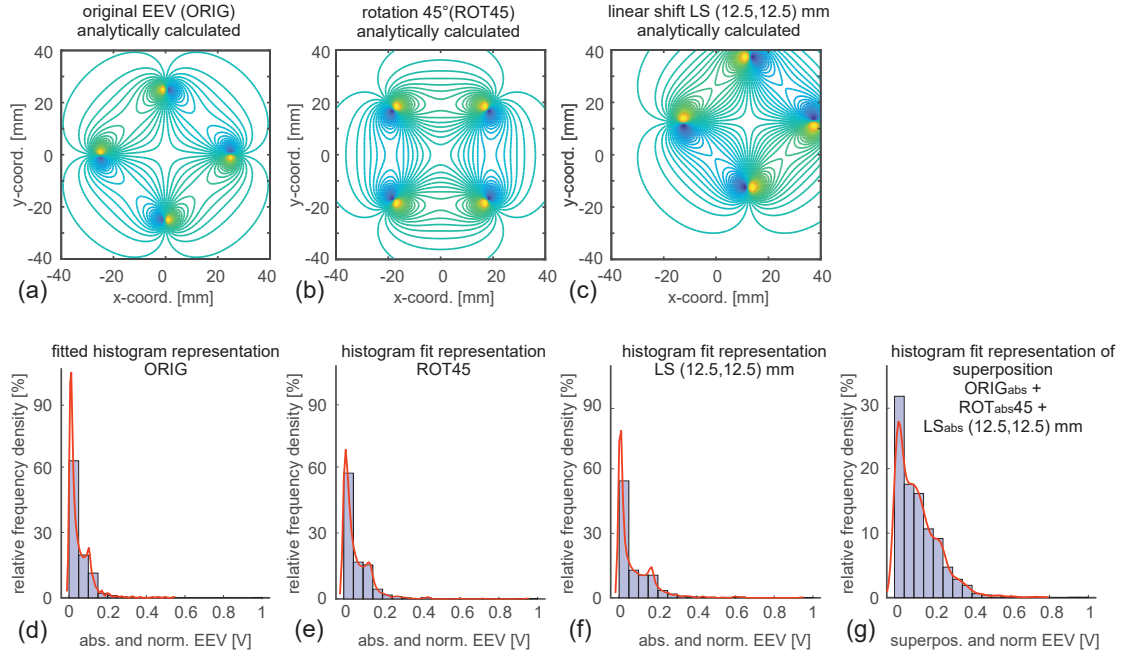
FIGURE 5.3: Histogram fit representation of EEVs based on a kernel density estimation (KDE) to identify an optimal composition of movement sequences. The histogram visualizes the distribution of the potential difference of the EEV. (a) Analytically calculated original EEV (ORIG). (b) Analytically calculated rotated EEV by 45° (ROT45). (c) Analytically calculated EEV, in this case linearly shifted by 12.5 mm both in x- and y-direction (LS (12.5, 12.5) mm). (d) Histogram fit representation of ORIG EEV. For this, the absolute value of the potential difference is used, which is normalized to a value range between 0 and 1. The fit curve shows an overshoot close to the first bins of the histogram which is caused by the KDE. (e) Representation of a fitted histogram of the absolute and normalized ROT45 EEV. (f) Same as in (d) and (e) but for the linearly shifted EEV depicted in (c). (g) Superposition of absolute value matrices $ORIG_{abs}$, $ROT_{abs}45$ and $LS_{abs}(12.5, 12.5)$ mm. Subsequently, the resulting matrix is also normalized to a range between 0 and 1 to allow for a comparison for different movement sequences. The lowest maximum value of the density fit curves of all movement sequences provides the best result.

Several requirements have to be observed in order to execute the strategy. As already used in chapters 3 and 4, the sensor arrangement is assumed to be symmetrical. The sensors and emitters are arranged orthogonally to each other and have the same size. Furthermore, the same potentials are emitted to generate the electric dipole field. This enables to calculate the EEV analytically as in chapter 4.

The general procedure of the histogram fit strategy is structured as follows:

1. Analytical calculation of the individual EEV matrices for each movement condition of the respective sequence: ORIG, ROT, LS

2. Computation of absolute values of the analytically calculated EEV matrices to prevent cancellation of the potential differences during addition: $ORIG_{abs}$, ROT_{abs}, LS_{abs}

3. Superposition of the absolute matrices:
   $RES = ORIG_{abs} + ROT_{abs} + LS_{abs}$

4. Normalization of the resulting matrix RES to a range between 0 and 1 to ensure comparability between different sequences: RES_{norm}

5. Generate histogram representation of the normalized resulting matrix RES_{norm}. The choice of the number of bins is arbitrary. In this case, a fixed number of 20 bins have been chosen

6. Calculation of density fit curve f according to equations (5.2), (5.3) and (5.4), which will also be explained in the current section 5.2

7. Determination of the maximum value of the relative frequency density in the fit curve: $max(f)$

To be able to compare a large number of different sequences with each other, these seven steps of the general procedure have to be performed for each individual sequence s. The lowest maximum value of the relative frequency density in the fit curve of all investigated movement sequences indicates the best result r$_{best}$:

$$\mathrm{r}_{best} = min\left\{max\left(f_s\right)\right\} \qquad s \in \mathbb{N}^+ \tag{5.1}$$

where s is the index of the respective movement sequence.

The density fit curve of the EEV histogram used here is based on the kernel density estimation, which can be defined by a smoothing function and a bandwidth value (Bowman and Azzalini 1997). In contrast to the strategies introduced in chapters 3 and 4, in which the corresponding parameters or a threshold value have to be defined to determine whether an object position can be calculated with sufficient accuracy, the KDE belongs to the non-parametric statistics to estimate the probability density fit curve of random data (Sheskin 2006). The advantage of this is that the model structure is only determined from the data, thus a flexibility is available since just one parameter, the sample size n, has to be defined. The kernel density estimator $\hat{f}$ to obtain the fit curve f is defined as

$$\hat{f}_h(x) = \frac{1}{nh} \sum_{i=1}^{n} K\left(\frac{x - x_i}{h}\right) \tag{5.2}$$

with the bandwidth $h > 0$ and $(x_1, ..., x_n)$ are random samples from the distribution with sample size n. The kernel K is represented by a non-negative function. There are various choices of kernels (Hill 1985), in this case a *Gaussian kernel* is selected:

$$K(u) = \frac{1}{\sqrt{2\pi}} e^{-\frac{1}{2}u^2} \tag{5.3}$$

For the quality of density estimation the selection of the kernel is less important than the choice of the bandwidth value h which controls the smoothness of the resulting density fit curve. The approach used here to calculate the optimal bandwidth for random samples of normally distributed one dimensional data with Gaussian kernel is *Silverman's rule-of-thumb* (B. W. Silverman 1986) which is given by

$$h = \left(\frac{4\sigma}{3n} \right)^{\frac{1}{5}} \tag{5.4}$$

where σ is the standard deviation of the samples. The kernel density is evaluated with a sample of 100 equally arranged points which cover the range of data.

5.3   Results of the fitted histogram representation of EEVs

In contrast to the investigations performed in chapters 3 and 4, the histogram fit representation allows to compare a significantly larger number of permutations concerning the uniqueness of object localizations. In chapter 4 a variety of linear shift movements is investigated and compared, but the rotational movement has been fixed to 45° since this value is essential for the partitioning of the search area. Using the histogram fit strategy, it is possible to examine sequences from a large number of rotational movements combined with numerous linear shifts and the original matrix to compare their uniqueness with respect to object localization. Here, all cases of ROT-conditions (ROT (0...90) °) in combination with the cases of LS-conditions (LS (0...25, 0...25) mm) and the ORIG-condition are explored. The resulting number of permutations is 61516. After applying the general procedure for each of these sequences, the maximum value of the fitted curve is determined and stored in a matrix. According to equation (5.1), the best result of all observed sequences can be found. In table 5.1, the best result is given in the first row. In addition, the ranking of the five best scores is depicted in the following four rows. The respective combinations of the movement sequence is also shown. The relative frequency density indicates the identified maximum value of the density fit curve. The results in the ranking list are only composed of discrete values of the respective movement conditions.

ranking of best scores	combination of movement sequence			relative frequency density
	ROT	LS$_x$	LS$_y$	
[ranking number]	[degree]	[mm]	[mm]	[%]
1	44	13	13	28.451
2	46	13	13	28.452
3	42	21	4	28.455
4	48	4	21	28.456
5	42	22	3	28.466
half sensor length	45	12.5	12.5	28.340
mean (best 10)	45.00	12.70	12.70	28.460
STD (best 10)	3.43	8.85	8.85	0.009
mean (best 100)	45.03	12.99	12.81	28.570
STD (best 100)	2.96	6.93	6.90	0.056
mean (best 500)	44.94	12.66	12.62	28.770
STD (best 500)	4.73	8.17	8.19	0.120

TABLE 5.1: Ranking of best results for combinations of movement sequences by means of the histogram fit strategy. The first part of the table (first five rows) lists the five best identified movement sequences, composed of the original EEV, a rotation and a linear shift. As at first only discrete values were examined, the composition of the original matrix, a rotation by 45° and a shift of exactly half the sensor length (LS(12.5, 12.5) mm) was additionally tested. This result is highlighted by the red rectangle because in this case the relative frequency density shows an improved result compared to the best result of the first five rows. The lower part of the table contains the arithmetic mean for the best 10, 100 and 500 results and the corresponding standard deviation (STD). Regarding the rotational movement, a rather constant mean value of 45 ° with a slight deviation can be identified for all cases. However, the linear shift movement differs greatly in its combination, which was also observed in the results of the ranking list.

Since in chapter 4 it was assumed that exactly half the sensor length shift would probably provide the best result, this sequence (here highlighted by a red rectangle) was also tested. In fact, this combination provides the best result. To recognize tendencies indicating optimal movement sequences, the mean value and the standard deviation (STD) of the best 10, 100 and 500 results are additionally calculated and also shown in the table. In all cases, the rotational movement condition exhibits a rather constant mean value of 45 ° with only a slight deviation, whereas the linear shift movement condition shows significant deviations with respect to the mean.

To visualize the best 500 results and their tendencies, in figure 5.4(a) a 3D-scatter plot of the results and in figure 5.4(b) a 2D-scatter plot for the cut plane at ROT45 is presented. The linear shift movement conditions, both in x- and y-directions are shown on the x-and y-axes. The rotational movement condition is illustrated on the z-axis of the diagram. The ranking of the optimal composition of movement sequences is shown as color-coded markers and the best results are highlighted in blue shades. The diagram illustrates that the results have been grouped into roughly three clusters. Already in table 5.1 it can be observed that the rotational movement of 45° seems to be optimal but the

linear shift movement condition can not only be reduced to one optimal value. The empirically determined result presented in chapter 4 can be identified in the center of the scatter-plot. The shading of blue markers indicates that the best results are concentrated here. However, two additional linear shift conditions are displayed, each predominantly shifting only in one direction.

(a)

(b)
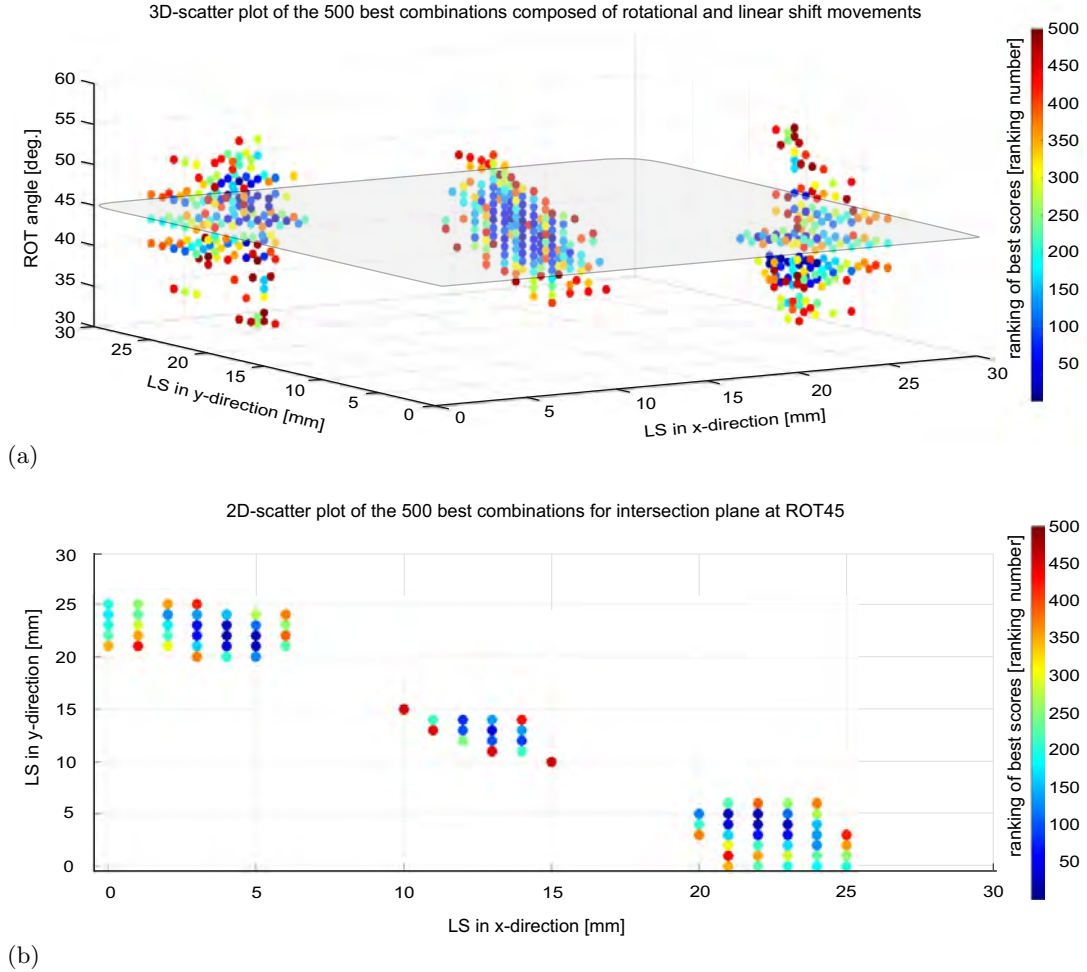
FIGURE 5.4: Visualization of the 500 best combinations of movement sequences by means of the histogram fit strategy. (a) The 3D-scatter plot shows the relationship between the linear shift movements in both x- and y-direction depicted on the x- and y-axes and the rotational operation which can be found on the z-axis of the diagram. All permutations composed of the combination of the original EEV (ORIG), all cases of rotational conditions (ROT(0...90) °) and all cases of linear shift conditions (LS(0...25, 0...25) mm) are explored by means of the histogram fit strategy. To analytically determine the optimal composition of movement sequences, the ranking of the 500 best scores is presented. The ranking is color-coded, the best results are highlighted in blue shades. As a result, three different clusters have emerged. On the one hand the expected result, which was already empirically determined in chapter 4 (half sensor length), can be observed, on the other hand also a linear shift only in one direction appears to provide a suitable result. However, the rotational movement of 45°, previously defined for the method of partitioning of search area, seems to be optimal for all analyzed sequences. (b) 2D-scatter plot of the 500 best combinations illustrated for the intersection plane at ROT45.

103

5.4   Summary

The histogram fit strategy introduced in this chapter, which is based on a kernel density estimation, is easy to implement and requires less computing time compared to the previously introduced strategies. A fitted histogram representation of EEVs is used to estimate an optimal composition of movement sequences. The maximum value of the obtained density fit curve of the EEV histogram provides information about the uniqueness of object localization derived from a composition of movement conditions. Thus, a large number of sequences can be compared with each other and the optimal movement sequence can be identified by the lowest maximum value. Using this strategy, it is possible both to validate the previously empirically determined result obtained in chapter 4, which proposes a linear shift of half a sensor length, and to verify the rotational movement of 45° that is permanently applied in all prior strategies. In addition, the analysis of the scatter plot, shown in figure 5.4, once again confirms the majority voting approach, introduced in chapter 4. A sequence from the ORIG condition, a ROT45 condition and three linear displacements is used here. The first shift is performed exclusively in x-, the second exclusively in y- and the third both in x- and y- direction. The results that can be observed in the scatterplot seem to correspond to this approach.

Furthermore, the histogram fit strategy is not based on defining parameters and the calculation of intersections or the nearness of EEV contour-rings to assess the uniqueness of object localization within a matrix that results from a superposition of different movement conditions.

As in chapters 3 and 4, a symmetrical sensor-emitter arrangement with orthogonally arranged sensor electrodes has been assumed as a precondition for this strategy. When using the symmetrical arrangement, it was possible to compare all permutations with each other by means of the strategy. But also the examination of an unsymmetrical sensor arrangement can be performed using this histogram fit strategy. Since the search for a suitable sensor arrangement leads to a significant number of permutations that have to be compared with each other, the solution can be determined as an optimization problem. The outlook in chapter 6 briefly discusses an approach for the optimization problem of an unsymmetrical sensor arrangement which is based on the histogram fit strategy. As a further step, a cluster analysis may be implemented for evaluation and to quantify the intensity of the linear correlation between the individual results.

6

Discussion and future research

6.1 Discussion

This thesis concentrates on the localization of objects in fluids based on a bioinspired electroreceptor system. The central questions are how many sensors are needed in order to uniquely determine the position of an object and which sensor arrangements and movements are beneficial for this task. The biological model, the weakly electric fishes are able to generate and sense electric fields and use this for active electrolocation. While the sensor-emitter configuration in the biological template is anatomically fixed, discontinuities in the density of electroreceptors have been reportend and have been implicated as morphological adaptations to facilitate sensing (Caputi et al. 2002; von der Emde and S. Schwarz 2002). In addition to these anatomical specializations, fish are known to execute stereotyped scanning behaviors that are believed to provide specific and sometimes new sensory information like size, shape and distance of detected objects (Engelmann and von der Emde 2011; Biswas et al. 2018). Technical abstraction makes it possible not only to investigate the role of different sensor arrays and the contribution of movement, but can further be extended to changes of the emitter configuration, thereby going beyond the biological example.

Previous work has already used bioinspired technologies to develop sensor systems that operate contact-free at short distances. These systems are based on probabilistic (e.g. Bayes filter, Kalman filter, particle filter) approaches (Lebastard et al. 2013; Y. Silverman et al. 2012; Y. Silverman et al. 2013; Solberg et al. 2008). However, before these more complex approaches are adopted or extended, this work takes a step back to optimize the very basic movement strategy of the sensor-emitter ensemble as such. Therefore, all data reported in this thesis is based on a simple biomimetic abstraction for active electrolocation, consisting of an emitter dipole and an orthogonally arranged pair of sensor electrodes. This reduced sensor-emitter array is a simplified abstraction of the

biological electrosensory system of fish. In a first step, this abstraction is used to find an optimal scanning strategy composed of a minimal set of scanning movements of this receptor system to uniquely identify the position of an object. For this, the approach of EEVs, a concept originally introduced by Solberg et al. (2008), was used in this thesis. This concept is connected with the idea that optimal movements (optimal scanning strategy) of the sensor-emitter ensemble can further facilitate object localization.

Based on the superposition of numerical extracted contour-rings of linearly shifted and/or rotated EEVs, the number of possible object positions is reduced to the intersections of these rings. This allows to localize the object provided that a sufficient number of movements and local measurements are performed in sequence. Contrary to using exclusively translational movements as in Solberg et al. (2008), this work shows by inclusion of rotational movements that a minimal set of scanning movements suffices to uniquely localize an object. Rather than using a particle filter approach, the strategy introduced here is based solely on the superposition of extracted EEV contour-rings as determined by potential measurements at the sensors. When a concatenation of purely rotational movements is used, the mirror symmetries of the superimposed EEV contour-rings result in a reduction of uncertainty with respect to the object position in 2 possible (mirror symmetric) positions. In contrast to this, a concatenation of purely translational shifts can result in potentially unambiguous results. However, for a limited amount of movements and measurements the highest percentage of unique object positions have been identified by using a concatenation of the original EEV (ORIG), a rotated EEV (ROT) and a linearly shifted EEV (LS). In a first step, for this minimal set of scanning movements, the electric field characteristics and the respective EEVs were modelled and simulated by means of FEM. This allows a simple optimization of this very basic scanning strategy, which then can be used as a pre-processing step for more complex and higher-level process approaches, e.g. particle filters.

Thereafter, as an extension of these results, a strategy was developed that has the potential to be used in robotic applications. This approach is based on the minimal set of scanning movements (see above). As a first step only two movements (ORIG + ROT45) are used to reduce the search area by using a skillful partitioning approach. In contrast to the first approach that relies on computationally intensive FEM-simulations, the EEVs are calculated by a simplified analytical formulation which is based on mathematical assumptions presented in Rasnow (1996) that enable the description of the perturbations caused by a sphere in an uniform electric field. Such an analytical approach offers the advantage that it can be implemented on embedded computer systems.

A further improvement to the initial approach is a modification of the optimal scanning strategy. In contrast to the use of precise intersections, also the nearness of contour-rings,

chosen from a composition for each movement condition, provided sufficient information to identify the position of an object. The recently introduced localization algorithms (basic movement sequence and majority voting approach) are based on this nearness metric which makes them less sensitive to measurement inaccuracies or unwanted discretization effects. As a result, this increases the number of unique object positions. These localization algorithms, applicable in embedded systems, are independent of probabilistic models and only dependent on direct sensor readings and on a technological measuring system to record the movement of the simple receptor system. In contrast, Solberg et al. (2008) has chosen a particle filter approach in which each possible object position is represented by discrete particles with likelihood weightings. Subsequently, the expected variance of particles has to be minimized which allows the controller continuously to predict and update this probability to make a hypothesis of where the object can be located. Based on a particle filter algorithm, a typical electrolocation sequence starts with an initial assumption, followed by a series of observations that cause defined movements of the sensor-emitter system. The robot stops when a localization criterion is satisfied, e.g. when the uncertainty is below a threshold value. As an advancement of the electrolocation sequence used by Solberg et al. (2008), in which only linear shift movements were performed, the beneficial influence of rotational movements on the results was demonstrated in this work. In addition, it was shown that a minimal and fixed movement sequence is sufficient to uniquely localize an object.

The majority voting approach introduced in this thesis is based on an original EEV (ORIG), a fixed rotational movement by 45°(ROT45) and a triple combinations composed of a pure x-, a pure y- and a diagonally-directed linear shift (LS1-LS3). For this configuration, the best combination of linear shifts is represented by shifting the receptor system by a value of approximately half distance between the sensors and the center of the sensor-emitter ensemble. This is caused by the general shape of the EEV. Its base region exhibits a range of about $0\,V$, in consequence the length of the extracted contour-rings is large which results in a high number of possible object positions. In addition, this region shows a small gradient which can lead to large deviations in case of measurement inaccuracies. However, higher level regions of the EEV offer the advantage of smaller contour-ring lengths and larger gradients which results in a reduced number of possible object positions and minor effects caused by deviations. In conclusion, it is advantageous to use a combination of EEV contour-rings that include a large number of extracted contour-rings from higher-level regions of the EEVs.

These reflections about the general shape of an EEV and its influence on measurements have led to the question of whether a rotational movement different to 45° could also provide the same or even better results in uniquely identifying an object. By means of the majority voting approach, the use of a fixed rotational movement (ROT45) is justified by

the fact that a maximal reduction of the search area (search area partitioning) is achieved. This fixed ROT45 movement enables the complete investigation of exclusively linear shifts because the number of permutations to be tested are kept on a manageable level. However, if all rotations have to be examined as well in this study, it is an advantage not to analyze each discrete point within the search matrix, but the totality of the points contained in the EEV matrix has to be examined for uniqueness. For that reason, a fitted histogram representation is introduced to compare a large number of different movement sequences. Based on a kernel density estimation, a histogram fit strategy is used, in which the lowest maximum value of the obtained density fit curve is to be identified, which indicates the best sequence out of a large number of movement sequences. The concept of this strategy is based on considerations of the basic shape of the EEV. It plays a major role in estimating an optimal composition of movement sequences. An advantage of this histogram fit strategy is that it is easy to implement and that it requires less computing time compared to the localization strategies presented previously. Thus, this strategy could also act as a pre-processing tool for more complex and high-level approaches.

6.2 Future research

This section contains recommendations for future work and possible practical implementations of the object localization strategies and of the application presented in this thesis. Initially, the focus of the study was on a symmetrical sensor arrangement of the receptor system. However, the question arises whether a different sensor arrangement provides better results for the localization of objects by generating EEVs which possibly provide higher potential differences or gradients in acceptable ranges in the distance to the sensors. Figure 6.1 illustrates three different examples of unsymmetrical or compressed sensor arrangements on a planar unperturbed electric field. In all examples, the emitters are kept in their original position (E+ = (-25, 0) mm and E- = (25, 0) mm) which allows a simple analytical calculation of the EEVs. Figure 6.1(a) shows an arrangement similar to the symmetrical receptor system, which has already been used and investigated. Again, in the unperturbed case, the sensors are positioned on the 0 V equipotential line between the emitters, but are closer to each other. Figure 6.1(b) illustrates sensors that are placed on equipotential lines of the same potential but of opposing sign. Therefore, in the unperturbed case, the potential difference, measured at the sensors, is always unequal to 0 V. The third example in figure 6.1(c) show sensors which are located on the same equipotential line but different to 0 V. If there is no object present in the field, the potential difference measured at the sensors is always 0 V.
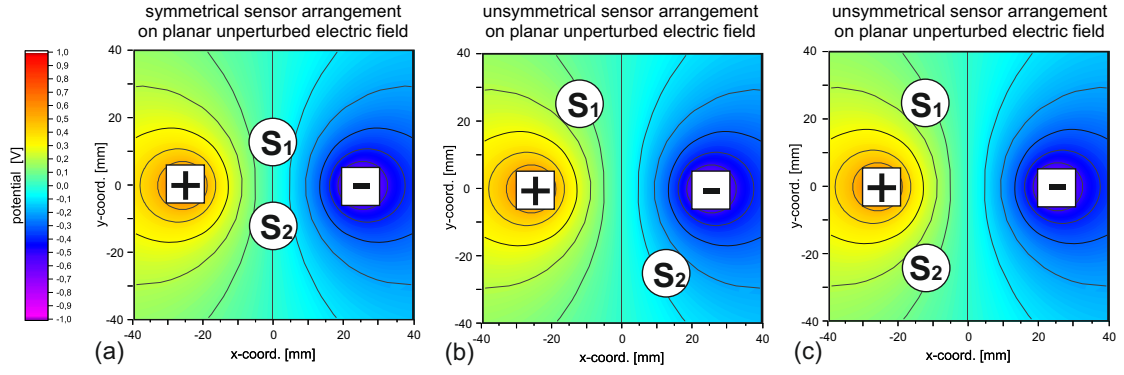
FIGURE 6.1: Different sensor arrangements on a planar unperturbed electric field. In all cases, the emitters (labelled + and -) are located at original position, but the sensors S_1 and S_2 are arranged differently. (a) Symmetrical sensor arrangement for $S_1 = (0, 12.5)$ mm and $S_2 = (0, \text{-}12.5)$ mm. The sensors are located on the equipotential line centered between the two emitters. Similar to the symmetrical arrangement always used as simple biomimetic abstraction, in the unperturbed case, a potential of 0 V can be measured here, but in contrast the sensors are closer to each other. (b) Here, the sensors are placed at positions $S_1 = (\text{-}12.5, 25)$ mm and $S_2 = (12.5, \text{-}25)$ mm. They are located on equipotential lines which exhibit the same potential but different signs. (c) In this configuration, the sensors are placed at $S_1 = (\text{-}12.5, 25)$ mm and $S_2 = (\text{-}12.5, \text{-}25)$ mm. In the unperturbed case, the sensors are positioned on an equipotential line having a potential difference of 0 V.

Based on the unsymmetrical or compressed configurations presented in Figure 6.1, it is possible to generate EEVs as illustratec in figure 6.2 as 2D- and 3D-plots. These EEVs are created by means of FEM-simulations. In general, it should be mentioned that the shape of the EEVs can be modified by using an unsymmetrical or changed sensor arrangement. The EEVs depicted in figures 6.2(a) and (b) exhibits a symmetrical range of the potential difference, even if the contour-rings are partially compressed. If the distance of the sensors to is larger than the distance of the emitters to the center of the arrangement, it is also possible to generate stretched EEV contour-rings. Figures 6.2(c) and (d) illustrate an unsymmetrical EEV in which also partially compressed contour-rings can be observed. However, compared to the EEV presented in (a) and (b), a positive offset in the range of the potential difference is present. The unsymmetrical EEV shown in figures 6.2(e) and (f) differs from the previous EEV by having no offset, however the contour-rings change their symmetry characteristics. In addition, this arrangement enables to generate higher potential differences. In summary, it could be a future strategy to use stretched or compressed EEV contour-rings to on the one hand break the symmetry and on the other hand to keep the sensors on equipotential lines of 0 V in the unperturbed case, to avoid an offset.

Thus, the question arises where exactly the sensors have to be positioned to achieve the best localization of objects. The number of permutations is too large to investigate and compare all cases. For this reason, an optimization procedure based on a *genetic*
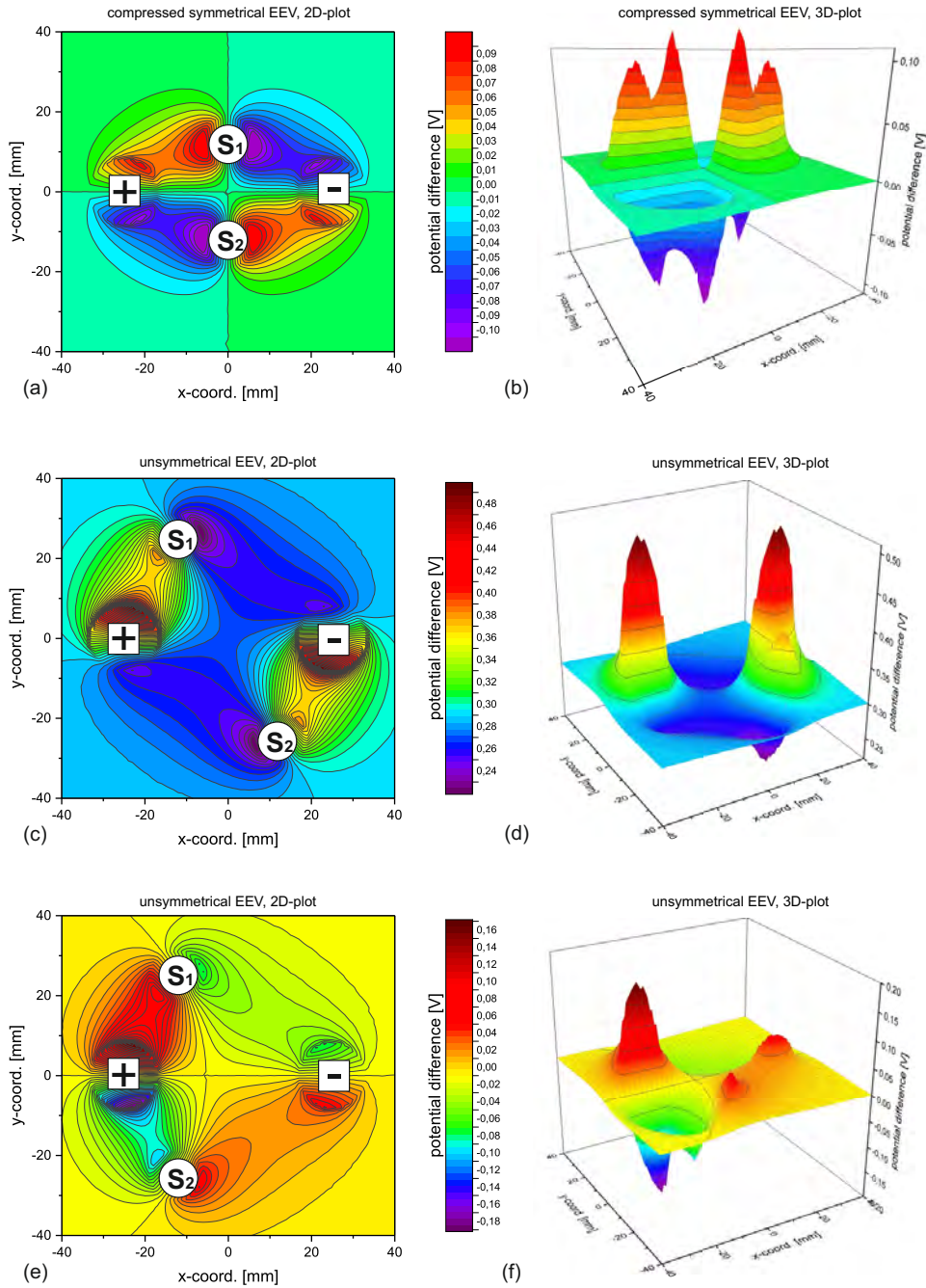
FIGURE 6.2: Comparison of different unsymmetrical or compressed EEVs, visualized as 2D- and 3D-plots. The labels of the figures correspond to the respective sensor arrangement shown in figure 6.1. (a) 2D-plot of symmetrical EEV for sensor arrangement also illustrated in figure 6.1(a). (b) 3D-plot of symmetrical EEV as shown in (a). The range of the potential difference is symmetrical, even if the EEV contour-rings are partially compressed. (c) 2D-plot of the EEV for sensors for the arrangement presented in figure 6.1(b). (d) 3D-plot with regard to (c). This arrangement causes a positive offset in the range of the potential difference and partially compressed contour-rings. (e) Here, the sensors are located at positions as shown in figure 6.1(c). (f) 3D-plot of unsymmetrical EEV as depicted in (e). Here again, the range of the potential difference is symmetric, but the EEV contour-rings change in their symmetry characteristics.

algorithm (GA) is used as part of the histogram fit strategy to determine an optimal sensor arrangement even in unsymmetrical scenarios. Figure 6.3 provides an explorative example of a histogram fit representation of unsymmetrical EEVs after using an optimization procedure by means of a genetic algorithm.
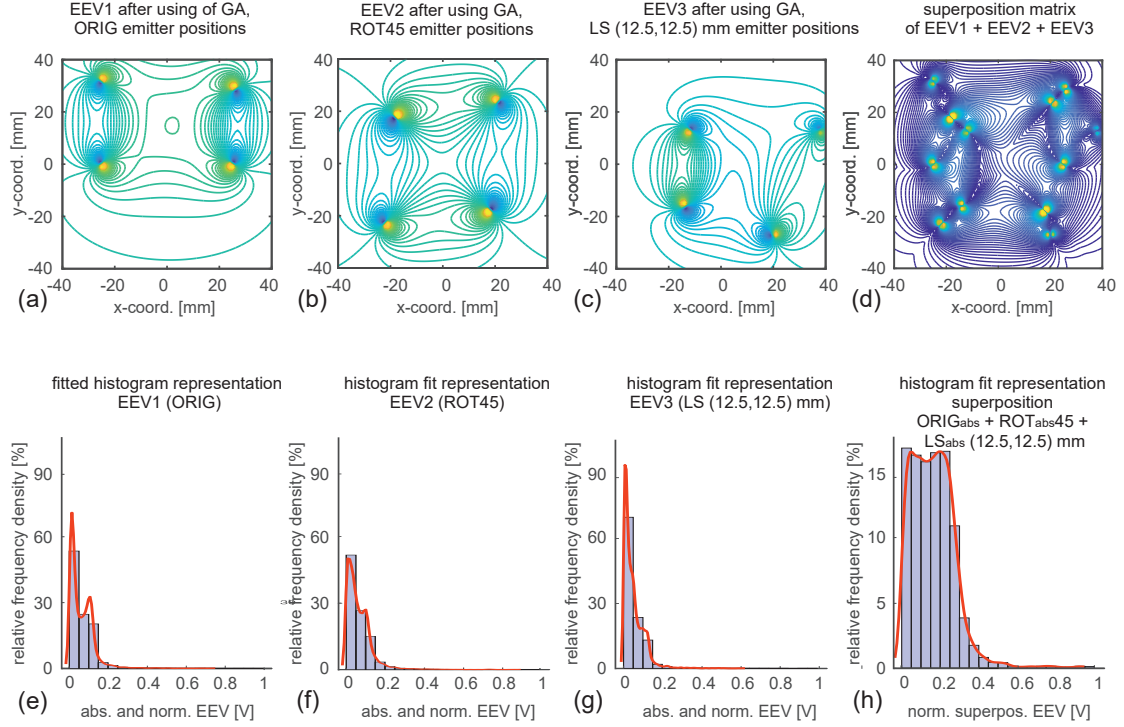

FIGURE 6.3: Fitted histogram representation of unsymmetrical EEVs after optimization by means of a genetic algorithm. An optimal arrangement of the sensors is investigated by means of the histogram fit strategy in order to identify optimized compositions of movement sequences. In this arrangement the positions of the sensors S_1 and S_2 are variable, the locations of the emitters remain fixed in relation to each other and to the origin, but under consideration of a rotational or a linear shift movement. This enables the simplified analytical calculation of the EEVs. (a) EEV1 as a result of optimized sensor positions for the emitters at ORIG position. (b) The emitters are rotated by 45° (ROT45), the distribution after optimization of the sensors results in EEV2. This result shows similarities compared to the symmetrical sensor arrangement. (c) Result of EEV3 after using the genetic algorithm. Here, the emitters are linearly shifted by 12.5 mm both in x- and y-direction (LS (12.5, 12.5) mm). (d) Superposition matrix of EEVs shown in (a)-(c). It can be observed that almost the entire area is filled up primarily by small contour-rings. (e) Histogram fit representation of ORIG EEV1 shown in (a). (f) Fitted histogram representation of the optimized EEV2 for emitters at ROT45 with regard to (b). (g) Same as in (e) and (f) but for EEV3 depicted in (c). (h) Histogram fit representation of superposition of absolute value matrices $ORIG_{abs}$ (EEV1), $ROT_{abs}45$ (EEV2) and $LS_{abs}(12.5, 12.5)$ mm (EEV3). Compared to the best result of the symmetrical arrangement presented in chapter 5, a more uniform distribution can be observed below the fit curve. However, this effect is a consequence of the influences caused by offsets.

Genetic algorithms are a specific form of evolutionary algorithms, which use the natural selection process of biological evolution in their functionality to solve optimization problems (Holland 1992). However, in most cases it is not possible to find the global

but a sufficiently precise local solution (here the minimum) of the optimization problem. As part of the genetic algorithm, a population consisting of individual solutions will be repeatedly modified. By applying operators, such as recombination and mutation, over successive generations the population tends towards the minimal solution. By means of the histogram fit strategy, the genetic algorithm aims to find the minimum of the maximum value of the obtained density fit curve. This requires the adaptation of GA parameters such as population size, number of generations and the definition of bounds to determine an optimal solution. The result in figure 6.3 is based on a population size of 200 individuals and a number of 300 generations. The sensors are arbitrarily placed on discrete points by integer constraints within the bounds of the search area, whereas the emitters always remain fixed in their position relative to the origin under consideration of any possible rotational movements or linear shifts. In this first approach, the emitter configuration is unchanged in consideration of the basic movement sequence composed of ORIG (figure 6.3(a) and (e)), ROT45 (figure 6.3(b) and (f)) and LS $(12.5, 12.5)\,\text{mm}$ (figure 6.3(c) and (g)) to optimize the positions of the sensors in the rotated or linearly shifted ensemble. The superposition matrix of the individual EEVs as a result of the optimization process can be seen in figure 6.3(d). A variety of small EEV contour-rings can be observed which cover the entire search area. This uniform distribution of the result can also be recognized below the density fit curve presented in figure 6.3(h). Since it is difficult to deal with objects that are far away from the receptor system, many areas with large field strengths and consequently also large gradients are advantageous because they reduce the number of possible object positions. In comparison to the best result of the symmetrical sensor arrangement, it seems that a better result has been found due to optimization. However, by examining this result for uniqueness by means of the basic movement sequence for each position in the matrix, it turns out that this it is not the case. This is caused by the influences of offsets as presented in figure 6.2(c) and (d). Nevertheless, from a measurement point of view, such a result could potentially be advantageous as the measurements can be carried out in higher ranges of potential differences by means of smaller EEV contour-rings, which exhibit larger gradients. Furthermore, it could be useful to eliminate possible offsets by suitable methods to minimize their influence when applying the histogram fit strategy.

A further opportunity for future work to improve and optimize the developed localization strategies can be found in a three-dimensional simulation, which is inspired by the general shape of the biological model. All investigations in this work have been carried out using two-dimensional simplified assumptions without sensor bodies. However, it would be possible to realize the movement of the receptor system in a technological implementation by a defined arrangement of sensors only by switching between the different sensor pairs. A selection of the corresponding electrodes of an array could be performed by

using controlled analog multiplexers (Böckmann 2017). However, this would require the appropriate design of a sensor pod.

Currently, there is a variety of physical models for the design, construction and control of bioinspired and biomimetic underwater vehicles (Neveln et al. 2013). Different robot applications were developed in order to investigate localization strategies for 3D-objects. For example, Boyer et al. (2012) use a current sensing approach in a sensor system consisting of seven electrodes to measure the current that flows through the electrodes. Another electrosensory application, based on a voltage sensing approach, is shown in Bai et al. (2015), where a cylindrical shaped sensor pod, which contains two emitter electrodes and multiple pairs of differential sensing electrodes, is used to measure the potential difference for the detection of perturbations to the self generated electric field. Thus, the sensor geometry plays an important role in the development of applicable receptor systems.

In order to provide a complex 3D-distribution of sensor points, a 3D-model of a fish shape might serve as a template to define a bioinspired distribution of technical electro-sensors. As an example, a simplified geometry based on the biological model of weakly electric fish, which can be used for 3D-field simulations is shown in figure 6.4(a). The fish geometry is simplified to reduce the model to the essential features, which enables the simulation to operate more efficiently. In figure 6.4(b), a mesh generation of the simplified geometry in preparation for numerical simulations is illustrated. A result of first 3D-simulations of the electric field based on the simplified fish model is presented in figure 6.4(c). In this case, the field is not perturbed by objects.

simplified fish geometry used in simulation   generated mesh of simplified fish geometry   3D field simulation based on simplified fish model

(a)   (b)   (c)
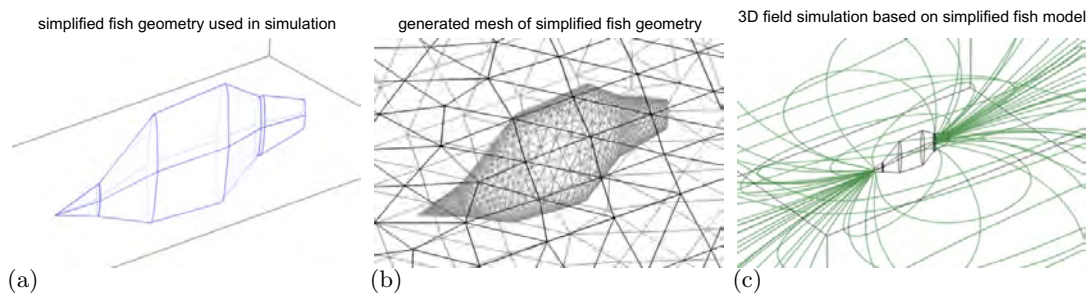
FIGURE 6.4: 3D-field simulation based on biological model using a simplified fish geometry. (a) Simplified 3D-fish geometry used in FEM-simulation. Model simplifications reduce the model to the essential features enabling the simulation to operate more efficiently. (b) Mesh generation of the simplified fish model to subdivide the continuous area into discrete sections in preparation for numerical simulations. (c) First 3D-field simulation results based on biological model (simplified geometry) without object. Based on this model, further abstractions can be derived for the development of the arrangement of sensors and emitters which could be attached to a body of an underwater vehicle.

This model could not only be used to develop the design of the artificial electrosensory system, further questions with respect to the biological system could also be investigated. With regard to the shape and frequency of the EOD signal emitted by the fish, time-dependent simulations with dynamic signals could be helpful to determine an optimal signal shape. In addition, the determination of the phase shift of the signals could be useful to detect further object parameters (Ammari et al. 2014; Bai et al. 2015; Bai et al. 2016). First approaches for the development of a signal processing system suitable to implement in a technical system have already been investigated in Eickmann (2015).

This work was focused on the localization of a single spherical object. The disadvantage of the strategies developed here is that the parameters of the object and the fluid, such as the permittivity, conductivity and the size of the object have to be known to be able to uniquely localize an object. Therefore, further investigations should be carried out concerning the influence of these parameters or to what extent a larger number of objects or a different shape or size of an object influence the localization strategies introduced here. It may be advantageous to supplement additional methods based on probabilistic approaches in order to uniquely identify further characteristics such as shape, material properties, size or number of objects.

Furthermore, inspired by the scanning movements of the fish, the dynamic behavior of the receptor system was investigated. A minimal set of scanning movements has been determined to be sufficient to perform an unique object localization. However, the fish also change their body shape relative to the object (Sim and Kim 2011). Further research could be carried out to determine whether this behavior would provide a gain in information if it is transferred to the sensor system.

Technical implementations of the localization strategies and the application which were developed in this thesis might be found in mobile underwater robotics, medical technology, in the determination of material properties of liquids or objects, or in environments where optical systems might fail, for example when inspecting fluid-filled drains. A similar approach was used to investigate a catheter-based sensor for the medical diagnosis of arteriosclerosis which is intended to identify plaques (Metzen et al. 2012). A further example in which the detection of an emitted field is applied is the electrical impedance tomography (EIT) (Barber and Brown 1984). EIT is based on measurements of electrical conductivities within a body and is used in medical imaging. By emitting weak alternating currents and sensing potential differences at the surface of the examined body region, EIT is used to estimate the distribution of impedances to generate images of the structures of the biological tissue within the body. In Snyder et al. (2012) the possibility of using EIT also for active electrolocation in fluids has been explored.

To conclude, it can be summarized that the original research question, which was initially focused on active electrolocation of objects can be extended by many aspects. The continuous optimization of the design and the movement conditions of the bioinspired electroreceptor system has played an major role in the development and investigation of suitable strategies for object localization. To find an optimal scanning strategy, which should be composed of a minimal set of movements, numerical methods were initially used. In principle, the developed strategy is based on the superposition of extracted linearly shifted and/or rotated EEV contour-rings, which intersections reduce the number of possible object positions. To implement this scanning strategy on embedded systems, two localization algorithms were introduced which are based on a simplified analytical EEV representation and an improvement of the intersection strategy by investigating the nearness of the contour-rings. In the last step, a fitted histogram representation was introduced to estimate the optimal composition of movement sequences.

The scanning, localization and evaluation strategies developed in this thesis may provide useful answers to future research questions in the field of active electrolocation.

Appendix A

A.1 Abstraction of the emitter arrangement for calculating equipotential lines by means of Apollonian circles

According to section 4.1.1, the arrangement to be considered assumes that the electric dipole field as shown in figure A.1(a) is caused by two parallel conducting cylinders of infinite lengths. A 3D-plot of this arrangement is visualized in figure A.1(b). The cylinders with the corresponding and opposing line charge densities $\pm\lambda$ (here highlighted in blue) are located in a homogeneous medium. In figure A.1(c), an abstraction of the emitter-electrodes is presented by means of a vector representation with reference to the equations used in this appendix. Both emitter cylinders exhibit the same radius R with center points arranged at a distance of 2d apart. The corresponding line charge densities are at a distance of 2b from each other.

The two parallel conducting cylinders generate equipotential lines in a plane perpendicular to the line charges which are represented by the the so-called *Apollonian circles* (Altshiller 1915). The geometric construct of these circles are named after the ancient geometer and astronomer Apollonius of Perga. This construct is useful for calculating equipotential lines of electric fields. Based on the conditions of the vector representation illustrated in figure A.1(c), correlations of the radii R and the center positions d of the circles are calculated as functions of the distance b in the following.

The line charge densities $\pm\lambda$ of the emitters are located at positions $\vec{x}_p = (-b, 0)$ and $\vec{x}_n = (b, 0)$. Furthermore, the distance vectors $\vec{r}_p$ and $\vec{r}_n$ between position $\vec{x}$ and the electrically charged conductors are defined as:
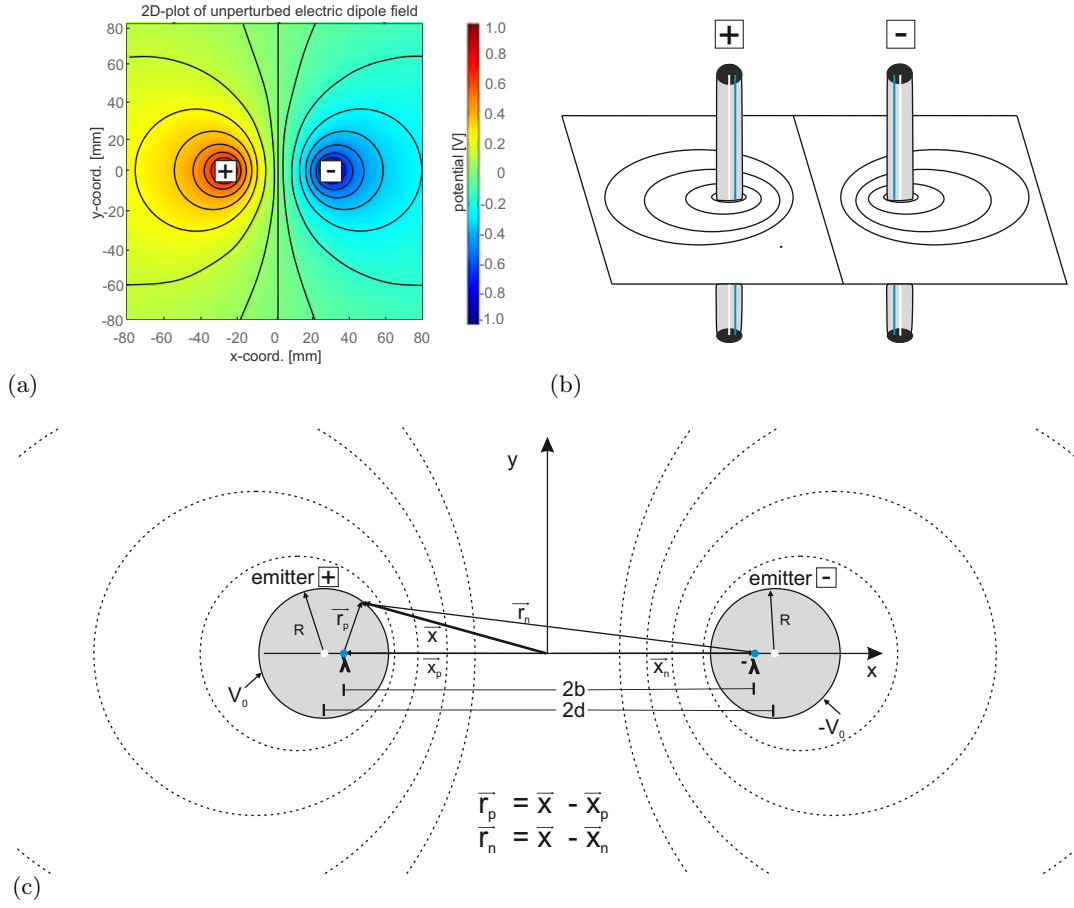
FIGURE A.1: 2D- and 3D-abstraction of the emitter arrangement consisting of two cylinders with corresponding vector representation. (a) 2D-plot of an unperturbed electric dipole field, which is generated by a pair of emitter electrodes (labelled + and -). The equipotential lines are depicted in black. (b) 3D-plot of the electric dipole field, caused by two parallel conducting cylinders which represent the emitter-electrodes. The centers of the cylinders are marked in white, the corresponding line charges are indicated in blue. The equipotential lines of this arrangement in a plane perpendicular to the line charges are represented by the so-called *Apollonian circles*. (c) Vector representation of the emitter-arrangement with reference to the equations used in this appendix. All drawings are not to scale.

$$\vec{r}_p = \vec{x} - \vec{x}_p \quad \Rightarrow \quad r_p = \sqrt{(x + b)^2 + y^2} \tag{A.1}$$

$$\vec{r}_n = \vec{x} - \vec{x}_n \quad \Rightarrow \quad r_n = \sqrt{(x - b)^2 + y^2} \tag{A.2}$$

According to equation (4.7) the potential φ at point $\vec{x}$ is given as:

$$\varphi(\vec{x}) = \frac{\lambda}{2\pi\epsilon} ln\left(\frac{r_n}{r_p}\right) = \frac{\lambda}{4\pi\epsilon} ln\left(\frac{(x - b)^2 + y^2}{(x + b)^2 + y^2}\right) \tag{A.3}$$

A.1. *Abstraction of the emitter arrangement for calculating equipotential lines by means of Apollonian circles*

Transformation of equation (A.3) results in

$$e^{\frac{\varphi(\vec{x})4\pi\epsilon}{\lambda}} = \frac{(x-b)^2 + y^2}{(x+b)^2 + y^2} = k \tag{A.4}$$

where k is a constant ratio of the radii r_n and r_p which results in an Apollonian circle for the geometric location of the point.

$$k = \frac{x^2 - 2xb + b^2 + y^2}{x^2 + 2xb + b^2 + y^2} = \text{const.} \tag{A.5}$$

Rewriting equation (A.5) results in:

$$x^2 + y^2 - 2xb\frac{1+k}{1-k} + b^2 = 0 \tag{A.6}$$

The equation of a circle with center at $(d, 0)$ is

$$(x-d)^2 + y^2 = R^2 \quad \text{or} \quad x^2 + y^2 - 2xd + d^2 = R \tag{A.7}$$

Comparing equations (A.6) and (A.7) leads to equipotential lines, represented by circles with following conditions

$$d = b\left(\frac{1+k}{1-k}\right) \tag{A.8}$$

and

$$b^2 = d^2 - R^2 \tag{A.9}$$

which is already given in equation (4.1). Substituting equation (A.8) in (A.9) results in

$$R^2 = \left(b^2\frac{(1+k)^2}{(1-k)^2}\right) - b^2 = b^2\left(\frac{(1+k)^2 - (1-k)^2}{(1-k)^2}\right) = b^2\left(\frac{4k}{(1-k)^2}\right) \tag{A.10}$$

Finally, for the radii R of the equipotential lines the following correlation is obtained:

$$R = \frac{2b\sqrt{k}}{|1-k|} \tag{A.11}$$

119

Bibliography

Altshiller, N. (1915). "On the Circles of Apollonius". In: *The American Mathematical Monthly* 22.9, pp. 304–305 (cit. on p. 117).

Ammari, H., Boulier, T., and Garnier, J. (2013). "Modeling Active Electrolocation in Weakly Electric Fish". In: *Siam Journal on Imaging Sciences* 6.1, pp. 285–321 (cit. on pp. 10, 62).

Ammari, H., Boulier, T., Garnier, J., and Wang, H. (2014). "Shape recognition and classification in electro-sensing". In: *Proceedings of the National Academy of Sciences* 111.32, pp. 11652–11657 (cit. on pp. 9, 58, 114).

Babineau, D., Longtin, A., and Lewis, J. E. (2006). "Modeling the electric field of weakly electric fish". In: *Journal of Experimental Biology* 209.18, pp. 3636–3651 (cit. on p. 24).

Bacelo, J., Engelmann, J., Hollmann, M., von der Emde, G., and Grant, K. (2008). "Functional foveae in an electrosensory system". In: *The Journal of comparative neurology* 511.3, pp. 342–359 (cit. on pp. 4, 5).

Bacher, M. (1983). "A new method for the simulation of electric fields, generated by electric fish, and their distorsions by objects". In: *Biological Cybernetics* 47.1, pp. 51–58 (cit. on p. 10).

Bai, Y., Neveln, I., Peshkin, M., and MacIver, M. A. (2016). "Enhanced detection performance in electrosense through capacitive sensing". In: *Bioinspiration & Biomimetics* 11.5, p. 055001 (cit. on pp. 10, 62, 114).

Bai, Y., Snyder, J. B., Peshkin, M., and MacIver, M. A. (2015). "Finding and identifying simple objects underwater with active electrosense". In: *The International Journal of Robotics Research* 34.10, pp. 1255–1277 (cit. on pp. 10, 62, 66, 113, 114).

Barber, D. C. and Brown, B. H. (1984). "Applied potential tomography". In: *Journal of Physics E: Scientific Instruments* 17.3, pp. 723–733 (cit. on p. 114).

Bass, A. H. and Hopkins, C. D. (1983). "Hormonal control of sexual differentiation: changes in electric organ discharge waveform". In: *Science* 220, pp. 971–974 (cit. on p. 3).

— (1985). "Hormonal control of sex differences in the electric organ discharge (EOD) of mormyrid fishes". In: *Journal of Comparative Physiology* A.156, pp. 587–604 (cit. on p. 4).

Bazeille, S., Lebastard, V., and Boyer, F. (2018). "Underwater Robots Equipped with Artificial Electric Sense for the Exploration of Unconventional Aquatic Niches". In: *Marine Robotics and Applications.* Ed. by L. Jaulin, A. Caiti, M. Carreras, V. Creuze, F. Plumet, B. Zerr, and A. Billon-Coat. Springer International Publishing, pp. 29–50 (cit. on pp. 10, 72).

Bell, C. C. (1982). "Properties of a modifiable efference copy in an electric fish". In: *Journal of Neurophysiology* 47.6, pp. 1043–1056 (cit. on p. 6).

— (1990). "Mormyromast electroreceptor organs and their afferent fibers in mormyrid fish. III. Physiological differences between two morphological types of fibers". In: *Journal of Neurophysiology* 63.2, pp. 319–332 (cit. on p. 3).

Bell, C. C., Bradbury, J., and Russell, C. J. (1976). "The electric organ of a mormyrid as a current and voltage source". In: *Journal of Comparative Physiology* 110, pp. 65–88 (cit. on p. 3).

Bell, C. C. and Grant, K. (1992). "Sensory processing and corollary discharge effects in mormyromast regions of mormyrid electrosensory lobe. II. Cell types and corollary discharge plasticity". In: *Journal of Neurophysiology* 68.3, pp. 859–875 (cit. on p. 6).

Bell, C. C., Grant, K., and Serrier, J. (1992). "Sensory processing and corollary discharge effects in the mormyromast regions of the mormyrid electrosensory lobe. I. Field potentials, cellular activity in associated structures". In: *Journal of Neurophysiology* 68.3, pp. 843–858 (cit. on p. 6).

Bell, C. C., Zakon, H. H., and Finger, T. E. (1989). "Mormyromast electroreceptor organs and their afferent fibers in mormyrid fish: I. Morphology". In: *The Journal of comparative neurology* 286.3, pp. 391–407 (cit. on p. 5).

Bennett, A. T. D. (1996). "Do animals have cognitive maps?" In: *Journal of Experimental Biology* 199, pp. 219–224 (cit. on p. 9).

Bennett, M. V. L. (1971). "Electroreception". In: *Sensory Systems and Electric Organs*. Ed. by W. S. Hoar and D. J. Randall. Vol. 5. Fish Physiology. Academic Press, pp. 493–574 (cit. on p. 2).

Bennett, M. V. L. and Steinbach, A. B. (1969). "Influence of electric organ control system on electrosensory afferent pathways in mormyrids". In: *Neurobiology of Cerebellar Evolution and Development*. Ed. by R. Llinas. Chicago: American Medical Association, pp. 207–214 (cit. on p. 5).

Binns, K. J., Lawrenson, P. J., and Trowbridge, C. W. (1993). *The Analytical and Numerical Solution of Electric and Magnetic Fields*. New York: Wiley, J. (cit. on p. 13).

Biswas, D., Arend, L. A., Stamper, S. A., Vágvölgyi, B. P., Fortune, E. S., and Cowan, N. J. (2018). "Closed-Loop Control of Active Sensing Movements Regulates Sensory Slip". In: *Current Biology* 28.24, pp. 4029–4036 (cit. on p. 105).

Böckmann, J. (2017). "Hardwaresynthese eines FFT-Algorithmus samt Fensterung zur schnellen Verarbeitung von frei wählbaren, differentiellen Messdaten aus Analogmultiplexern". MA thesis. Bielefeld University of Applied Sciences, Germany (cit. on p. 113).

Bowman, A. W. and Azzalini, A. (1997). *Applied Smoothing Techniques for Data Analysis*. New York: Oxford University Press Inc. (cit. on p. 100).

Boyer, F., Gossiaux, P. B., Jawad, B., Lebastard, V., and Porez, M. (2012). "Model for a Sensor Inspired by Electric Fish". In: *IEEE Transactions on Robotics* 28.2, pp. 492–505 (cit. on pp. 10, 62, 66, 113).

Boyer, F., Lebastard, V., Chevallereau, C., Mintchev, S., and Stefanini, C. (2015). "Underwater Navigation based on passive electric sense: New perspectives for underwater docking". In: *The International Journal of Robotics Research* 34.9, pp. 1228–1250 (cit. on pp. 10, 62).

Boyer, F., Lebastard, V., Chevallereau, C., and Servagent, N. (2013). "Underwater Reflex Navigation in Confined Environment Based on Electric Sense". In: *IEEE Transactions on Robotics* 29.4, pp. 945–956 (cit. on pp. 10, 72).

Braithwaite, V. A. (1998). "Spatial memory, landmark use and orientation in fish". In: *Spatial Representation in Animals*. Ed. by S. Healy. New York: Oxford University Press, pp. 86–102 (cit. on p. 9).

Budelli, R. and Caputi, A. A. (2000). "The electric image in weakly electric fish: Perception of objects of complex impedance". In: *Journal of Experimental Biology* 203, pp. 481–492 (cit. on p. 4).

Budelli, R., Caputi, A. A., Gomez, L., Rother, D., and Grant, K. (2002). "The electric image in Gnathonemus petersii". In: *Journal of Physiology Paris* 96, pp. 421–429 (cit. on p. 4).

Bullock, T. H. and Heiligenberg, W. (1986). *Electroreception*. New York: Wiley, J. (cit. on p. 3).

Cain, P. and Malwal, S. (2002). "Landmark use and development of navigation behaviour in the weakly electric fish Gnathonemus petersii (Mormyridae; Teleostei)". In: *Journal of Experimental Biology* 205, pp. 3915–3923 (cit. on p. 9).

Caputi, A. A. and Budelli, R. (2006). "Peripheral electrosensory imaging by weakly electric fish". In: *Journal of Comparative Physiology* 192.6, pp. 587–600 (cit. on p. 3).

Caputi, A. A., Castello, M. E., Aguilera, P., and Trujillo-Cenoz, O. (2002). "Electrolocation and electrocommunication in pulse gymnotids: signal carriers, pre-receptor mechanisms and the electrosensory mosaic". In: *Journal of Physiology Paris* 96, pp. 493–505 (cit. on pp. 3, 105).

Carlson, B. A., Hopkins, C. D., and Thomas, P. (2000). "Androgen correlates of socially induced changes in the electric organ discharge waveform of a mormyrid fish". In: *Hormones and Behavior* 38.3, pp. 177–186 (cit. on p. 3).

Clough, R. W. (1960). "The Finite Element Method in Plane Stress Analysis". In: *Proceedings of American Society of Civil Engineers* 23, pp. 345–378 (cit. on p. 25).

COMSOL (2015). *AC/DC Module User's Guide*. COMSOL Multiphysics® v. 5.2., Stockholm, Schweden (cit. on p. 25).

— (2016). *Introduction to COMSOL Multiphysics.* COMSOL Multiphysics® v. 5.2a., Stockholm, Schweden (cit. on p. 26).

Crawford, J. D. (1992). "Individual and sex specificity in the electric organ discharges of breeding mormyrid fish, Pollimyrus isidori". In: *Journal of Experimental Biology* 164, pp. 79–102 (cit. on p. 3).

Dimble, K.D., Faddy, J.M., and Humbert, J.S. (2014). "Electrolocationbased underwater obstacle avoidance using wide-field integration methods". In: *Bioinspiration & Biomimetics* 9.1, p. 016012 (cit. on p. 10).

Eickmann, F. (2014). "Klassifizierung einflussnehmender Parameter bei der Feldmessung mit bioinspirierten Elektrosensoren in Fluiden". BA thesis. Bielefeld University of Applied Sciences, Germany (cit. on p. 7).

— (2015). "Entwicklung eines Hardware/Software Co-Designs zur breitbandigen Analyse stationärer Parameter verrauschter, sinusartiger Signale mit Hilfe statistischer und trigonometrischer Methoden". MA thesis. Bielefeld University of Applied Sciences, Germany (cit. on p. 114).

Engelmann, J., Bacelo, J., Metzen, M., Pusch, R., Bouton, B., Migliaro, A., Caputi, A., Budelli, R., Grant, K., and von der Emde, G. (2008). "Electric imaging through active electrolocation: implication for the analysis of complex scenes". In: *Biological Cybernetics* 98.6, pp. 519–539 (cit. on p. 4).

Engelmann, J., Nobel, S., Rover, T., and von der Emde, G. (2009). "The Schnauzenorganresponse of Gnathonemus petersii". In: *Frontiers in Zoology* 6, p. 21 (cit. on pp. 6, 39, 40, 58).

Engelmann, J. and von der Emde, G. (2011). "Active Electrolocation". In: *Encyclopedia of Fish Physiology: From Genome to Environment.* Ed. by A. P. Farrell. Vol. 1. Academic Press, pp. 375–386 (cit. on pp. 4–6, 105).

Fairweather, G. (1978). *Finite Element Galerkin Methods for Differential Equations.* New York: Marcel Dekker (cit. on p. 27).

Fang, S., Peshkin, M., and MacIver, M. A. (2016). "Human-in-the-loop active electrosense". In: *Bioinspiration & Biomimetics* 12.1, p. 014001 (cit. on pp. 62, 66).

Gottwald, M., Bott, R. A., and von der Emde, G. (2017). "Estimation of distance and electric impedance of capacitive objects in the weakly electric fish Gnathonemus petersii". In: *Journal of Experimental Biology* 220, pp. 3142–3153 (cit. on p. 9).

Griffith, D. J. (1999). *Introduction to Electrodynamics*. 3rd ed. Prentice Hall (cit. on p. 13).

Heiligenberg, W. (1975). "Theoretical and experimental approaches to spatial aspects of electrolocation". In: *Journal of comparative physiology* 103.3, pp. 247–272 (cit. on p. 24).

Hestenes, M. R. and Stiefel, E. (1952). "Methods of Conjugate Gradients for Solving Linear System". In: *Journal of Research of the National Bureau of Standards* 49.6, pp. 409–436 (cit. on p. 35).

Hill, P. D. (1985). "Kernel estimation of a distribution function". In: *Communications in Statistics - Theory and Methods* 14.3, pp. 605–620 (cit. on p. 101).

Hofmann, V., Geurten, B. R., Sanguinetti-Scheck, J. I., Gomez-Sena, L., and Engelmann, J. (2014). "Motor patterns during active electrosensory acquisition". In: *Frontiers in Behavioral Neuroscience* 8, p. 186 (cit. on pp. 6, 40, 41, 67, 69).

Holland, J. H. (1992). *Adaptation in Natural and Artificial Systems: An Introductory Analysis with Applications to Biology, Control and Artificial Intelligence*. MA, USA: MIT Press Cambridge (cit. on p. 111).

Hollmann, M., Engelmann, J., and von der Emde, G. (2008). "Distribution, density and morphology of electroreceptor organs in mormyrid weakly electric fish: anatomical investigations of a receptor mosaic". In: *Journal of Zoology* 276.2, pp. 149–158 (cit. on p. 3).

Hopkins, C. D. (1983). "Sensory mechanisms in animal communication". In: *Animal Behaviour 2: Animal Communication*. Ed. by T. R. Halliday and P. J. B. Slater. Vol. 2. Oxford: Blackwell Scientific Publications, pp. 114–155 (cit. on p. 3).

— (1999). "Design features for electric communication". In: *Journal of Experimental Biology* 202.10, pp. 1217–1228 (cit. on p. 2).

Hopkins, C. D. and Bass, A. H. (1981). "Temporal coding of species recognition signals in an electric fish". In: *Science* 212, pp. 85–87 (cit. on p. 3).

Hoshimiya, N., Shogen, K., Matsuo, T., and Chichibu, S. (1980). "The Apteronotus EOD field: Waveform and EOD field simulation". In: *Journal of comparative physiology* 135.4, pp. 283–290 (cit. on p. 24).

Jackson, J. D. (1999). *Classical Electrodynamics*. 3rd ed. New York: Wiley, J. and Sons (cit. on pp. 13, 18, 20).

Bibliography

Jones, G. (2005). "Echolocation". In: *Current Biology* 15.13, pp. 484–488 (cit. on p. 1).

Kawasaki, M. (2009). "Evolution of Time-Coding Systems in Weakly Electric Fishes". In: *Zoological Science* 26.9, pp. 587–599 (cit. on p. 9).

Kramer, B. (1990). *Electrocommunication in teleost fishes: behavior and experiments.* Berlin Heidelberg New York: Springer (cit. on p. 3).

Landau, L. D., Lifshitz, E. M., and Pitaevskii, L. P. (1984). *Electrodynamics of Continuous Media.* 2rd ed. Vol. 8. Butterworth-Heinemann (cit. on pp. 13, 66).

Lanneau, S., Boyer, F., Lebastard, V., and Bazeille, S. (2017). "Model based estimation of ellipsoidal object using artificial electric sense". In: *International Journal of Robotics Research* 36.9, pp. 1022–1041 (cit. on p. 72).

Lebastard, V., Boyer, F., and Lanneau, S. (2016). "Reactive underwater object inspection based on artificial electric sense". In: *Bioinspiration & Biomimetics* 11.4, p. 045003 (cit. on pp. 6, 69).

Lebastard, V., Chevallereau, C., Girin, A., Servagent, N., Gossiaux, P. B., and Boyer, F. (2013). "Environment reconstruction and navigation with electric sense based on a Kalman filter". In: *International Journal of Robotics Research* 32.2, pp. 172–188 (cit. on pp. 10, 57, 62, 66, 89, 105).

Lissmann, H. W. (1951). "Continuous electrical signals from the tail of a fish, Gymnarchus niloticus Cuv." In: *Nature* 167, pp. 201–202 (cit. on p. 2).

— (1958). "On the Function and Evolution of Electric Organs in Fish". In: *Journal of Experimental Biology* 35, pp. 156–191 (cit. on p. 2).

Lissmann, H. W. and Machin, K. E. (1958). "The Mechanism of Object Location in Gymnarchus Niloticus and Similar Fish". In: *Journal of Experimental Biology* 35, pp. 451–486 (cit. on pp. 2, 10).

Lorensen, W. E. and Cline, H. E. (1987). "Marching Cubes: A High Resolution 3D Surface Construction Algorithm". In: *SIGGRAPH Computer Graphics* 21.4, pp. 163–169 (cit. on p. 71).

Machin, K. E. and Lissmann, H. W. (1960). "The mode of operation of the electric receptors in Gymnarchus niloticus". In: *Journal of Experimental Biology* 37.4, pp. 801–811 (cit. on p. 3).

Maxwell, J. C. (1865). "A Dynamical Theory of the Electromagnetic Field". In: *Philosophical Transactions of the Royal Society of London* 155, pp. 459–512 (cit. on p. 14).

— (1873). *A Treatise on Electricity and Magnetism.* 3rd ed. New York: Dover Publications (cit. on p. 14).

Mc Gregor, P. K. and Westby, G. W. M. (1992). "Discrimination of individually characteristic electric organ discharges by a weakly electric fish". In: *Animal Behaviour* 43, pp. 977–986 (cit. on p. 3).

Metzen, M., Biswas, S., Bousack, H., Gottwald, M., Mayekar, K., and von der Emde, G. (2012). "A biomimetic active electrolocation sensor for detection of atherosclerotic lesions in blood vessels". In: *IEEE Sensors Journal* 12.2, pp. 325–331 (cit. on p. 114).

Meyer, J. H. (1982). "Behavioral responses of weakly electric fish to complex impedances". In: *Journal of Comparative Physiology* 145, pp. 459–470 (cit. on p. 7).

Mogdans, J. and Bleckmann, H. (2012). "Coping with flow: behavior, neurophysiology and modeling of the fish lateral line system". In: *Biological Cybernetics* 106.11-12, pp. 627–642 (cit. on p. 2).

Moller, P. (1970). "Communication in weakly electric fish, Gnathonemus niger (Mormyridae) I. Variation of electric organ discharge (EOD) frequency elicited by controlled electric stimuli". In: *Animal Behaviour* 18.4, pp. 768–786 (cit. on p. 2).

Nelson, M. E. and MacIver, M. A. (1999). "Prey capture in the weakly electric fish Apteronotus albifrons: Sensory acquisition strategies and electrosensory consequences". In: *Journal of Experimental Biology* 202.10, pp. 1195–1203 (cit. on pp. 4, 57).

— (2006). "Sensory acquisition in active sensing systems". In: *Journal of Comparative Physiology A* 192, pp. 573–586 (cit. on p. 90).

Neveln, I. D., Bai, Y., Snyder, J. B., Solberg, J. R., Curet, O. M., Lynch, K. M., and MacIver, M. A. (2013). "Biomimetic and bio-inspired robotics in electric fish research". In: *Journal of Experimental Biology* 216, pp. 2501–2514 (cit. on pp. 10, 62, 66, 113).

Parzen, E. (1962). "On Estimation of a Probability Density Function and Mode". In: *The Annals of Mathematical Statistics* 33.3, pp. 1065–1076 (cit. on p. 95).

Pedraja, F., Hofmann, V., Lucas, K. M., Young, C., Engelmann, J., and Lewis, J. E. (2018). "Motion parallax in electric sensing". In: *Proceedings of the National Academy of Sciences* 115.3, pp. 573–577 (cit. on p. 6).

Peng, J., Zhu, Y., and Yong, T. (2017). "Research on Location Characteristics and Algorithms based on Frequency Domain for a 2D Underwater Active Electrolocation Positioning System". In: *Journal of Bionic Engineering* 14.4, pp. 759–769 (cit. on p. 62).

Rasnow, B. (1996). "The effects of simple objects on the electric field of Apteronotus". In: *Journal of Comparative Physiology A* 178.3, pp. 397–411 (cit. on pp. 10, 22, 42, 66, 106).

— (2005). "Measuring and visualizing EOD fields". In: *Communication In Fishes*, pp. 600–622 (cit. on p. 85).

Rasnow, B., Assad, C., Nelson, M. E., and Bower, J. M. (1989). "Advances in Neural Information Processing Systems 1". In: ed. by D. S. Touretzky. San Francisco, CA, USA: Morgan Kaufmann Publishers Inc. Chap. Simulation and Measurement of the Electric Fields Generated by Weakly Electric Fish, pp. 436–443 (cit. on p. 24).

Rayleigh, J. W. S. (1877). *The Theory of Sound*. London: Macmillan (cit. on p. 27).

Ritz, W. (1908). *Über eine neue Methode zur Lösung gewisser Variationsprobleme der mathematischen Physik*. Journal für die reine und angewandte Mathematik (cit. on p. 27).

Rosenblatt, M. (1956). "Remarks on Some Nonparametric Estimates of a Density Function". In: *The Annals of Mathematical Statistics* 27.3, pp. 832–837 (cit. on p. 95).

Sawtell, N. B. (2010). "Multimodal integration in granule cells as a basis for associative plasticity and sensory prediction in a cerebellum-like circuit". In: *Neuron* 66.4, pp. 573–584 (cit. on p. 6).

Schroeder, W. J., Martin, K., and Lorensen, B. (2006). *The Visualization Toolkit An Object-Oriented Approach to 3D Graphics*. 4rd ed. Visualization Handbook. Burlington: Butterworth-Heinemann, pp. 593–614 (cit. on pp. 68, 71, 75).

Schwab, A. J. (2013). *Begriffswelt der Feldtheorie*. 7rd ed. Springer Berlin Heidelberg (cit. on p. 27).

Schwarz, H. R. (1991). *Methode der finiten Elemente*. 3rd ed. B.G.Teubner, Stuttgart (cit. on p. 28).

Servagent, N., Jawad, B., Bouvier, S., Boyer, F., Girin, A., Gomez, F., Lebastard, V., Stefanini, C., and Gossiaux, P. (2013). "Electrolocation Sensors in Conducting Water Bio-Inspired by Electric Fish". In: *IEEE Sensors Journal* 13.5, pp. 1865–1882 (cit. on p. 10).

Sheskin, D. (2006). *Handbook of parametric and nonparametric statistical procedures*. 4rd ed. Chapman and Hall/CRC (cit. on p. 100).

Sichert, A. B., Bamler, R., and van Hemmen, J. L. (2009). "Hydrodynamic Object Recognition: When Multipoles Count". In: *Physical Review Letters* 102.5 (cit. on p. 2).

Silverman, B. W. (1986). *Density Estimation for Statistics and Data Analysis*. London: Chapman & Hall (cit. on p. 101).

Silverman, Y., Miller, L. M., MacIver, M. A., and Murphy, T. D. (2013). "Optimal Planning for Information Acquisition". In: *In Proceedings of the IEEE/RSJ International Conference on Intelligent Robots and Systems (IROS), Tokyo, Japan*, pp. 5974–5980 (cit. on pp. 57, 89, 105).

Silverman, Y., Snyder, J., Bai, Y., and MacIver, M. A. (2012). "Location and Orientation Estimation with an Electrosense Robot". In: *In Proceedings of the IEEE/RSJ International Conference on Intelligent Robots and Systems (IROS),Vilamoura, Portugal*, pp. 4218–4223 (cit. on pp. 10, 57, 89, 105).

Silvester, P. P. and Ferrari, R. L. (1996). *Finite elements for electrical engineers*. 3rd ed. Cambridge University Press (cit. on p. 27).

Sim, M. and Kim, D. (2011). "Electrolocation based on tail-bending movements in weakly electric fish". In: *Journal of Experimental Biology* 214, pp. 2443–2450 (cit. on p. 114).

Snyder, J., Silverman, Y., Bai, Y., and MacIver, M. A. (2012). "Underwater object tracking using electrical impedance tomography". In: *2012 IEEE/RSJ International Conference on Intelligent Robots and Systems, IROS 2012*, pp. 520–525 (cit. on pp. 10, 114).

Solberg, J. R., Lynch, K. M., and MacIver, M. A. (2008). "Active electrolocation for underwater target localization". In: *International Journal of Robotics Research* 27.5, pp. 529–548 (cit. on pp. vii, 8–10, 36, 39, 41, 42, 57, 61, 63, 66, 89, 105–107).

Bibliography

Stachniss, C. and Burgard, W. (2014). "Particle Filters for Robot Navigation". In: *Foundations and Trends in Robotics 2012 (published in 2014)* 3.4, pp. 211–282 (cit. on pp. 10, 41).

Stamper, S. A., Roth, E., Cowan, N. J., and Fortune, E. S. (2012). "Active sensing via movement shapes spatiotemporal patterns of sensory feedback". In: *Journal of Experimental Biology* 215.9, pp. 1567–1574 (cit. on p. 6).

Staudacher, E., Gebhardt, M. J., and Dürr, V. (2005). "Antennal Movements and Mechanoreception: Neurobiology of Active Tactile Sensors". In: *Advances in Insect Physiology* 32, pp. 49–205 (cit. on p. 2).

Szabo, T. (1965). "Sense organs of the lateral line system in some electric fish of the Gymnotidae, Gymnarchidae, and Mormyridae". In: *Journal of Morphology* 117, pp. 229–250 (cit. on p. 3).

Toerring, M. J. and Belbenoit, P. (1979). "Motor programmes and electroreception in mormyrid fish". In: *Behavioral Ecology and Sociobiology* 4.4, pp. 369–379 (cit. on p. 6).

Toerring, M. J. and Moller, P. (1984). "Locomotor and electric displays associated with electrolocation during exploratory behavior in mormyrid fish". In: *Behavioural Brain Research* 12.3, pp. 291–306 (cit. on pp. 4, 6, 40).

Turing, A. M. (1948). "Rounding-off errors in matrix processes". In: *The Quarterly Journal of Mechanics and Applied Mathematics* 1.3, pp. 287–308 (cit. on p. 35).

von der Emde, G. (1999). "Active electrolocation of objects in weakly electric fish". In: *Journal of Experimental Biology* 202.10, pp. 1205–1215 (cit. on pp. 2, 3, 7).

von der Emde, G. and Bleckmann, H. (1997). "Waveform tuning of electroreceptor cells in the weakly electric fish, Gnathonemus petersii". In: *Journal of Comparative Physiology A: Neuroethology, Sensory, Neural, and Behavioral Physiology* 181, pp. 511–524 (cit. on p. 3).

von der Emde, G. and Fetz, S. (2007). "Distance, shape and more: recognition of object features during active electrolocation in a weakly electric fish". In: *Journal of Experimental Biology* 210.17, pp. 3082–3095 (cit. on pp. 2, 6).

von der Emde, G. and Schwarz, S. (2002). "Imaging of Objects through active electrolocation in Gnathonemus petersii". In: *Journal of Physiology-Paris* 96.5-6, pp. 431–444 (cit. on p. 105).

131

Wolf-Homeyer, S., Engelmann, J., and Schneider, A. (2016). "Electrolocation of objects in fluids by means of active sensor movements based on discrete EEVs". In: *Bioinspiration & Biomimetics* 11.5, p. 055002 (cit. on pp. 39, 61–63, 67, 69, 72, 75, 89, 93, 94).

— (2018). "Application of reduced sensor movement sequences as a precursor for search area partitioning and a selection of discrete EEV contour-ring fragments for active electrolocation". In: *Bioinspiration & Biomimetics* 13.6, p. 066008 (cit. on pp. 61, 93, 94).

Zakon, H. H. (1987). "The electroreceptors: diversity in structure and function". In: *Sensory biology of aquatic animals*. Ed. by A. Atema, R. R. Fay, A. N. Popper, and W. N. Tavolga. Berlin Heidelberg New York: Springer, pp. 813–850 (cit. on p. 3).

Zill, S., Schmitz, J., and Büschges, A. (2014). "Load Sensing and Control of Posture and Locomotion". In: *Arthropod Structure and Development* 33, pp. 273–286 (cit. on p. 1).